FLUID DYNAMIC ACTUATORS FOR SATELLITE ATTITUDE CONTROL AND THERMAL MANAGEMENT

by

Sobhan Etemadi
B.Eng., Aerospace Engineering, Ryerson University, 2011

A dissertation

presented to Ryerson University

in partial fulfillment of the

requirements for the degree of

Doctor of Philosophy

in the Program of

Aerospace Engineering

Toronto, Ontario, Canada, 2017

AUTHOR'S DECLARATION FOR ELECTRONIC SUBMISSION OF A DISSERTATION

I hereby declare that I am the sole author of this dissertation. This is a true copy of the dissertation, including any required final revisions, as accepted by my examiners.

I authorize Ryerson University to lend this dissertation to other institutions or individuals for the purpose of scholarly research.

I further authorize Ryerson University to reproduce this dissertation by photocopying or by other means, in total or in part, at the request of other institutions or individuals for the purpose of scholarly research.

I understand that my dissertation may be made electronically available to the public.

_____

Sobhan Etemadi

FLUID DYNAMIC ACTUATORS FOR SATELLITE ATTITUDE CONTROL AND THERMAL MANAGEMENT

Sobhan Etemadi

Doctor of Philosophy, Aerospace Engineering, Ryerson University, Toronto (2017)

ABSTRACT

In this thesis, the application of fluid based actuators for satellite attitude control and thermal management is investigated. The actuator named *Pumped Fluid Loop Actuator* (PFLA) is examined to satisfy the need for integrated attitude and thermal management systems while considering strict mass and power budgets. A nonlinear voltage-driven control law is formulated and the feasibility of the PFLA for satellite attitude maneuvers is addressed. A high-fidelity PFLA model is developed. The power consumption of the PFLA is examined in the presence of sensor noise. Simulation results demonstrate its feasibility for attitude tracking capabilities of up to ± 0.01° with slew rates of up to 10 °/s.

Next, the limitations of existing fluid dynamic actuators are overcome through the design of a novel Patent Pending *Pumped Fluid Spherical Actuator* (PFSA). The PFSA extends the capabilities of fluid dynamic actuators and allows for satellite attitude control about any arbitrary axis through spherical design, and introduces a fault-tolerant functionality that allows it to be used as a sensor in the event of rate-gyro failure of the attitude determination subsystem. The dynamic model of the PFSA is obtained through computational fluid-dynamics and finite-element analysis using the grid-independent solution. The passive stabilization capabilities of the

PFSA are investigated. Simulation results show an order of three-fold reduction in settling time in comparison to existing fluid dynamic actuators.

Lastly, a design modification is proposed for PFLA in order to examine its thermal management capabilities. A comprehensive investigation is carried out to perform thermal transport from onboard electronics through conduction and convection. Simulation results demonstrate the advantages of thermal transport while considering fluid rotation inside the PFLA as opposed to stationary fluid.

ACKNOWLEDGEMENTS

I can probably write another thesis to express my gratitude and appreciation for everyone who has been there for me throughout this grueling roller coaster ride. I hope that I am able to convey a small segment of my appreciation in this section.

Anyone in the research field knows the importance of a good supervisor. I am happy to say that I have had the privilege for a great one. Dr. Kumar, I remember when I first came to your office in 2009 asking for a research position and you asked me for a higher GPA. I returned at the end of the year with just that and you accepted me as your research student. Seven years have gone by since then, and I can still remember my excitement when you accepted me. Thank you endlessly for your incredible support and opportunities you provided me with through the years. Time and time again you have helped guide me through the difficulties of research and motivated me to keep pushing forward. Thank you for allowing me to express my own passion in my research. I cannot imagine having taken this path with any other supervisor.

After you find yourself a great supervisor, sometimes, you end up in a lab with great people. But other times, you may get lucky, and end up finding lab mates that teach you the real value of friendship; friendships that you know will last a lifetime. Chow, Khaaj, words cannot even begin to describe how much I love you guys. From the gym days, to the days of you guys yelling and screaming at me to finish my thesis, to the long endless nights trying to solve simulations, to moving across the globe and starting a new chapter, I cherish the memories we have made together and the friendship that exists between us. Thank you both for being there for me through thick and thin and continuing to be there. I could not have done this without you guys. Also, a big THANK YOU to Mikey, Afshin, Venki, Min, Alex, and Waqas for making the lab experience so much fun.

And then, there is family. Where do I start, what do I even say? 27 years, and you have always been there for me. We have gone through ups and downs, and we have always pulled through. If there is anything I have learned is that no matter how tough life gets, keep your values, your love for one another, and your willingness to move forward. When you work hard enough, everything always works out. Babash, Shasha, thank you for working so hard, giving up so much, and making it so easy for me to go through school to get a good education and never having to worry about anything other than that. I am lucky to have parents like you. Brother,

Scarrrrr! Thank you for being a cool bro. Your music is incredible. Your songs have been on repeat for the past few months while writing this thesis. Your music is inspirational and I know you are going to go far with it. Hans Zimmer…pft. ~~F~~Pharid - LIP. I love you all and I hope I have made you proud.

Last but not least, you need someone that keeps you excited and not bored out of your mind when you are in the research field. Vania, the past few years with you have been an incredible adventure. One that I am thrilled you stuck around for. Thank you for being there for me through the fun times and most importantly through the tougher ones. You always know how to make me feel better, especially with your Nutella ice cream. I am thrilled this chapter of our lives is behind us and I am excited for what adventures lay ahead. Lava you.

For

My Beloved Mother and Father,

Shahla & Behzad

TABLE OF CONTENTS

LIST OF TABLES

LIST OF FIGURES

NOMENCLATURE

Alphabetical

$A_{act} \in \mathbb{R}^{3\times4}$	Projection Matrix
D	Hydraulic Diameter, $2wh/(w+h)$
e_b	Electromotive Force
$\bar{e}$	Principal Axis (Euler's Theorem)
f	Darcy Friction Factor
f_d	Friction Drag Coefficient, 1.21×10^{-6} Nm/Rpm
g_x, g_y, g_z	Components Of Gravitational Acceleration
H	Angular Momentum Vector
h	Loop Cross-Sectional Height
$I \in \mathbb{R}^{3\times3}$	Identity Matrix
i_a	Armature Current
J_m	Impeller Moment Of Inertia
$J_s \in \mathbb{R}^{3\times3}$	Total Satellite Moment Of Inertia
$J_{fl} \in \mathbb{R}^{4\times4}$	Fluid Axial Moments Of Inertia
K_t	Motor Torque Constant, $7.38 \times 10^{-3} \frac{V \cdot sec}{rad}$
K_m	Back-EMF
k	Thermal Conductivity
L_a	Armature Inductance
l	Channel Length
N_c	Coulomb Friction, 7.06×10^{-4} Nm
n	Control Gains
P_w	Power
p	Pressure
Q_{imp}	Pump Volumetric Flow Rate
q_v	Vector Portion Of Quaternion (q_1, q_2, q_3)
q_4	Scalar Portion Of Quaternion
R	PFLA Loop Radii
R_a	Armature Resistance
Re	Reynolds Number, $\frac{\rho V D}{\mu}$
$R_O^B \in \mathbb{R}^{3\times3}$	Direction Cosine Matrix Transformation
R_{orbit}	Orbital Altitude From The Center Of The Earth
r_{fl}	Cross-Sectional Radius Of Fluid Loop
S	Terminal Sliding Mode Surface
t	Time

V_{fl}	Linear Fluid Velocity
v_a	Applied Armature Voltage
w	Loop Cross-Sectional Width
X_I, Y_I, Z_I	Inertial Reference Frame
x_0, y_0, z_0	Orbital Reference Frame
x, y, z	Body-Fixed Coordinate Frame

Greek

τ_m	Motor Torque
σ_{ij}	Viscous Stress Tensor
ρ	Fluid Density
μ	Fluid Kinematic Viscosity
β	Relative Flow Angle
ω_{fl}	Fluid Angular Velocity
τ_{ff}	Fluid Friction Torque
ε_{fl}	Shear Stress
η	State Of Loops (For Filled Loops, 2π)
τ_{mf}	Torque Motor Friction
τ_f	Total Friction Torque
$\alpha°, \beta°$	Configuration Skew Angles
φ, α, γ	Roll, Pitch, Yaw
τ_e	External Disturbance
φ_q	Principal Angle (Euler's Theorem)
ω_{BI}^B	Angular Velocity Of The Satellite Relative To The Inertial Frame, Expressed In The Body Frame
ω_{BO}^B	Angular Velocity Of The Satellite Relative To The Orbital Frame, Expressed In The Body Frame
ω_{OI}^B	Orbital Angular Velocity Of The Satellite Expressed In The Body Frame, $R_O^B[0 \quad -\omega_0 \quad 0]^T$
ω_0	The Orbital Angular Velocity, $\sqrt{\mu_e/R_{orbit}^3}$
μ_e	Gravitational Parameter Of Earth (3.986×10^{14} m$^3/s^2$)
ω_{imp}	Pump Impeller Velocity
$\varkappa_1, \varkappa_2, \delta_1, \delta_2, \delta_3, \epsilon, \varepsilon, \lambda_1, \lambda_2$	Control Gains
τ_c	Control Command Input
τ_a, τ_{fl}	Applied Actuator Torque
ω	Angular Velocity

Subscripts

act	Actuator
c	Control
d	Desired State
e	Error
fl	Fluid
i	1,2,3
imp	Impeller
s	Satellite
sat	Saturation
0	Initial Condition

Accents

$(\dot{x})$	$\frac{d(x)}{dt}$
$(\ddot{x})$	$\frac{d^2(x)}{dt^2}$
$[x]^{\times}$	Skew-Symmetric Matrix
$[x]^T$	Transpose Operation Of Matrix x
$\|\|x\|\|$	Norm Of x
$\|x\|$	Absolute Value Of x
$\hat{x}$	Estimate

Acronyms

AC	Alternating Current
ACS	Attitude Control System
AOR	Axis Of Rotation
ATM	Attitude Tracking Maneuver
CAD	Computer-Aided Design
CFD	Computational Fluid Dynamics
CMG	Control Moment Gyro
DC	Direct Current
DGCMG	Double Gimbal Control Moment Gyro
DOF	Degrees Of Freedom
ECI	Earth Centered Inertial
FEA	Finite Element Analysis
HITL	Hardware-In-The-Loop

IATMS	Integrated Attitude And Thermal Management System
LEO	Low Earth Orbit
LHP	Loop Heat Pipe
LVLH	Local-Vertical Local-Horizontal
MEMS	Microelectromechanical Systems
MHD	Magnetohydrodynamics
NSE	Navier-Stokes Equations
P2P	Point-To-Point
P4	Pyramid Actuator Configuration
PCB	Printed Circuit Board
PD	Proportional-Derivative
PFLA	Pumped Fluid Loop Actuator
PFSA	Pumped Fluid Spherical Actuator
PID	Proportional-Integral-Derivative
PWM	Pulse Width Modulation
REC	Rotational Electromechanical Converter
RW	Reaction Wheel
S3	Orthogonal 3 Actuator Configuration
S4	Orthogonal 3 + 1 Skew Actuator Configuration
SGCMG	Single Gimbal Control Moment Gyro
VDNCL	Voltage-Driven Nonlinear Control Law
VSCMG	Variable Speed Control Moment Gyro

CHAPTER 1
INTRODUCTION

ADVANCED space missions require effective control actuators to ensure accurate and rapid response to attitude maneuver commands while maintaining the system reliability in the presence of model uncertainties, subsystem failures, and external disturbances [1]. Ignoring the actuator dynamics can in practice result in performance degradation or loss of system stability [2]. Accurate attitude tracking requires both actuators that provide accurate torque outputs as well as robust control algorithm to uphold the agile system requirements. In this study, we aim to assess the feasibility of fluid dynamic actuators known for satellite attitude maneuvers. The study is initiated with a literature review of existing actuators used in practical satellite applications.

1.1 Literature Review

Two categories of actuators exist for satellite attitude control, passive and active. The former requires no power input to the system to operate and is used for stabilization while the latter requires a power source to produce control torques. For this research, both operational categories of actuators are considered as they provide a method to actively alter the attitude of a satellite as required for a particular mission and to passively stabilize its attitude in an environment where energy consumption is a critical factor.

1.1.1 Reaction Wheels

Figure 1.1: Blue Canyon Technologies Reaction Wheel Assembly [3]

Reaction wheels (RW) are angular momentum exchange devices that are used in satellite to alter or maintain their attitude as required for a given mission. Reaction wheels can impose a zero-bias and bias angular velocity and are accelerated and decelerated to produce control torques to adjust or maintain the attitude of a satellite. The control torque generated by a RW is proportionally controlled by the power that is delivered to the motor shaft to which its wheel is permanently connected. Inherently, greater power delivered to the motor will result in the amplification of the torque and thus a greater angular momentum exchange with the satellite and vice versa. However, the maximum and minimum torque that can be generated by the wheel is directly limited by the capabilities of the motor.

In a survey conducted by Votel [4] it was demonstrated that conventional RWs have momentum capabilities up to 100 Nm·s; beyond that, they jeopardize the structural integrity of the unit and can lead to a mission's failure. As such, they require considerable support structures that in turn add undesired mass to the system.

1.1.2 Control Moment Gyroscope

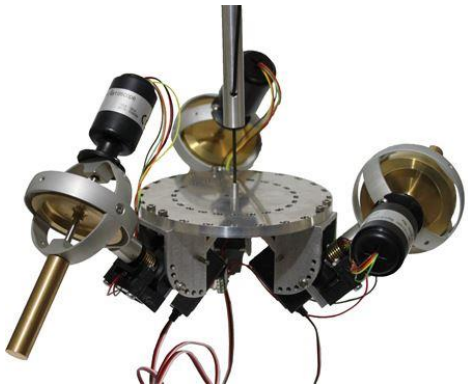

Figure 1.2: Bright Fusion Limited Control Moment Gyro Assembly [5]

The control moment gyro (CMG) is a special actuator configuration wherein an actuator is mounted on a gimbal that acts to direct the control torque vector of the CMG to provide maximum control torque about the desired axis. CMGs output large and precise torques for agile attitude maneuvers and thus have proven advantageous over traditional standard configurations [6]. However, the existence of a singularity with the CMG presents a limitation in producing control torque about all arbitrary axes. In the case where a singularity does occur, all torque directions lie on a two-dimensional plane in a three-dimension angular momentum space [7]. CMGs act as torque amplifiers, a property making them ideal as attitude actuators for large satellite and are categorized under three subcategories: 1) Single Gimbal CMG (SGCMG), 2) Double Gimbal CMG (DGCMG), and 3) Variable Speed Control Moment Gyros (VSCMG).

The category of SGCMG has only a single degree of freedom (DOF) due to only a single angle being controlled by the gimbal. In DGCMG, the existence of two gimbals allows for multiple DOF with an almost spherical angular momentum envelope and thus can perform rapid attitude maneuvers with high efficiency [6]. However, both SGCMG and DGCMG generally operate at a constant angular velocity, and therefore the configuration only controls the torque vector and not the magnitude. To overcome this drawback, the VSCMG, as its name suggests allows for the variability in actuator angular velocity and an additional DOF that can be used to avoid the singularity problem [7]. However, the complexity of CMG design has limited their practical use in satellite missions.

1.1.3 Electromagnetic Actuators

Figure 1.3: Vectronic Aerospace Magnetorquer VMT-35 Assembly [8]

The simplest of electromagnetic actuators are magnetorquers. These are simple devices that operate through the winding of copper wire around a carbon rod to form an electromagnetic coil. An electrical current passing through the coil generates a magnetic field that interacts with the Earth's magnetic field to stabilize a satellite. The necessity of a strong external magnetic field renders them unsuitable for deep space missions and limits their applications. Generally, magnetorquers are used for stabilization and momentum dumping from RWs in low earth orbits (LEO).

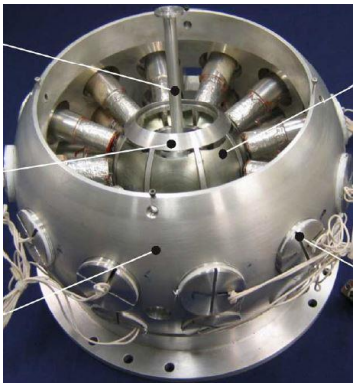

Figure 1.4: Spherical Electromechanical Actuator Assembly [9]

To extend the limits of control about any arbitrary axis and eliminate singularities, the advancements in gimbal technologies have led to investigations and developments in spherical actuators that use electromagnetic principles. In an attempt to expand on the works of multi-DOF actuators as first assessed by Williams et al. [10], extensive research has been carried out on spherical actuators based on variable-inductance [11, 12]. However, the complexity of the motor

structure makes them unsuitable for practical applications. Further advancements were suggested [13, 14] through the use of permanent magnets but the technology was not mechanically robust and provided low specific torque capabilities.

To address the drawbacks of the preliminary systems, Wang et al. [15] developed a spherical permanent magnet actuator capable of 3-DOF and high specific torque. A complete set of equations governing the kinematic and dynamics of the model were developed along with an approach to achieve maximum torque. The feasibility and efficiency of the actuator was demonstrated through hardware-in-the-loop (HITL) simulations.

Similarly, Yan et al. [9] fabricated and tested a 3-DOF spherical actuator with a full circle of permanent magnets and two layers of air-core coils. Their analysis suggested the advantage of singularity-free actuation due to the spherical configuration that was verified through the developed torque modeling.

More recent studies in the field of actuator technologies as presented by Chen et al. [16] consider a spherical permanent magnet actuator with a stator consisting of 24 coils [9] and 8 permanent magnet poles. Their analyses through experiment and simulations concluded the effectiveness of spherical design with increased stability and reliability through optimization methods based on current redundancy.

In a similar effort, a new type of spherical voice coil actuator was developed by Kim et al. [17] with one pair of coils having a circular profile, while the other pair exhibits a rectangular contour. The method of operation for this actuator is based on the Lorentz force, whereby the torque produced from each coil is directly proportional in driving current; this notion allows for simplicity in controlling the actuator.

Further integration of electromagnetics can be seen from the principles of magnetofluid dynamic (MHD) pumping that offers a unique method of transporting fluid inside channels while eliminating the need for mechanically moving parts [18]. A paper written by Bushnell [19] from NASA discusses revolutionary technologies for the next ten years that will extend the frontiers of space technology. Among the various technologies covered, propulsion through MHD methods

is of high consideration due to the high specific impulse thrust available from said technology without having to haul fuel around the solar system.

The underlying concept of MHD surpasses its functionality of measurement and control; wherein the absence of mechanical components enforces high-reliability, low manufacturing costs, and produces torques that are ripple-free [20]. MHD relies on the interaction between an electric field and an orthogonal magnetic field to create a Lorentz force responsible for the motion of a fluid infused with magnetic particles such as iron-Fe.

In a study carried out by Jang and Lee [21] where they developed the first ever micropump based on MHD principles, they observed the generation of bubbles due to the electrolysis of the conducting fluid that directly affected the performance characteristics of the pump. It was determined that under a specified voltage of 45V, larger and fewer bubbles were generated than at the higher voltages. This phenomenon was a direct result of the selection of the conductive fluid, seawater, which produces hydrogen gas as a result of the chemical reaction through electrolysis; similar results were obtained in the works of [22]. In an attempt to eradicate the effects of electrolysis Lemoff and Lee [23] suggested the use of AC current along with an alternating magnetic field, in contrast to [21] where DC was used. This presented a solution for the formation of bubbles however it resulted in a reduction in pump performance due to the limited current amplitude and weak alternating magnetic field.

To eradicate the effects of electrolysis, Karmozdi et al. [24] developed a novel micropump that offered an improvement of 153% over leading MHD micropumps at the time of their research. Their design used the generated Lorentz force to move the electroconductive liquid, mercury, through the fluid channels; eliminating the effects of electrolysis as the generated heat from the current did not evaporate the working fluid. Results obtained therein are in agreement with those of Moghadam and Shafii [25] whereby the elimination of electrolysis is evident through the use of mercury as the working fluid.

An assessment carried out by Rabinovich and Grishin [26] on the Auroral Probe of the INTERBALL Project demonstrated the effectiveness of MHD elements, in combination with accelerometers, in stabilizing the rotation of a satellite with flexible appendages without reducing

its angular velocity. However, the technology required to efficiently produce high torque using MHD methods for satellite attitude control does not currently exist. MHD requires high voltage and high current in order to produce an effective control force. In space applications, this would result in high power consumption for MHD actuators and would be unfeasible for practical space missions. Furthermore, in order to produce a high Lorentz force, the anode and cathode in the MHD pump need to be a highly conductive material such as copper, and due to the nature of MHD, the anode and cathode corrode rapidly with increasing current. This factor would limit the useable lifetime of the MHD and jeopardize the space mission. Nonetheless, it is evident that the use of fluid as a momentum transfer medium is capturing the attention of modern research.

1.1.4 Pumped Fluid Loop Actuators

Figure 1.5: Pumped Fluid Loop Actuator Assembly [27]

Research in the use of fluid dynamic principles for satellite attitude control has been further examined in the literature through the use of a DC pump as opposed to MHD forces for their practicality and requirement of lesser power input. The method of fluid transport through pipes onboard the satellites to control its attitude have been presented through the use of a pumped fluid loop actuator (PFLA).

In an attempt to reduce propellant mass, the use of fluid based dampers to stabilize a rotating module aboard a satellite was investigated by Gasbarri and Teofilatto [28]. They analyzed the dynamics and effectiveness of two fluid dampers fully filled with viscous fluid, one positioned on the pitch plane and the other on the roll plane. Through angular momentum exchange between the satellite and the fluid encased inside the pipes, they observed dissipation of angular

momentum from the rotating arms to the satellite. Their results validated the application of fluid dampers as a means for passively dissipating energy.

Further expanding into the notion of fluid based systems as attitude control devices, Kumar [29] proposed the application of three PFLA for addressing the three-dimensional attitude stabilization problem. His method comprised of three independent loops attached to a satellite in a standard 3 orthogonal configuration wherein each loop is positioned with its torque vector acting along each of pitch, roll, and yaw axes. Numerical simulation of the actuators validated the feasibility of such a system in both passive and active states for achieving attitude stabilization in the presence of environmental disturbances. It was further determined that by using nonlinear control algorithms, the effects of environmental disturbances can be stabilized using the PFLA while leaving the satellite attitude response unaffected. However, the active simulations did not account for actuator dynamics.

A study based on the foundations laid by Kumar [29] was carried out by Nobari and Misra [30], [31] whereby four PFLA were positioned based on the standard square pyramid configuration, to add redundancy to the control system, and an assessment was conducted to observe their performance for passive satellite attitude stabilization. Their analysis confirmed that by using the PFLA as passive dampers, all attitude disturbances were dissipated when the satellite was in circular orbit and only roll-yaw disturbances were alleviated for elliptical orbits. Due to the passive nature of the PFLA dampers, the stabilization process was slow and took over 30 Earth orbits as the damping torque was not large enough to provide stabilization in a short time. Furthermore, the passive use of the actuators did not allow for asymptotic stabilization of the satellite pitch angle for an elliptical orbit. In an attempt to reduce the stabilization settling time of the satellite, they introduced an active system using PID control. The results suggested a significant reduction in settling time to approximately 600s. However, once again the actuator dynamics were not examined for the active case.

In further expanding their works, Nobari and Misra [32] proposed a novel hybrid attitude control scheme for satellite attitude stabilization. They proposed the use of two magnetorquers in conjunction with one active PFLA to provide multi-axial active stabilization. An active attitude control system using the PFLA was examined and the settling time was reduced by a magnitude

of approximately 10 from their initial passive study. They also considered the case of actuator faults wherein a failure of the magnetorquer occurred. Their results indicated that the failure of the magnetorquer providing control torques along the pitch axis is the most critical as the dynamic coupling that exists between the pitch axis and the roll or yaw axis is quite weak. In contrast, a failure in the roll axis coil would not be detrimental as the yaw axis symmetry could account for stabilization in the roll axis. Nevertheless, they determined that their hybrid actuator arrangement was capable of using the PFLA for attitude stabilization even under actuator failure of the magnetorquer but at the cost of high pump pressure and high magnetic dipole moment; once again the dynamics of the PFLA were not considered in the research.

Similarly, Xiao-wei et al. [33] have examined the use of mechanically pumped fluid loops for attitude control. Through the use of a proportional-derivative (PD) control algorithm, they facilitated multi-axial stability through numerical simulation without actuator modeling. They examined both open and closed loop solutions to prove the effectiveness and feasibility of fluid loop applications to which they concluded offer performance improvements and volume/mass reductions making them ideal for micro and nanosatellite technologies.

The PFLA actuators considered in this study use a brushless DC micropump to transport fluid across a channel. The channels are typically circular tubes that are positioned to provide a torque along the required axis to be controlled. In line with reaction wheel technology, PFLAs use the angular momentum exchange between the fluid-filled tubes and the satellite body to produce control torques. The performance enhancements gained from using fluid to stabilize satellite can be recognized through the research and advancements in fluid-loop technologies [29, 32-34]. The method of PFLA actuation requires the use of a mechanical pump that is susceptible to degradation and produces high-frequency noise and jitters affecting peripheral electronics due to the motion of the motor; similar to the noise disturbance caused by RW motors [35]. In comparison to traditional RWs, PFLAs offer large damping torques, lightweight, and low cost and can be varied according to mission requirements; a large PFLA with low fluid angular velocity and low viscosity results in an energy efficient system with minimal vibration effects on the satellite structure [29].

1.2 Ryerson University Small Satellite Program

Small satellite designs have revolutionized space engineering techniques to complement the interest of research and development in both academia and industry. With high consideration on production costs with the advancement of micro-technology, small specialized satellites are becoming cheaper to produce however with limitations placed on their missions [36]. While anticipating further advances in miniaturization, *the Space Systems Dynamics, and Control* SSDC) laboratory at *Ryerson University*, under the supervision of Dr. K.D. Kumar, focusses primarily on the design and development of small satellite control systems. The overall objective is to advance research on small satellite design.

The *RyeSat* program includes the design and development of miniature satellites: (1) 500 gm tube satellite (*TubeSat*), (2) 1 kg pico-sized satellite (*PicoSat*), (3) 10 kg nano-sized satellite (*NanoSat*), and (4) 100 gm femto-sized satellite (*FemSat*). This research is aimed at the NanoSat-class. The result of this task introduces applications and missions for small satellite to expand into divisions of space exploration and other sectors not currently being addressed due to the limitations in small satellite performance capabilities. The research entailed herein aims to provide Nano satellite satellites with increased attitude control capabilities through the use of fluid dynamic principles. The applications of fluid dynamics bring several advantages not available with other actuator devices.

To this end, the problems that exist for modern actuators to control Nano satellite in deep space missions are addressed subsequently and are the objectives of this research.

1.3 Problem Statement

Modern space missions require precise satellite attitude control capabilities at low cost. The problem of fault-tolerant attitude control in alleviating disturbances such as actuator saturation or sensor noise to date has been exhaustively examined from the perspective of the control algorithm, and no attempt has been recognized to address this issue from the actuator perspective. The lack of innovation and advancement in satellite actuator technologies has not

addressed the capability of hardware for becoming fault-tolerant itself. Complex control algorithms are derived and are not always applicable to practical systems.

While actuator devices in use today can provide agile slew maneuver performances, they require complex precision machining and supplementary subsystems to ensure their reliability during the mission which in turn adds significant costs. Small satellites are the modern day research and observation tool and require attitude control systems with greater capabilities. Many significant challenges must be overcome before agile satellite maneuvering is available at low costs. The problem statements for this dissertation can be classified as:

[PROB1] ***Attitude control in the presence of actuator saturation:*** The application of theoretical control algorithms does not consider the limitations of hardware in the form of actuator saturation from the point of view of the hardware. This results in simulations that do not account for the real performance of the actuator systems. Furthermore, the necessity of power-optimal and precise ACSs requires precision-crafted reaction wheels or control moment gyro configurations that consume a large volume in the satellite and are not applicable for small satellite missions due to their high manufacturing costs. Small satellite missions settle for ACSs that provide larger attitude errors as a trade-off for cost, therefore limiting applications for small satellites.

[PROB2] ***Enhancing actuator performance for attitude control using novel design:*** Actuators have limitations due to their physical geometries and the boundaries of their supplementary hardware such as gimbals. A novel actuator design is required for attitude control about any arbitrary rotation axis.

[PROB3] ***Fault-tolerant actuator design:*** Fault-tolerant control is examined through the development of nonlinear control algorithms that do not consider the actual hardware capabilities; ACSs failures have been addressed from the viewpoint of the control law; however fault-tolerant functionality has not been examined from the actuator design perspective. Closed-loop control algorithms require feedback in the form of sensory signals for determining the attitude, position, and angular rates of the satellite. If failure of the onboard rate gyro or

accelerometer occurs, the lack of feedback can lead to instability of the satellite and loss of attitude determination.

[PROB4] ***Integrated attitude control and thermal management:*** Heat dissipation from onboard electronics and attitude control devices require an additional thermal management subsystem to ensure operational temperatures are maintained. Thermal management systems take up additional real estate in limited-space satellite enclosures and add additional weight, cost, and complexity. Combined attitude and thermal management systems have been proposed in the literature using fluid. However, results to indicate the effectiveness of the proposed system have not been produced.

1.4 Research Objectives

In response to the problem statement above, this dissertation focusses on the design and practical simulation of a satellite equipped with PFLA that overcomes the complexities and costs associated with traditional attitude control devices as examined in Section 1.1 while providing added benefits to small and large satellites.

From a practical perspective, the goal is to design an ACS that can achieve high pointing accuracy, agile slew rates, and perform large angle attitude maneuvers in the presence of model uncertainties, disturbances, and actuator faults. This dissertation examines the aforementioned primarily from the perspective of the hardware as opposed to the control algorithm as is traditionally examined in the literature.

[OBJ1] ***Attitude maneuver:*** Develop and apply a nonlinear voltage-driven control law to regulate the PFLA for performing attitude tracking maneuvers while subject to sensor noise, and optimize power consumption through actuator configurations.

[OBJ2] ***Novel actuator for attitude control:*** Design and develop a new form of actuator based on spherical design that eliminates restrictions with existing hardware and allows for active and passive stabilization about any arbitrary axis without singularities while reducing costs associated with traditional manufacturing methods.

[OBJ3] ***Integrated actuator and sensor for attitude control:*** Examine the ability to use a fluid dynamic actuator as a rate sensor for attitude determination in the event of rate gyro sensor failure.

[OBJ4] ***Satellite thermal management:*** Develop the PFLA as a combined attitude and thermal management system that can be used to transport thermal energy from onboard subsystems to the external space environment in order to maintain operating temperatures.

The development of advanced sensor technology and the desire for complex small satellite space mission requirements has increased the demand for high-performance attitude control devices at low cost. The lack of innovation in modern actuator hardware has limited the application of small satellites while there are numerous control algorithms proposed in the literature. Yet, control techniques derived in the literature do not consider digital signals such as voltage and pulse-width modulation (PWM), nor do they examine the physical capabilities of hardware during actuator saturation.

Researchers have often sought fault-tolerant control techniques to overcome actuator and/or sensor failures and have overlooked the performance capabilities of the hardware itself. Therefore, it is important to propose attitude control techniques from the perspective of the hardware in the presence of actuator and/or sensor failures.

The objective of this study is to show the performance enhancements gained from using fluid-based actuators for satellite attitude control so that future space missions can harness the benefits provided from fluid dynamic actuation.

1.5 Main Contributions

This dissertation presents an innovative control scheme for using fluid dynamic actuators for satellite attitude control. The study proposes the use of such a device for the ACS, from the hardware perspective, while considering actuator faults and peripheral attitude determination subsystem failures. Specifically, the following contributions are identified and expanded on based on objectives stated in Section 1.4.

1. *Attitude Stabilization with voltage law for PFLA actuator model (OBJ1 - CHAPTER 3)*

   A high-fidelity PFLA model is proposed that examines the viability of the actuator for attitude stabilization while considering the effects of sensor noise. A nonlinear voltage-driven control law is developed and the model is implemented into the control algorithm. The power consumption of the PFLA is also investigated for different actuator configurations.

2. *Attitude tracking maneuver using PFLA (OBJ1 - CHAPTER 3)*

   The PFLA is examined for agile satellite attitude tracking maneuvers using a voltage-driven control law and a power-optimal configuration. The technique presented in this dissertation is the first to consider the attitude maneuver problem using the PFLA while implementing a high –fidelity actuator model.

3. *Novel attitude control actuator (OBJ2 - CHAPTER 4)*

   The limitations of passive attitude stabilization have been recognized in the literature, and recent advancements in servo technologies have enabled research in spherical actuators for providing active attitude stabilization about infinite planes. A novel pumped fluid spherical actuator (PFSA) is presented herein, for the first time in the literature, which combines the advantages recognized from the PFLA and applies it to spherical design. The novel design allows for both active and passive attitude control while exhibiting all the advantages of the PFLA system.

4. *Attitude control in the absence of rate gyro information (OBJ3 - CHAPTER 4)*

   Examination of methods for determining attitude position from peripheral subsystems in the event of the failure of the attitude determination subsystem has become of increasing interest to researchers. Based on the attractive applications of the PFSA, and do to its unique performance capabilities, a method is proposed herein to use the PFSA as a rate gyro sensor in order to stabilize a satellite in the event of sensor failure.

5. *Integrated attitude and thermal management system (OBJ4 - CHAPTER 5)*

   The thermal management capability of the PFLA is extensively explored as a means of heat transport from peripheral electronics to maintain their operating temperatures without the need for large evaporator and condenser coils through fluid heat-pipe technologies. The method of using the PFLA as a combined thermal management and

attitude control system increases the mission capabilities for small satellite and can be extended to large satellite in order to eliminate the complexity of existing thermal management subsystems while simultaneously providing attitude control.

The approach for attitude control has changed very little since the launch of Sputnik I in 1957. However, with the cost associated with launching satellite into space, the modern era is diluted with small satellites due to their minimal space onboard launch craft. Needless to say, their small size limits their performance capability as their internal volume is allocated between payload and necessary subsystems for operation. By enabling further performance capabilities for small satellites while minimizing the volume occupied by vital subsystems would allow research to be carried out on innovative missions that require more complex payloads and attitude control. The research carried out in this dissertation is not limited to small satellites but rather allows for the advancement of small satellite missions that would otherwise be more difficult or impossible to attain without the PFLA/PFSA.

1.6 Thesis Outline

This thesis is structured as follows:

In CHAPTER 2, the mathematical models governing the PFLA actuator are presented, followed by the satellite attitude and kinematics equations that govern the rigid-body rotation of a satellite in space. The dynamic models are used in CHAPTER 3 with a developed nonlinear voltage-driven control algorithm that controls a practical voltage signal as opposed to a control torque. The problems associated with traditional control methods in regards to saturation are presented therein, and a model is proposed that alleviates impractical simulation results obtained when using theoretical control algorithms and attempts to address a disconnect that exists between theory and practice. The proposed model is then applied to the PFLA to examine the active attitude maneuver capability of the system that has not been addressed in the literature. The optimal power configuration is determined for the PFLA, and a power assessment is also presented. Furthermore, the fault-tolerant control of a satellite is examined from the perspective of the physical configuration of the actuators when a satellite is subject to extreme levels of sensor noise.

In the literature, one assumption is made when analyzing the PFLA for passive attitude stabilization. CHAPTER 4 introduces a novel pumped fluid spherical actuator (PFSA) that alleviates the necessity for assumptions of the PFLA and provides elevated performance for both active and passive attitude control that is not available in the literature. The proposed actuator is Patent Pending, and extensive simulation results have been presented herein to show the performance enhancements gained with the PFSA. Furthermore, to expand on the passive capabilities of PFSA, the actuator is introduced as a replacement for rate gyro sensors in the event of sensor failure.

In CHAPTER 5, the unresolved thermal management capability of the PFLA is thoroughly examined, and the thermal analysis results are presented as a basis for the thermal management capability of the PFLA and PFSA.

Lastly, the conclusions and future works of this study are presented in CHAPTER 6.

CHAPTER 2
ACTUATOR MODEL AND SATELLITE DYNAMICS

SPACE missions require effective attitude control systems (ACS) to ensure system reliability in the presence of model uncertainties, subsystem failures, and external disturbance. Precision attitude tracking requires robust control algorithm as well as actuators that provide accurate torque outputs that uphold the agile system requirements. In this study, we aim to address the satellite attitude control problem using a novel active fluid dynamic actuator otherwise known as the PFLA to provide agile maneuverability with minimal power consumption. Furthermore, the principals of fluid mechanics are applied in order to illustrate the fluid dynamics of the proposed actuator appropriately.

This chapter is organized as follows: In Section 2.1 the fluid dynamic actuator models and fluid theory are formulated with detailed motor dynamics, and the high-fidelity simulation model is introduced. In Section 2.2, the actuator configurations considered in this study are presented. Lastly, the fundamental dynamic and kinematic Euler equations of motion for a rigid body in a circular low Earth orbit (LEO) are presented in Section 2.3, followed by concluding remarks in Section 2.5.

2.1 Actuator Model

Herein the actuator dynamic model is developed in order to simulate the effects of the PFLA on the response of the satellite by providing an applied torque to control attitude. For the PFLA system, a brushless DC motor is used to drive the impeller inside a centrifugal pump which then regulates the fluid flow inside the loops. The torque generated by the fluid flow, in turn, drives the satellite attitude. This section formulates the equations governing the dynamics of the pump motor and the fluid dynamics.

2.1.1 PFLA/PFSA Motor Model

In order to investigate the performance of the proposed fluid dynamic actuator and examine its potential, the motor dynamics are presented. The dynamics of the DC-motor is represented by

$$J_m\dot{\omega}_{imp} + b\omega_{imp} = \tau_m \tag{2.1}$$

where J_m is the impeller moment of inertia, b is the motor viscous constant, ω_{imp} is the impeller angular velocity, and τ_m is the torque generated by the DC-motor that is directly proportional to the armature current, i_a, passing through the motor as described by Bialke [37]

$$\tau_m = K_t i_a \tag{2.2}$$

where K_t is the motor torque constant with units of V/rad/s.

The electrodynamic equation for the armature voltage of the DC-motor is governed by

$$v_a = L_a \frac{di_a}{dt} + R_a i_a + e_b \tag{2.3}$$

where L_a is the armature inductance, R_a is the armature resistance, and v_a is the applied armature voltage. For a constant flux as determined by the current flow through the stator windings, the voltage in the armature (back-EMF) e_b is directly proportional to the angular velocity of the motor shaft. Based on Faraday's Law of induction, the interaction between the magnetic field and the wound electrical coils inside the motor produces an electromotive force (EMF) that can be described by

$$e_b = K_b\omega_{imp} \tag{2.4}$$

where K_b is the back-EMF constant. This actuator motor model is distributed for the PFLA according the configurations in Section 2.2.

2.1.2 Fluid Dynamics Model

The torque generated by the brushless-DC motor transfers its energy to the fluid inside the loops of the PFLA. The motion of the fluid is governed by the established Navier-Stokes Equations (NSE) wherein the fluid is characterized by particular viscous stress terms. The NSE is a second-

order nonlinear differential equation that defines the fluid momentum for viscous flow and can be expressed as:

$$\rho g - \nabla p + \nabla \cdot \sigma_{ij} = \rho \frac{dV}{dt} \tag{2.5}$$

where $\sigma_{ij} = \begin{bmatrix} \sigma_{xx} & \sigma_{yx} & \sigma_{zx} \\ \sigma_{xy} & \sigma_{yy} & \sigma_{zy} \\ \sigma_{xz} & \sigma_{yz} & \sigma_{zz} \end{bmatrix}$ is the viscous stress tensor (shear stress) acting on any given infinitesimally small fluid element, ρ is the fluid density, p is the fluid pressure, V is the fluid velocity, and the gradient $\nabla = \frac{\partial()}{\partial x} + \frac{\partial()}{\partial y} + \frac{\partial()}{\partial z}$.

In other words, the NSE is *the gravitational force per unit volume + pressure force per unit volume + viscous force per unit volume = density × acceleration.* The NSE can be regarded as an application of Newton's second law $F = ma$ wherein force is the product of an object's mass times is acceleration. Eq. (2.5) can be expanded and written in componential form as:

$$\begin{aligned}
\rho g_x - \frac{\partial p}{\partial x} + \frac{\partial \sigma_{xx}}{\partial x} + \frac{\partial \sigma_{yx}}{\partial y} + \frac{\partial \sigma_{zx}}{\partial z} &= \rho \left(\frac{\partial u}{\partial t} + u \frac{\partial u}{\partial x} + v \frac{\partial u}{\partial y} + w \frac{\partial u}{\partial z} \right) \\
\rho g_y - \frac{\partial p}{\partial y} + \frac{\partial \sigma_{xy}}{\partial x} + \frac{\partial \sigma_{yy}}{\partial y} + \frac{\partial \sigma_{zy}}{\partial z} &= \rho \left(\frac{\partial v}{\partial t} + u \frac{\partial v}{\partial x} + v \frac{\partial v}{\partial y} + w \frac{\partial v}{\partial z} \right) \\
\rho g_z - \frac{\partial p}{\partial z} + \frac{\partial \sigma_{xz}}{\partial x} + \frac{\partial \sigma_{yz}}{\partial y} + \frac{\partial \sigma_{zz}}{\partial z} &= \rho \left(\frac{\partial w}{\partial t} + u \frac{\partial w}{\partial x} + v \frac{\partial w}{\partial y} + w \frac{\partial w}{\partial z} \right)
\end{aligned} \tag{2.6}$$

where p is the pressure. For incompressible Newtonian flow, as in the case of the fluid medium used in the PFLA the viscous stress are proportional to the element strain rates and the coefficient of viscosity μ. For Newtonian fluids μ is a thermodynamic property that varies with temperature and pressure; in general the viscosity of a fluid increases minutely with pressure and decreases with increasing temperature. The applied shear stress is also proportional to the velocity gradient and its generalization to three-dimensional viscous flow is governed by

$$\begin{gathered}
\sigma_{xx} = 2\mu \frac{\partial u}{\partial x} \quad \sigma_{yy} = 2\mu \frac{\partial v}{\partial y} \quad \sigma_{zz} = 2\mu \frac{\partial w}{\partial z} \\
\sigma_{xy} = \sigma_{yx} = \mu \left(\frac{\partial u}{\partial y} + \frac{\partial v}{\partial x} \right) \quad \sigma_{xz} = \sigma_{zx} = \mu \left(\frac{\partial w}{\partial x} + \frac{\partial u}{\partial z} \right) \\
\sigma_{yz} = \sigma_{zy} = \mu \left(\frac{\partial v}{\partial z} + \frac{\partial w}{\partial y} \right)
\end{gathered} \tag{2.7}$$

Since the fluid in the loops exhibit the nature of incompressible Newtonian fluid, the density and viscosity changes are considered negligible such that $\frac{\partial \rho}{\partial t} \approx 0$. This assumption results in the simplification of the mass continuity equation $\nabla \cdot V_{fl} = 0$. Substituting Eq. (2.7) into Eq. (2.6) and considering the characteristics of incompressible Newtonian fluid provides a more simple fluid momentum equation expressed by

$$\begin{aligned} \rho g_x - \frac{\partial p}{\partial x} + \mu\left(\frac{\partial^2 u}{\partial x^2} + \frac{\partial^2 u}{\partial y^2} + \frac{\partial^2 u}{\partial z^2}\right) &= \rho \frac{du}{dt} \\ \rho g_y - \frac{\partial p}{\partial y} + \mu\left(\frac{\partial^2 v}{\partial x^2} + \frac{\partial^2 v}{\partial y^2} + \frac{\partial^2 v}{\partial z^2}\right) &= \rho \frac{dv}{dt} \\ \rho g_z - \frac{\partial p}{\partial z} + \mu\left(\frac{\partial^2 w}{\partial x^2} + \frac{\partial^2 w}{\partial y^2} + \frac{\partial^2 w}{\partial z^2}\right) &= \rho \frac{dw}{dt} \end{aligned} \tag{2.8}$$

In compact form Eq. (2.8) can be reduced to

$$\rho g - \nabla p + \mu \nabla^2 V_{fl} = \rho \frac{\partial V}{\partial t} \tag{2.9}$$

The fluid motion inside the loops of the PFLA is modeled using computational fluid dynamics that solves the control volume using the NSE presented in Eq. (2.9).

In order for the PFLA to produce an applied torque on the satellite, the fluid dynamic actuator houses a centrifugal pump that regulates the fluid within the loop. The use of a centrifugal pump is ideal for driving the fluid as the loops are fully sealed. As the flow enters the pump casing through its inlet, fluid particles within the pump are expelled from the tips of the impeller blades at high velocities into the volume between the casing wall and the blade tips. The fluid particles collide with the inner casing of the pump and are decelerated thereby lowering the kinetic energy of the fluid and inversely increasing the pressure energy of the pump. Unlike friction that wastes energy, the decrease in kinetic energy consequently increases the pressure energy of the flow. In the preservation of the conservation of energy, prior to the flow exiting the pump, the fluid particles slow down to match the velocity at the inlet, given that the inlet and exit pipe diameter remains unchanged. As the fluid enters the loops, the fluid velocity relative to the wall is zero. This is a characteristic for all viscous fluid flows and is referred to as the *no-slip condition.*

Generally, Bernoulli's equation can be used to estimate the fluid velocity through the pump's channel and is governed by

$$p_{in} = p_{out} + \Delta p_{loss} - n\Delta p_{pump} \tag{2.10}$$

where for a closed system, the pressure loss is $\Delta p_{loss} = n\Delta p_{pump}$ where n is the number of active pumps. The pressure loss due to the fluid frictional effects between the fluid and channel walls can be estimated using the following formulation

$$\Delta p_{loss} = f\left(\frac{l}{D}\right)\left(\frac{\rho}{2}\right)V_{fl}^2 \tag{2.11}$$

where D is the hydraulic diameter of the channel defined through $D = 2wh/(w+h)$, V_{fl} is the fluid velocity, where w and h are the width and height of the cross-sectional area, respectively, and l is the channel length. The viscous behaviour of the Newtonian fluid inside the loops of the PFLA can be characterized by the dimensionless *Reynolds number* $Re = \frac{\rho V_{fl} D}{\mu}$ is the dimensionless Reynolds number defining the flow characteristics (laminar, transient, and turbulent) where D is the cross-sectional diameter of the loop and the same as the hydraulic diameter. In order for the PFLA to provide effective torque the fluid inside the loops must exhibit laminar properties ($Re \leq 2100$) wherein the critical Reynolds number is governed by

$$Re_{crit} = 16.5\sqrt{\frac{R}{D}} \tag{2.12}$$

where $R/D \geq 10^{-3}$ and R is the loop radius.

To determine the fluid velocity, rotating within the loops, as produced by the pump the theoretical foundation (Pump theory) of energy conservation in a centrifugal pump is examined. When a pump operates, the shaft accumulates energy in the form of mechanical energy. At the impeller, this energy is converted to internal (static pressure) and kinetic energy (velocity). The net torque experienced by the satellite is equal to and opposite in direction to the torque generated by the fluid rotation inside the loops. By using velocity triangles for the flow at the impeller inlet and outlet, the necessary pump equations are obtained.

2.1.3 Fluid-Impeller Interaction Model

To help simplify the mathematical model of the fluid dynamic system, the following five assumptions have been made:

i. The flow entering the pump has no inlet rotation. The lack of inlet rotation is a valid assumption as the impeller comprises radial vanes and the flow enters through a straight tube into rotation boundary inside the pump; this indicates the blade outlet angle is 90°, suggesting that the fluid is not rotating prior to entering the impeller.

ii. No slip occurs at the impeller blade. Slip is a condition that arises when the flow angle is smaller than the blade angle. Due to the miniature nature of the impeller, the connection between the flow angle and blade angle is neglected suggesting that the flow does indeed follow the blade. This assumption is one that is made in the derivation of the fundamental Euler's pump equation [38].

iii. The fluid velocity remains unchanged across the inlet to the outlet of the impeller. Typically, as the fluid passes across the impeller vanes, its velocity increases from the impeller inlet to its tip (outlet) due to the addition of energy to the fluid. However, since the radial impeller is quite small with vanes of length < 10 mm, the fluid velocity increase from the hub to the tip of the impeller is considered negligible.

iv. Flow friction inside the impeller housing due to surface roughness is neglected. Flow friction occurs where the fluid is in contact with the impeller and interior surface of the impeller housing. The magnitude of the friction loss depends on the roughness of the interior surface and the fluid velocity relative to the surface. For this study, the housing of the impeller is polished aluminum, and thus the flow friction with regards to surface roughness is negligible.

v. The fluid dynamic loops are fully filled with fluid. This assumption ensures that no sloshing of the fluid affects the performance of the pumps and also, no sloshing motion will affect the moment of inertia of the satellite.

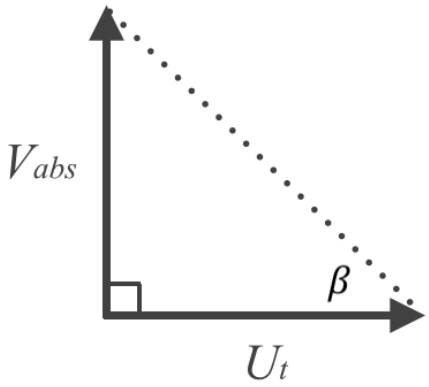

Figure 2.1: Pump Inlet Velocity Triangle

For a radial impeller with velocity triangle depicted in Figure 2.1, the pump inlet area can be calculated by

$$A_{in} = 2\pi r_{in} b_{in} \tag{2.13}$$

where r_{in} is the radial position of the impeller's inlet edge and b_{in} is the blade's height at the inlet. The angular fluid flow rate entering the loops is thus expressed as

$$\omega_{fl} = \frac{Q_{imp}}{A_{fl} r_{fl}} \tag{2.14}$$

where Q_{imp} is the volumetric flow rate entering the impeller governed by

$$Q_{imp} = V_m A_{in} \tag{2.15}$$

and the meridional velocity V_m is equivalent to the absolute fluid velocity V_{abs} when considering no inlet rotation, i.e. $V_m = V_{abs}$. Then, the fluid angular velocity inside the fluid dynamic actuator can be related to the discharge flow rate by defining the absolute fluid velocity V_{abs} as

$$V_{abs} = U_t \tan \beta \tag{2.16}$$

where β is the relative flow angle, and the tangential velocity U_t is calculated using

$$U_t = r_{in} \omega_{imp} \tag{2.17}$$

where ω_{imp} is the angular velocity of the impeller.

2.1.4 Fluid Torque Model

As the flow is discharged from the pump into the enclosed loop, the frictional interaction between the fluid and loop's inner surface causes energy dissipation through shear stress acting on the loop surface that must be considered Kumar [29]

$$\varepsilon_{fl} = \frac{1}{8} f_d \rho \left(\omega_{fl} r_{fl}\right)^2 \tag{2.18}$$

where f_d is the frictional drag coefficient, r_{fl} is the mean radius of the fluid loop, and ρ is the density of the fluid. For laminar flow ($R_e < 2100$), as in the case herein, f_d is obtained from Cengel [39]

$$f_d = \frac{64}{R_e} \tag{2.19}$$

The friction torque opposing the fluid torque inside the loop is adopted from Kumar [29] and modified as

$$\tau_{ff} = -\alpha_f \omega_{fl} \tag{2.20}$$

where $\alpha_f = \pi \varepsilon_{fl} {r_{fl}}^2 D \eta$ and $\eta = 2\pi$ defines fully filled loops. The frictional forces of the fluid dynamic actuator are mathematically discretized into three parameters; kinetic friction inside the fluid dynamic loops, and, viscous and coulomb friction that are developed in the motor. The viscous friction varies with the speed of the shaft, while the coulomb friction is a constant with polarity dependence on the direction of rotation Bialke [37] or the motor. The former is responsible for the power consumption in the wheel-drive electronics of the actuator assembly; an increase in fluid velocity constitutes a proportional increase in viscous friction that in turn leads to a notable increase in power consumption. The coulomb friction torque is responsible for irregularities and finite attitude errors in the attitude control system. These friction factors must be considered when developing nonlinear control algorithms Sidi [40]. A simplified model of the friction torque in terms of the coulomb and viscous effects is given by Wertz [41]

$$\tau_{mf} = N_c sgn(s) + f_d \omega_{imp} \tag{2.21}$$

where $N_c = 7.06e^{-4}$ Nm is the coulomb friction coefficient, $f_d = 1.21e^{-6}$ Nm/rpm is the viscous friction coefficient, and ω_{imp} is the wheel speed in revolutions per minute (rpm). Therefore, the total friction torque affecting the fluid dynamic loop assembly is governed by

$$\tau_f = \tau_{ff} + \tau_{mf} \tag{2.22}$$

The net torque generated by the pump motor can be computed as the torque produced by the motor, less any frictional effects expressed as

$$\tau_{fl} = -(\tau_m + \tau_f) \tag{2.23}$$

2.2 Actuator Configurations

The satellite's actuator configuration plays a vital role in providing maneuverability control torques. For any particular mission, the requirements will dictate the configuration of the attitude control subsystem. For instance, a mission may only require 1-DOF whereby only a single actuator will be used along the axis that is to be controlled or, complete 3-DOF may be required if the mission requires more complex attitude control capabilities. Regardless, an infinite number of configurations exist to set up the actuators.

Various configurations exist in the literature as examined by Ismail and Varatharajoo [42] to determine the configuration with optimal accuracy performance. Their analysis examined 19 varying configurations using three and four reaction wheels to identify the optimal orientation with regards to power consumption and angular momentum capabilities. Their results concluded that the standard three-wheel configuration of actuators positioned with their torque directions along the primary axes provides optimal attitude pointing accuracy of < 0.001°; however, no notable difference was observed for the generated angular momentum of the various cases. The optimal three-wheel configuration fundamentally inherits a catastrophic failure in the case of one wheel failure and therefore is not a suitable configuration for satellite missions [40].

In agreement with several accounts in the literature [43-46] where four reaction wheels are used in a pyramid configuration, results of [42] indicate that the pyramid configuration is neither an optimal nor a worst case scenario configuration; its advantage lies in the symmetry it poses along the three primary axes in case of an actuator failure [43].

The investigations carried out for the PFLA examine two actuator configurations; the standard 3 orthogonal actuators plus one 45° skew for redundancy, and the standard pyramid with 4 actuators. Henceforth, in the context of this thesis, the former configuration will be referred to as S4 while the latter P4. Our focus is on analyzing and validating the feasibility of the proposed

PFLA for nanosatellite while subjecting the system to practical sensor-noise fault cases. The actuator configurations selected for study allow for the examination of fault case scenarios and the practical implementation of the PFLA system.

2.2.1 S3 Configuration

The S3 structure as illustrated in Figure 2.3 is the most basic actuator configuration. Three actuators are positioned with their angular momentum axes directed along the primary pitch, roll, and yaw axes of the satellite.

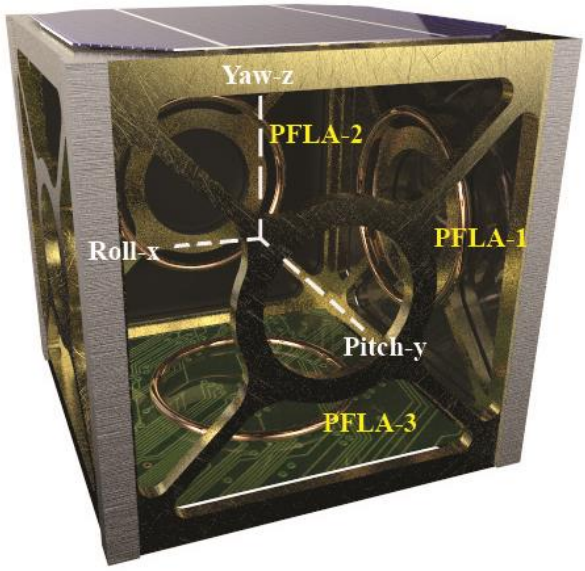

Figure 2.2: S3 Configuration

The advantage of this configuration is such that control torques are provided directly about the primary axes. However, the lack of a redundant actuator does not provide a fault tolerant approach in the event of one failed actuator. The torque distribution matrix of each actuator about its axis is governed by

$$A_{act} = \begin{bmatrix} 1 & 0 & 0 & 0 \\ 0 & 1 & 0 & 0 \\ 0 & 0 & 1 & 0 \end{bmatrix} \tag{2.24}$$

2.2.2 S4 Configuration

The S4 structure as illustrated in Figure 2.3 is the most widely used actuator configuration in practical satellite applications and is an adaptation from the S3. In S4, three actuators are positioned with their angular momentum axes directed along the primary pitch, roll, and yaw axes of the satellite. The fourth actuator is positioned at a 45° skewed angle ($\alpha° = \beta° = 45°$).

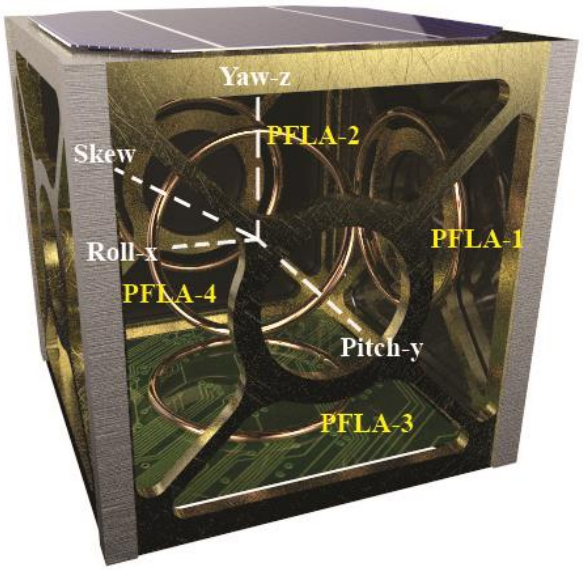

Figure 2.3: S4 Configuration

This configuration provides the highest attitude pointing accuracy [42], and the existence of the redundant actuator provides a fault tolerant approach in the event of one failed actuator as it provides componential torques along all three major axes. Another advantage of this configuration is the limited space that is required within the body of a satellite as all four actuators may be condensed around the center of rotation of the satellite. The torque distribution matrix of each actuator is governed by

$$A_{act} = \begin{bmatrix} 1 & 0 & 0 & -\cos\beta°\cos\alpha° \\ 0 & 1 & 0 & -\cos\beta°\sin\alpha° \\ 0 & 0 & 1 & \sin\beta° \end{bmatrix} \tag{2.25}$$

In S4, the skewed actuator is ideally positioned at 45° to provide 50% torque compensation in the x and y-axes and 71% compensation along the z-axis in the event of an actuator failure. This

ensures that the satellite maintains fully-actuated control however with an increase in settling time as only a portion of the necessary torque is available from the redundant wheel.

2.2.3 P4 Configuration

The P4 structure is one that has formed the basis of the control moment gyro (CMG) configuration. It is structured such that angular momentum vectors of four actuators are collinear to the edges of a four-sided pyramid as demonstrated in Figure 2.4.

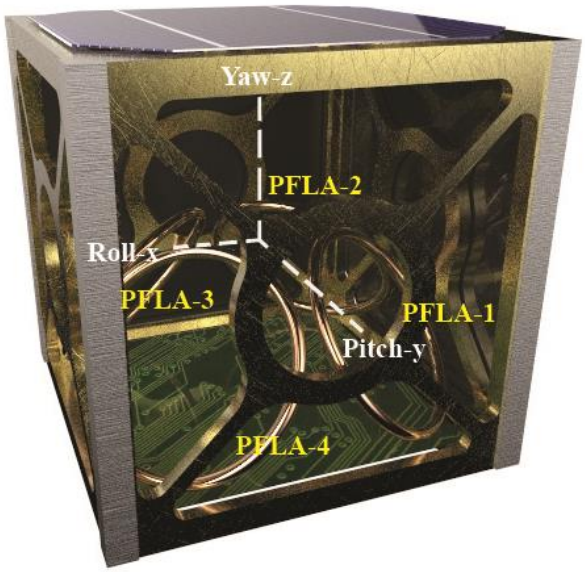

Figure 2.4: P4 Configuration

Although this configuration was less adopted in the past, it has become more widely accepted due to its stronger coupling torques and lower power consumption as compared with other traditional configurations such as the S4. The pyramid configuration has been extensively analyzed in the literature for reaction wheel actuators and found to have an optimal skew angle of $\alpha° = \beta° = 54.74°$ [47]. The torque distribution matrix for each actuator in the P4 configuration is defined by

$$A_{act} = \begin{bmatrix} cos\,\beta°\,sin\,\alpha° & -cos\,\beta°\,sin\,\alpha° & -cos\,\beta°\,sin\,\alpha° & cos\,\beta°\,sin\,\alpha° \\ -cos\,\beta°\,cos\,\alpha° & -cos\,\beta°\,cos\,\alpha° & cos\,\beta°\,cos\,\alpha° & cos\,\beta°\,cos\,\alpha° \\ sin\,\beta° & sin\,\beta° & sin\,\beta° & sin\,\beta° \end{bmatrix} \quad (2.26)$$

2.3 System Model

The nonlinear equations of motion of the proposed system comprising of a *rigid body satellite and fluid actuators* are formulated. The proposed system is assumed to be orbiting in a circular orbit around a celestial body, in the case considered herein, Earth.

2.3.1 Coordinate Frames

To represent the dynamics of the satellite in a circular orbit, an Earth-centered inertial (ECI) coordinate frame is considered, as shown in Figure 2.5. The ECI frame is denoted by $\mathcal{I}$-$X_I Y_I Z_I$ with its origin located at the center of the Earth. The X-axis passes through the vernal equinox and the Z-axis is directed towards the celestial North Pole. The Y-axis completes the right-hand triad. To describe the orbital frame, we define a local vertical local horizontal (LVLH) orbital reference frame $\mathcal{O}$-$x_0 y_0 z_0$. The center of the frame is located at the center of the satellite body with the x_0-axis directed along the satellite's orbital motion, the z_0-axis pointing towards the center of the Earth, and y_0-axis completing the right-hand triad that is in the direction opposing the satellite angular velocity and normal to the orbital plane. The principal body-fixed coordinate frame of the satellite is denoted by $\mathcal{B}$-xyz, with its origin located at the center of mass of the satellite. The roll, pitch, and yaw maneuvers and referenced by the satellite x, y, and z-axes, respectively.

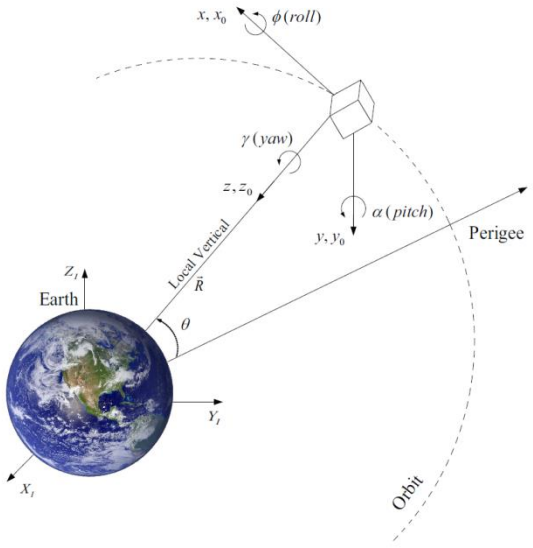

Figure 2.5: Frames of Reference

2.3.2 System Dynamics

The equation of motion of the proposed system is expressed as

$$\dot{H} + \omega_{BI}^{B} \times H = \tau_e \tag{2.27}$$

Where H is the total system angular momentum, $\omega_{BI}^{B} \in \mathbb{R}^{3\times1}$ is the angular velocity of the satellite relative to the inertial frame, expressed in the body frame, and $\tau_e \in \mathbb{R}^{3\times1}$ denotes any external disturbances acting on the system. We define $J_s \in \mathbb{R}^{3\times3}$ is the satellite moment of inertia (excluding the actuators), $J_{fl} \in \mathbb{R}^{4\times4}$ is a diagonal matrix defining the axial moments of inertia of the PFLA about the principal axes, and $J_{fl,sum} \in \mathbb{R}^{4\times4} = \begin{bmatrix} \sum_{\varsigma=1}^{3} J_{x_\varsigma} & 0 & 0 \\ 0 & \sum_{\varsigma=1}^{3} J_{y_\varsigma} & 0 \\ 0 & 0 & \sum_{\varsigma=1}^{3} J_{z_\varsigma} \end{bmatrix}$ is the total axial moment of the PFLA. H denotes the total angular momentum of the satellite expressed in $\mathscr{B}$, and defined by

$$H = H_s + A_{act} H_{fl} \tag{2.28}$$

where $H_s = J_s \omega_{BI}^{B}$ is the angular momentum of the satellite (excluding the actuators), and the angular momentum of the fluid, $H_{fl} \in \mathbb{R}^{4\times1}$, is defined by

$$H_{fl} = J_{fl}\omega_{fl} + J_{fl,sum} A_{act}^{T} \omega_{BI}^{B} \tag{2.29}$$

where $\omega_{fl} \in \mathbb{R}^{4\times1}$ represents the angular velocity of the fluid. The dynamics of the PFLA/PFSA is expressed as

$$J_{fl}\dot{\omega}_{fl} = \tau_{fl} \tag{2.30}$$

The nonlinear differential equation of motion describing the attitude dynamics of a rigid satellite controlled by PFLA/PFSA can be written as

$$\left(J_s + A_{act}J_{fl,sum}\right)\dot{\omega}_{BI}^{B} = -\omega_{BI}^{B\,\times}\left(J_s\omega_{BI}^{B} + A_{act}J_{fl}\omega_{fl} + A_{act}J_{fl,sum}A_{act}^{T}\omega_{BI}^{B}\right) - A_{act}\tau_{fl} + \tau_e \tag{2.31}$$

where $A_{act} \in \mathbb{R}^{3\times4}$ is a projection matrix whose columns contain the axial unit vectors of the four PFLA and their influence on the angular acceleration of the satellite; and $\omega_{BI}^{B\,\times}$ is the skew-symmetric matrix defined to simplify the cross-product operation and given by

$$\left[\omega_{BI}^{B}{}^{\times}\right] = \begin{bmatrix} 0 & -\omega_{BI_3}^{B} & \omega_{BI_2}^{B} \\ \omega_{BI_3}^{B} & 0 & -\omega_{BI_1}^{B} \\ -\omega_{BI_2}^{B} & \omega_{BI_1}^{B} & 0 \end{bmatrix} \tag{2.32}$$

2.3.3 Attitude Kinematics

The satellite attitude kinematic equations relate the time derivatives of the attitude coordinates to the angular velocity vector. Various parameterization methods exist in the literature for defining the kinematic equations. These representations include Euler angles, Cayley-Rodrigues parameter, modified Rodrigues parameters, and quaternions (Euler parameters). To avoid the inherent problem associated with singularities when using Euler angles, in this study, we adopt the quaternion to define the attitude kinematics of the satellite. The relationship between quaternions and Euler parameters is expressed by the following equation:

$$\bar{q} = \begin{bmatrix} \bar{e}\, sin(\varphi_q/2) \\ cos(\varphi_q/2) \end{bmatrix} = \begin{bmatrix} q_v \\ q_4 \end{bmatrix} \tag{2.33}$$

where φ_q is the principal angle, and $\bar{e} = [e_1\ e_2\ e_3]^T$ defines the principal axis associated with Euler's Theorem (${e_1}^2 + {e_2}^2 + {e_3}^2 = 1$). The Euler parameters representing the orientation of the satellite body frame, $\mathscr{B}$, with respect to the orbital frame, $\mathscr{O}$, are denoted by $q_v \in \mathbb{R}^{3\times1} = [q_1\ q_2\ q_3]^T$ and q_4 which is the scalar portion of the quaternion, and satisfy the constraint ${q_v}^T q_v + {q_4}^2 = 1$. The nonlinear differential equations governing the attitude kinematics of a satellite represented as quaternions can be defined by

$$\begin{bmatrix} \dot{q}_v \\ \dot{q}_4 \end{bmatrix} = 0.5 \begin{bmatrix} q_4 I + [{q_v}^{\times}] \\ -{q_v}^T \end{bmatrix} \omega_{BO}^{B} \tag{2.34}$$

where $I \in \mathbb{R}^{3\times3}$ is the identity matrix, and $[{q_v}^{\times}]$ is a quaternion skew-symmetric matrix given by

$$[{q_v}^{\times}] = \begin{bmatrix} 0 & -q_3 & q_2 \\ q_3 & 0 & -q_1 \\ -q_2 & q_1 & 0 \end{bmatrix} \tag{2.35}$$

The angular velocity of the body-fixed frame, $\mathscr{B}$, with respect to the inertial frame, $\mathscr{I}$, can be expressed as

$$\omega_{BI}^{B} = \omega_{BO}^{B} + \omega_{OI}^{B} \tag{2.36}$$

where $\omega_{OI}^{B} = R_{O}^{B}[0 \quad -\omega_0 \quad 0]^T$ is the orbital angular velocity of the satellite expressed in the body frame, $\mathscr{B}$. $\omega_{OI}^{B} \in \mathbb{R}^{3\times1}$ is obtained by rotating the angular velocity in, $\mathscr{O}$, using the direction cosine matrix transformation $R_{O}^{B} \in \mathbb{R}^{3\times3}$ which expresses the orientation of the satellite body-fixed frame with respect to the orbital frame in terms of quaternions as given by

$$R_{O}^{B} = ({q_4}^2 - {q_v}^T q_v)I + 2q_v {q_v}^T - 2q_4[{q_v}^\times] \tag{2.37}$$

The magnitude of the orbital angular velocity for a circular orbit is $\omega_0 = \sqrt{\mu_e / R_{orbit}^3}$, where μ_e is the gravitational parameter of Earth ($\mu_e = 3.986\text{e}14\ \text{m}^3/\text{s}^2$), and R_{orbit} represents the orbital radius of the satellite as measured from the center of the Earth.

2.3.4 External Disturbances

The environmental factors existing in space are a cause for satellite to be subjected to external forces including gravity gradient, solar radiation pressure, aerodynamic drag, and other disturbance forces. These external forces are translated into torques when they act on the rigid body satellite. This total external torque is defined by τ_e. However, depending on the satellite orbit as well as its size, some environmental factors are more prominent than others. For the class of satellite under consideration herein, primarily nanosatellite (1-10kg), the solar radiation pressure and aerodynamic drag are not of vital significance as there is not much wetted surface area due to the small size of the satellite. The total external disturbance torque acting on the satellite is represented by the magnitude of a sinusoidal disturbance torque herein. In order to analyze the performance of the PFLA/PFSA the external disturbance torque has been adopted from [48] as

$$\tau_e = \begin{bmatrix} 0.5\,sin(0.8t) \\ 0.5\,cos(0.5t) \\ 0.5\,cos(0.3t) \end{bmatrix} \times 10^{-5}\ [Nm] \tag{2.38}$$

2.4 Simulation

To facilitate a high-fidelity simulation that performs in the same manner as actual hardware, hardware-in-the-loop (HITL) performance results of the brushless DC motor were obtained from Patel [27] and used to generate a simulated motor in Simulink. The simulated motor model uses a Rotational Electromechanical Converter (REC) to simulate the DC-motor performance. The REC represents an ideal electromechanical energy conversion wherein the constant of proportionality $K_t = K_m$ and $K_t = 7.38 \times 10^{-3} \frac{V \cdot sec}{rad}$. A current sensor and an ideal rotational motion sensor are implemented in the motor circuit Figure 2.7 in order to obtain the power consumption, the feedback loop for the motor impeller angular velocity, and the feedback loop for the motor torque in order to ensure a closed-loop simulation with sensor feedback. The model also uses a rotational friction block to account for the viscous and coulomb friction present in the actual motor. The feedback loop of the satellite model is subjected to sensor noise levels as per the rate gyro sensor in Table 3.1 as depicted in Figure 2.6.

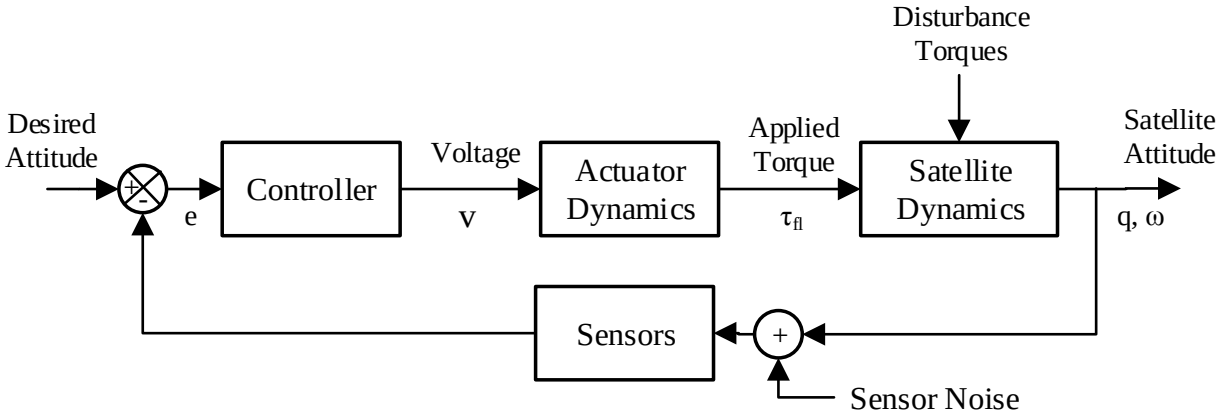

Figure 2.6: Satellite & Actuator Block Diagram

The saturated voltage defined by the control law is input to the motor model and the results in sensor feedback signals that simulate the effects of a rate gyro and magnetometer for attitude control. The complete simulation provides an accurate depiction of the PFLA model. This model, illustrated in Figure 2.7, alleviates all errors from commutation packet losses during HITL testing and ensures a continuously accurate and ideal signal from the PFLA motor.

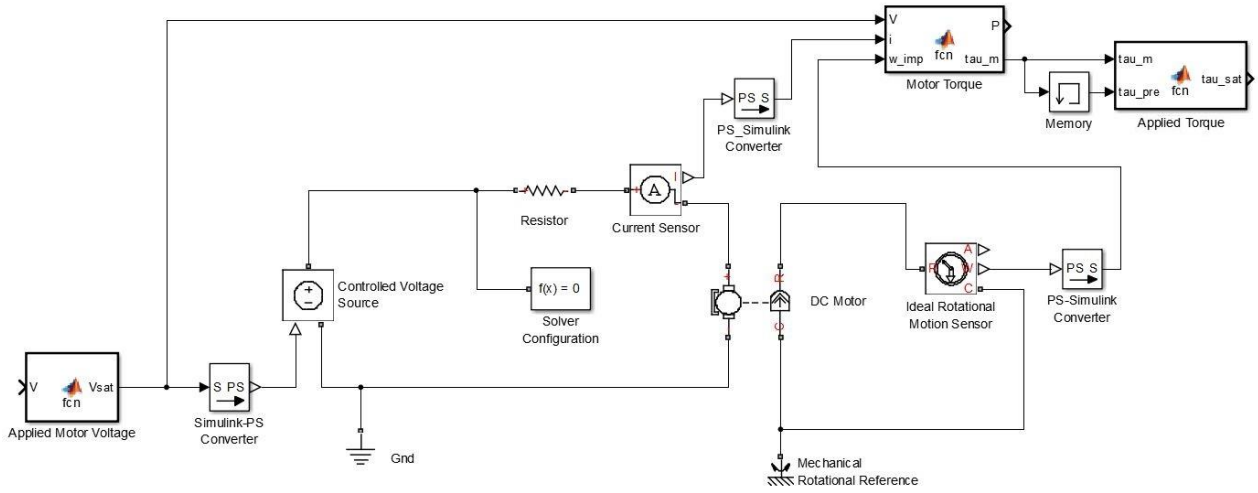

Figure 2.7: High-Fidelity Motor Model with Actuator Saturation

The hardware performance parameters of the motor (pump) used in the high-fidelity motor model are specified in Table 2.1.

Table 2.1: Pump Specifications

Motor & Pump Parameter	Value
Maximum Operating Voltage	12 VDC
Max Power Consumption	7.1 W
Maximum Flow Rate (From Experiment)	1750 ml/min
Impeller Velocity	[-570 570] rad/s
J_m, Impeller Inertia (SolidWorks CAD model)	$1e^{-7}$ kg·m^2
Volumetric Flow Rate	$2.917e^{-5}$ m^3/s
Output Pressure @ Max Flow Rate (Datasheet)	5.5 psi
Ethylene Glycol (Density; Viscosity)	1110 kg/m^3; $6.2e^{-2}$ Pa·s

The working fluid has been selected as Ethylene Glycol (antifreeze) for its limited thermal expansion within the operational temperatures of the study henceforth and for its similarity in viscosity to that of water; the selected TCS-M400S micropump (specifications provided in Table 2.1) provides optimal performance using fluids with similar viscosities to that of water.

The model is also used to determine the power consumption by the motor during the attitude maneuvers considered in this study. By integrating a current sensor into the circuit, the power

consumption of the DC motor is obtained by simply multiplying the current drawn by the motor by the differential voltage across its terminals as given by the linear equation

$$P_w = v_a i_a \tag{2.39}$$

The power consumption of the PFLA has not yet been studied in the literature, and this performance measure will examine the feasibility of the proposed actuator as a viable ACS.

2.5 Conclusions

In this chapter, the governing equations of motion are presented to formulate the necessary control algorithm that will be addressed in Section 3.2. The formulation of the fluid dynamic model was mathematically simplified through assumptions to save computational costs that would be encountered if a full set of Navier-Stokes fluid dynamic equations were otherwise used. The attitude control problem was assessed from the perspective of varying actuator configurations to determine their optimal arrangements used in the literature that will be considered henceforth in this study. A high-fidelity PFLA motor model was introduced, and the performance of the simulated motor model was compared against results obtained in HITL testing to ensure its validity and accuracy in subsequent chapters. The model incorporates rate sensors as used in real applications in order to obtain feedback information that is then analyzed by the attitude control board on the satellite. The sensor feedback is subjected to nominal noise levels as per the sensor data sheets. This model is implemented in the simulations conducted for the PFLA/PFSA and can be adopted for use in reaction wheel simulations by simply altering the circuit and motor performance measures.

CHAPTER 3
ATTITUDE MANEUVERS USING PFLA

SATELLITES operate similar to the human body. Just as the body relies on its primary motor cortex to generate neural impulses that control the executions of movement, satellites rely on their actuators and control algorithms to reorient and reposition themselves in space. The attitude maneuver problem dates back to the launch of the very first pioneered satellites. To maneuver in space and ensure the satellite remains on its trajectory if subjected to disturbance forces existent in the space environment, a control mechanism and control algorithm is required. The control algorithms play the role of the primary motor cortex and send digital signals to command the actuators - that act as the arms and legs of the satellite. Satellite attitude maneuvers require an active method to drive the actuators, as in the case considered in this chapter.

The application of actuators as attitude control systems onboard satellite allow for the execution of slew maneuvers during the lifetime of the mission. Slew maneuvers can be defined as the changing of the orientation of a satellite. This includes stabilizing and/or redirecting a satellite in another direction (point-to-point maneuver henceforth referred to as P2P), or following a predetermined track (attitude tracking maneuver or ATM). In practical missions, the imperfect deployment of a satellite from the launch shuttle can induce initial tipoff rotational rates which may introduce large angle tumbling motions if it is not actively controlled. In general, it is required to know the satellite attitude at all times for feedback controls [49]. The problem of attitude maneuver is further complicated by uncertainties of satellite mass and inertia properties due to payload motion, rotation of solar arrays, and fuel consumption, among other variables.

Innumerable studies have been conducted in the literature that examine, from the very basics to the most complex, of algorithms that will give purpose to the actuators existence to perform slew maneuvers. These algorithms range from the basic proportional, integral, and derivative (PID) to the most complex Neural Network-based control algorithms. However, very few studies actually consider the actuator model itself. It is important for attitude control laws to consider the

performance of the actuators as control input magnitude and rate saturations are physical limitations that must be taken into account for practical applications. The controller designer must address this issue as it may lead to instability or unacceptable performance measures of the actuator device. In the study herein, we develop a non-linear voltage driven control algorithm and validate the performance of the PFLA system.

To the best of the author's knowledge, in the literature, the PFLA has only been used as a device to address the attitude maneuver problem. The objective of the underlying study is aimed to propose the novel actuator for the purpose of attitude maneuvers requiring agile reorientation performances of up to 10°/s [50]. Furthermore, this study provides a complete analysis of a satellite Attitude Control System (ACS) for P2P and ATM and integrates a high-fidelity motor model as presented in Section 2.1.1. The attitude maneuver performance of the PFLA is also addressed with consideration of sensor noise to determine the power consumption for the proposed actuator. Furthermore, a voltage-driven nonlinear robust control law is proposed that unlike traditional laws does not directly control torque but rather drives the applied voltage for the pumps.

This chapter begins by introducing the mathematical models governing the attitude maneuver problem in Section 3.1; the voltage-driven control algorithm in presented in Section 3.2. Section 3.3 examines the performance of the PFLA for attitude maneuvers with the implementation of a torque interface between the actuator and the satellite that has not been addressed in the literature. The proposed model is applied to the PFLA; the performance of the PFLA is measured for attitude stabilization on S3; the PFLA is then presented as a method for attitude tracking maneuvers on P4; the effects of elevated levels of sensor noise are examined on the performance of the PFLA using S4 and P4, and the power-optimal configuration is viewed from the perspective of hardware. Lastly, the conclusions of the study are presented in Section 3.4.

3.1 Satellite Attitude Tracking Model

In the case of maneuvering about a desired trajectory, the target attitude of the satellite in the desired frame $\mathscr{B}_\mathrm{d}$ with respect to the orbital LVLH frame $\mathscr{O}$ is defined by the orientation of the desired quaternions $q_{vd} \in \mathbb{R}^{3\times1}$ and $q_{4d} \in \mathbb{R}$ that satisfy the constraint ${q_{vd}}^T q_{vd} + {q_{4d}}^2 = 1$. To define the appropriate error dynamics, let $\omega_d \in \mathbb{R}^{3\times1}$ denote the angular velocity of the desired frame with respect to the orbital frame, expressed in the desired frame. Here, we assume that there exist known, finite constants $c_1, c_2 > 0$, such that $\|\omega_d\| \leq c_1$ and $\|\dot{\omega}_d\| \leq c_2$ have an upper bound for all $t \geq 0$. To address the attitude maneuver problem, we define the quaternion error $q_{ve} \in \mathbb{R}^{3\times1}$ and $q_{4e} \in \mathbb{R}$ as the relative orientation between the body-fixed frame $\mathscr{B}$, and the desired reference frame $\mathscr{B}_\mathrm{d}$, and can be computed from the formulation described in [51] as

$$\begin{aligned} q_{ve} &= q_{4d}q_v - q_4 q_{vd} + [q_v{}^\times]q_{vd} \\ q_{4e} &= q_{4d}q_4 + {q_{vd}}^T q_v \end{aligned} \tag{3.1}$$

where ${q_e}^T q_e + {q_{4e}}^2 = 1$. The respective rotation matrix $R_e = R(q_{ve},\, q_{4e}) \in SO(3)$ is expressed by

$$R_e = ({q_{4e}}^2 - {q_{ve}}^T q_{ve})I + 2q_{ve}{q_{ve}}^T - 2q_{4e}[q_{ve}{}^\times] \tag{3.2}$$

where R_e has properties ${R_e}^T R_e = 1$, $\|R_e\| = 1$, $det(R_e) = 1$, and $\dot{R}_e = -[\omega_e{}^\times]R_e$. To compute the first derivative of the rotation matrix, we define the relative angular velocity error $\omega_e \in \mathbb{R}^{3\times1}$ as

$$\omega_e = \omega_{BI}^B - R_e\omega_d \tag{3.3}$$

wherein the first derivative of Eq. (3.3) is

$$\dot{\omega}_e = \dot{\omega}_{BI}^B - R_e\dot{\omega}_d + [\omega_e{}^\times]R_e\omega_d \tag{3.4}$$

The respective governing relative attitude error kinematic equations are governed by

$$\begin{bmatrix} \dot{q}_{ve} \\ \dot{q}_{4e} \end{bmatrix} = 0.5 \begin{bmatrix} q_{4e}I + [q_{ve}{}^\times] \\ -{q_{ve}}^T \end{bmatrix} \omega_e \tag{3.5}$$

The governing equations of motion provided in this section define the attitude rotational motions of a satellite. In order to provide P2P and ATM capabilities, a control algorithm must be devised that will control the dynamics of the satellite by actively controlling the motor voltage of the PFLA and is provided subsequently.

3.2 Nonlinear Voltage-Driven Control Law

In this section, we present the voltage-driven nonlinear control algorithm for a rigid body satellite equipped with PFLA/PFSA and subjected to uncertainties in mass moment of inertia and actuator saturation limits. A nonlinear sliding mode controller is developed to account for actuation voltage and fluid frictional effects exhibited by the PFLA/PFSA. This solution to the attitude maneuver problem is described by quaternions and avoids the singularity and chattering problems generally associated with sliding mode control techniques.

The voltage-driven control law commanding the motors of the PFLA and PFSA is governed by

$$v_a = K_m \omega_{imp} + \frac{R_a}{K_t}\left(A_{act}^T \tau_c + \tau_{ff}\right) \tag{3.6}$$

where the motor and fluid dynamic parameters can be found in Section 2.1.

$$\tau_c = -\varkappa_1 S - \varkappa_2 \cdot sgn(S) - N \tag{3.7}$$

where $\varkappa_1, \varkappa_2 > 0$ are design parameters and

$$N = -\left(J_s + A_{act}J_{fl,sum}\right)^{-1}\left(\omega_{BI}^{B\times}\left(J\omega_{BI}^B + A_{act}J_{fl}A_{act}^T\omega_{fl} + A_{act}J_{fl,sum}A_{act}^T\omega_e\right) - \tau_e\right) + Z \tag{3.8}$$

where $\mathrm{Z} = (\lambda_1 + \lambda_2 \mathrm{G})\dot{q}_{ve} - R_e\dot{\omega}_d + [\omega_e{}^{\times}]R_e\omega_d$, and λ_1, λ_2 are positive design parameters, and

$$G = n \cdot diag({q_{ve}}^{n-1}) \tag{3.9}$$

where, the terminal sliding mode surface, S, is asymptotically stable with $n > \frac{1}{2}$ [52], defined as

$$S = \omega_e + \delta_1 q_{ve} + \delta_2 A_{act}\omega_{imp} + \delta_3 A_{act}\omega_{fl} + \delta_4 q_{ve}^n \tag{3.10}$$

where $S = [S_1\ S_2\ S_3]^T \in \mathbb{R}^{3\times 1}$ and $\delta_1, \delta_2, \delta_3, \delta_4$ are constant positive-definite gain matrices.

Stability Proof

To ensure that the system state remains in sliding mode after convergence, the conditions

$$lim_{s(x)\to 0^+}\, \dot{s}\,(x) < 0 \quad \& \quad lim_{s(x)\to 0^-}\, \dot{s}\,(x) > 0 \tag{3.11}$$

must be satisfied. To ensure the reaching of the sliding manifold is independent of initial conditions, the reaching condition must also be satisfied:

$$s\dot{s} < 0, \forall s \neq 0 \tag{3.12}$$

With respect to the Lyapunov theory, the existence and reaching conditions for the sliding mode can be expressed if there exists a Lyapunov function:

$$V(s) \in R^{+}: \begin{cases} V(s) = 0 & for\ s = 0 \\ V(s) > 0 & for\ s \neq 0 \end{cases} \tag{3.13}$$

Theorem 3.1: For the system model in Eq. (2.31), if the sliding manifold is chosen as Eq. (3.10), the control law is defined as Eq. (3.6), and the actuator electromechanical dynamics are governed by Eq. (2.1) and Eq.(2.3), then the system tracking error Eq. (3.1) and Eq. (3.3) will converge to zero as time approaches infinity.

Assumption: For the system model in Eq. (2.31), it is considered that three actuators are used to provide control torques about the principle axes using the S3 configuration; the A_{act} distribution matrix is thus converted to an identity matrix $I_{3\times3}$.

Proof: To prove that the control law Eq. (3.6) fulfills the sliding mode reaching condition Eq. (3.12), consider the following Lyapunov candidate function

$$V = \frac{1}{2} S^T S \tag{3.14}$$

where the first time-derivative of Eq. (3.14) is expressed as

$$\dot{V} = S^T \dot{S} \tag{3.15}$$

and the first derivative of Eq. (3.10) is governed by

$$\dot{S} = \dot{\omega}_e + \delta_1 \dot{q}_{ve} + \delta_2 \dot{\omega}_{imp} + \delta_3 \dot{\omega}_{fl} + \delta_4 n q_{ve}^{n-1} \dot{q}_{ve} \tag{3.16}$$

Substituting Eq. (3.16) into Eq. (3.15) yields

$$\dot{V} = S^T \left(\dot{\omega}_e + \delta_1 \dot{q}_{ve} + \delta_2 \dot{\omega}_{imp} + \delta_3 \dot{\omega}_{fl} + \delta_4 n q_{ve}^{n-1} \dot{q}_{ve} \right) \tag{3.17}$$

Substituting $\dot{\omega}_{imp}$ Eq. (2.1), τ_m Eq. (2.1) and Eq. (2.2) with $b = 0$, i_a Eq. (2.3), e_b Eq. (2.4), τ_{ff} Eq. (2.20), τ_{fl} Eq. (2.22) and Eq. (2.23) with $\tau_{mf} = 0$, $\dot{\omega}_{fl}$ Eq. (2.30), $\dot{\omega}_{BI}^{B}$ Eq. (2.31), $\dot{\omega}_e$ Eq. (3.4), v_a Eq. (3.6), and τ_c Eq. (3.7) into Eq. (3.17) and simplifying the mathematical expression yields,

$$\dot{V} = S^T\left(\left(J_s + J_{fl,sum}\right)^{-1}\left(-\omega_{BI}^{B\times}\left(J_s\omega_{BI}^B + J_{fl}\omega_{fl} + J_{fl,sum}\omega_{BI}^B\right) + \tau_e\right) + \left(\left(J_s + J_{fl,sum}\right)^{-1} + \delta_2 J_m^{-1} - \delta_3 J_{fl}^{-1}\right) \times \left(-\varkappa_1 S - \varkappa_2 sgn(S) + \left(J_s + A_{act}J_{fl,sum}\right)^{-1}\left(\omega_{BI}^{B\times}\left(J\omega_{BI}^B + A_{act}J_{fl}A_{act}^T\omega_{fl} + A_{act}J_{fl,sum}A_{act}^T\omega_e\right) - \tau_e\right) - \lambda_1\dot{q}_{ve} - \lambda_2 n q_{ve}^{n-1}\dot{q}_{ve} + R_e\dot{\omega}_d - [\omega_e^{\times}]R_e\omega_d - \alpha_f\omega_{fl}\right) - R_e\dot{\omega}_d + [\omega_e^{\times}]R_e\omega_d + \left(\delta_3 J_{fl}^{-1} - \left(J_s + J_{fl,sum}\right)^{-1}\right)\alpha_f\omega_{fl} + \delta_1\dot{q}_{ve} + \delta_4 n q_{ve}^{n-1}\dot{q}_{ve}\right) \tag{3.18}$$

Taking the control parameters as

$$\delta_1 = \lambda_1 \tag{3.19}$$

$$\delta_2 = 2J_m \tag{3.20}$$

$$\delta_3 = \left(\left(J_s + J_{fl,sum}\right)^{-1} + I_{3\times3}\right)J_{fl} \tag{3.21}$$

$$\delta_4 = \lambda_2 \tag{3.22}$$

and simplifying the mathematical expression yields

$$\dot{V} = S^T\left(-\varkappa_1 S - \varkappa_2 sgn(S)\right) = -\varkappa_1 S^2 - \varkappa_2 S \cdot sgn(S) \tag{3.23}$$

Therefore, the first derivative of the Lyapunov function has been proven negative definite, and the control law is almost globally asymptotically stable.

3.3 Simulation Results and Discussion

In this section, we illustrate the effectiveness of the PFLA for performing P2P and ATM of nanosatellite (10 kg) through numerical integration of Eq. (2.31) and Eq. (3.6) using the Runge-Kutta (ODE45) numerical solver. For typical brushless DC motors, the values for the inductance L_a in the armature circuit and the viscous friction constant b are very small and therefore are neglected in the dynamic model Cochin [53].

The practical voltage-driven control law that controls the performance measures of the actuator directly must consider the physical performance constraints of the PFLA itself. Due to the physical limitations of actuators the control torque generated is bounded [54] and in the numerical simulation cases considered herein, the PFLA/PFSA motor has an upper torque saturation limit of τ_{max}.

$$\tau_c = \begin{cases} \tau_{max} & if \quad \tau_c \geq \tau_{max} \\ \tau_c & if \quad -\tau_{max} < \tau_c < \tau_{max} \\ -\tau_{max} & if \quad \tau_c \leq -\tau_{max} \end{cases} \tag{3.24}$$

Further, for practical implementations, the inherent chattering associated with terminal sliding mode is addressed and eliminated using the boundary layer method [55]

$$st(S_c) = \begin{cases} \frac{S_i}{\epsilon}, & if \ |S_i| \leq \epsilon \\ sgn(S_i), & if \ |S_i| > \epsilon \end{cases} \tag{3.25}$$

where $\epsilon > 0$ is a small positive constant.

Several cases are analyzed that test the viability and performance of the PFLA as a practical device for attitude maneuvers. This study evaluates S3, S4, and P4 configurations to determine performance measures of accuracy, slew rate, and power consumption for the PFLA and to determine the optimal configuration for the PFLA system onboard a satellite. Each PFLA is equipped with a TCS-M400S micropump that operates using a brushless DC-motor and communicates over an I^2C bus with the main control board. The control law Eq. (3.6) drives the voltage of the pumps that provide the necessary angular momentum about the roll, pitch, and the yaw body-axes.

Table 3.1: System Model Parameters

Parameters	Values
Orbit	
R_e	6878 km
μ_e	398600 $km^3 \cdot s^{-2}$
Satellite Size	0.3 ×0.3 ×0.3 m^3
Satellite Moment of Inertia	
J_{xx}	0.027 $kg \cdot m^2$
J_{yy}	0.022 $kg \cdot m^2$
J_{zz}	0.016 $kg \cdot m^2$
Pumped Fluid Loop Actuator	
J_{fl}	$7.14e^{-4}$; $6.8\ e^{-4}$; $6.5\ e^{-4}$ $kg \cdot m^2$ (3 PFLA) $7.14e^{-4}$; $6.8\ e^{-4}$; $6.5\ e^{-4}$; $7.1e^{-4}$ $kg \cdot m^2$ (4 PFLA)
Sensor Noise Rate Gyro – ADXRS646-EP [56]	0.015 °/s/√Hz

The mapping matrices that relate the PFLA control torques to the satellite body-frame torques for the S3, S4, and P4 configurations have been provided in Eq. (2.24) to Eq. (2.26).

The constant gains and control parameters are selected as: δ_1, δ_2, δ_3 and δ_4 according to Eq. (3.19), (3.20), (3.21) and (3.22), respectively, $\varkappa_1 = 1 \times 10^{-3}$, $\varkappa_2 = 2 \times 10^{-2}$, $\epsilon = 0.05$, $\lambda_1 = 1 \times 10^{-3}$, $\lambda_2 = 1 \times 10^{-3}$, $n = 7/9$, and $\tau_{max} = 1.92 \times 10^{-2}$.

Several cases are studied in this chapter to assess the performance and feasibility of the PFLA for P2P maneuvers and ATM. The study begins by introducing a model that addresses the torque interface between angular momentum based actuators and the satellite that is not considered in the literature. The study then extends the proposed approach to analyze the PFLA performance for attitude tracking maneuvers on P4. To further address the practicality of the PFLA, the effects of sensor noise are examined for point-to-point maneuvers on S4 and P4, and the optimal power configuration of the PFLA is determined; performance measures such as tracking error, power consumption, and control effort are examined.

3.3.1 Attitude Stabilization

The problem with the existing method of overcoming saturation through control techniques is that the actuator models are typically not considered. The maximum torque capable of being provided by the actuator is set as an upper limit in the control algorithm, and the controller behaves by limiting the applied maximum torque to the predefined saturation value. This control torque saturation from the perspective of the control law is not the same as actuator saturation from the hardware point-of-view.

At this point, it is important to define the terms *control torque saturation* as defined in the literature as the limit where constant maximum control torque is applied to the satellite and *actuator saturation* as defined by the maximum angular momentum capable of being generated from the hardware.

To address the saturation limitations from a hardware perspective, Ha et al. [57] proposed the design of a multi-rim composite flywheel rotor to increase the saturation limit of RW technologies and reduce structural mass while maintaining strength. Their analysis confirmed the viability of such a rotor for increased energy storage of 5kWh in comparison to metal flywheels of the same inertial loading.

To further address the saturation problem using hardware, Kim et al. [58] conducted a design study for a microsatellite using RWs and magnetorquers as control hardware onboard the KITSAT-3; magnetorquers were used for momentum dumping to remove RW saturation. They determined that the algorithm used to develop the control strategies allowed for satisfactory results with the developed hardware.

Existing control algorithms developed in the literature are theoretical and do not consider the relationship between the actuator applied torque and its corresponding reaction torque on the satellite. The control torque saturation is of particular interest in this section as the research conducted pertaining to this matter through theoretical control laws does not directly apply to practical hardware. This problem is addressed in this section by examining the response of a satellite under active stabilization when subject to initial disturbance torques. Furthermore, the study is carried out using the voltage-driven nonlinear control algorithm (VDNCL) presented in Section 3.2 while using a high-fidelity model of the PFLA actuator system. The study is initiated by demonstrating the satellite response using the theoretical approach as presented in the literature. Next, the interface between the control torque input and the satellite reaction torque is addressed in order to close the gap that exists between theory and practice. The proposed control technique is applicable to all forms of angular momentum based actuators including reaction wheels and is not limited to the case of the PFLA as considered herein.

3.3.1.1 Case I: Control Torque Saturation ($\boldsymbol{\tau_{fl} = const}$ for $\boldsymbol{\omega_{fl} = \omega_{fl,sat}}$)

Consider a satellite with three PFLA with their torque axes positioned about the primary roll, pitch, and yaw axes (S3 configuration) of the satellite that is subject to an initial angular velocity of $\omega_{BO_0} = (62, -45, -17)\ °/s$ at an initial angle of $\theta_0 = (11°, -11°, 89°)$. The desired states of the satellite are $\omega_{BO_d} = (0,0,0)\ °/s$ and $\theta_d = (0°, 0°, 0°)\ i.e.\ q_{vd} = (0, 0,0,1)$, and the control torque saturation is bounded by limits [-0.0192 0.0192] Nm.

The attitude response of the satellite when using the theoretical VDNCL in conjunction with the high-fidelity PLFA model is presented in Figure 3.1. Therein it is evident that the actuator stabilizes the satellite from its initial angle of 89° to 0° in ~ 10s about the yaw axis, and is in agreement with requirements of agile maneuvers.

To examine the difference that exists between control torque saturation and actuator saturation, the satellite angular velocity response is examined with respect to the applied control torque as illustrated in Figure 3.2 and Figure 3.3 with particular interest in the periods where control torque saturation occurs. By examining the results for $\tau_{a_1}\left(or\ \tau_{fl_1}\right)$ in Figure 3.3 it is clear that the control torque is saturated on the time range of [0.01s 2.649s]. The fast initial torque ramp-up and fluid angular velocity ramp-up are due to the small moment of inertia of fluid that acts as a light load on the pump rotor, results which are consistent with those found in [59-62]; by increasing the moment of inertia of the fluid as is required for larger satellite, the ramp-up times increase accordingly as seen in [62].

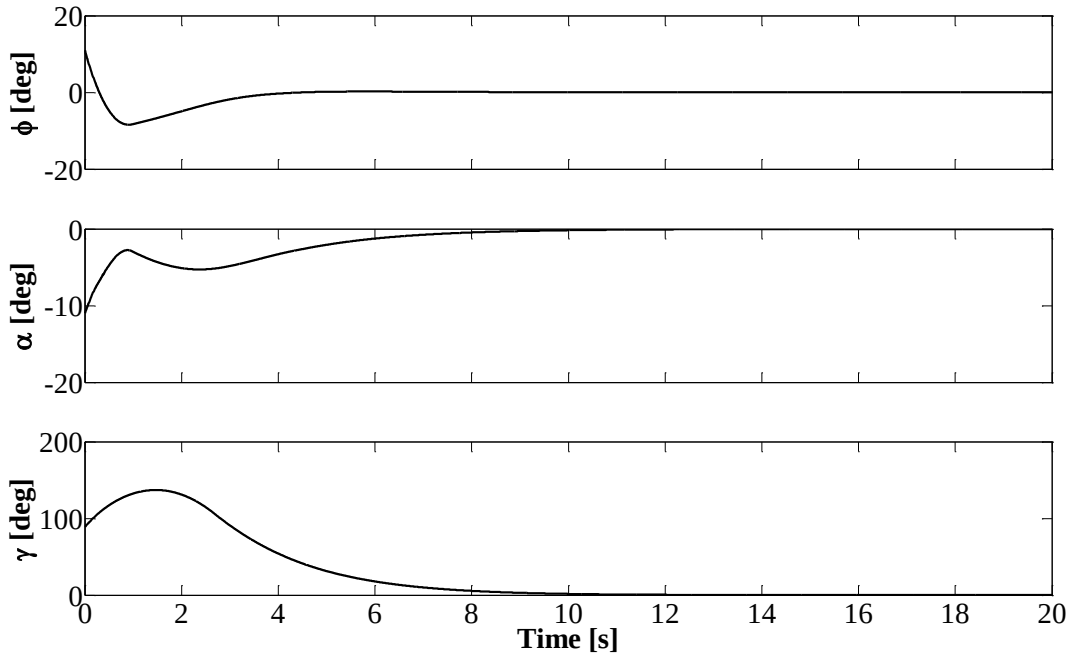

Figure 3.1: Satellite Attitude Response using VDNCL

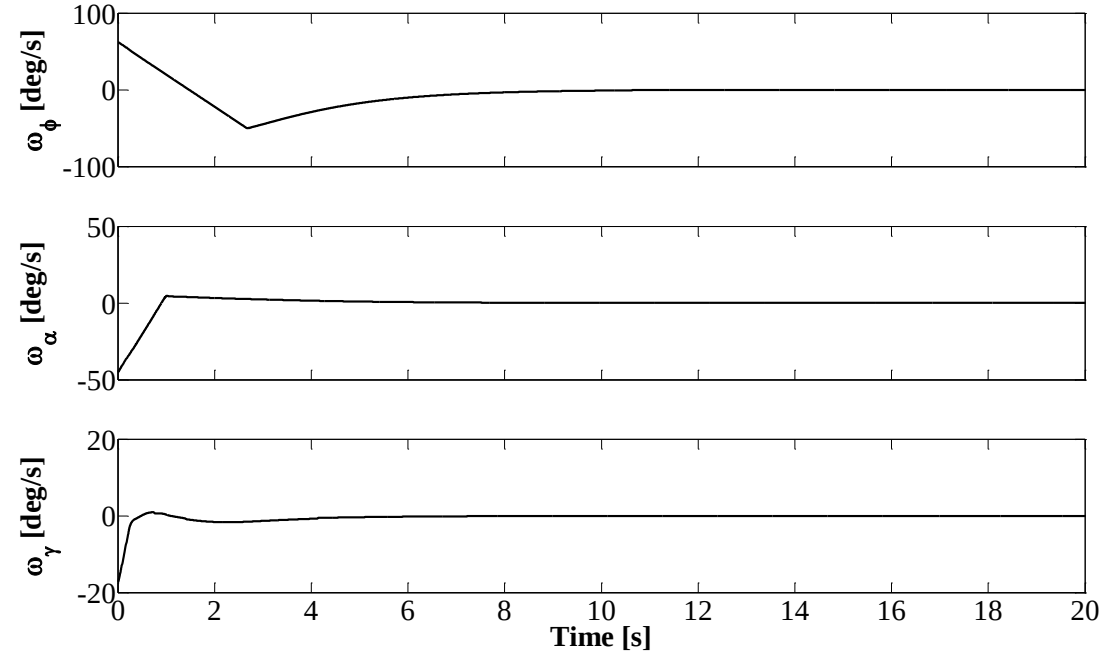

Figure 3.2: Satellite Angular Velocity Response using VDNCL

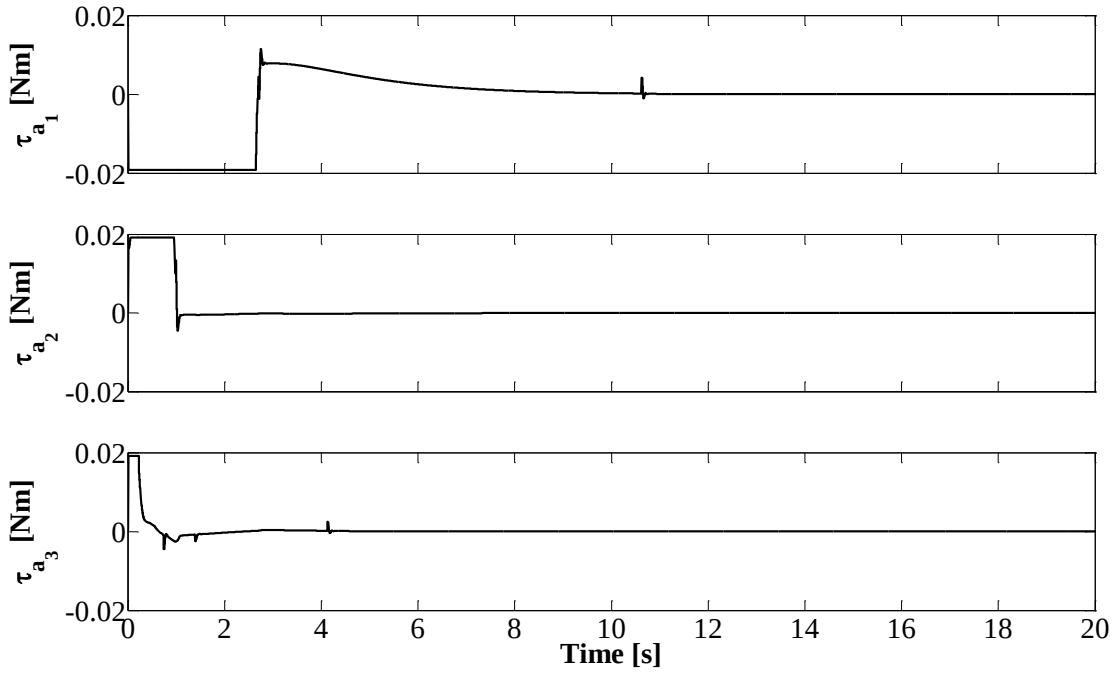

Figure 3.3: Applied Control Torque Profile for VDNCL

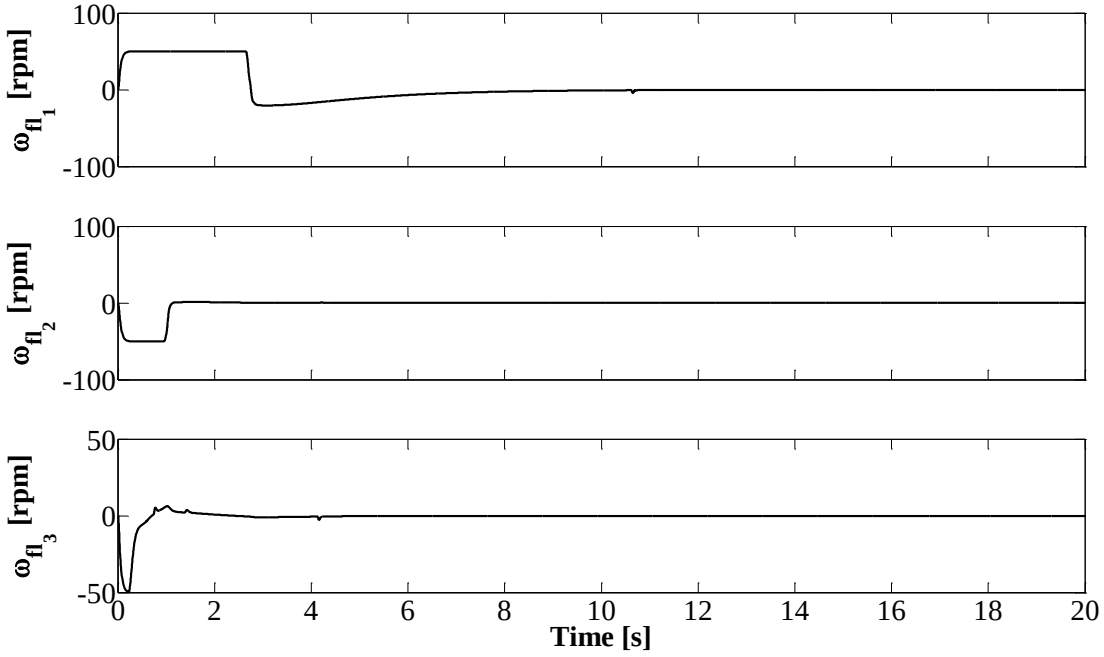

Figure 3.4: Fluid Angular Velocity Saturation for VDNCL

Based on the definition of conservation of angular momentum, it is clear that at the points of saturation of the PFLA, the control torque is constant, thereby implying that acceleration exists. The resultant acceleration of the body during saturation constitutes a linear increase in the angular velocity of the satellite as depicted in the corresponding time range of [0.01s 2.649s] in Figure 3.2. The results presented therein are in direct agreement with results found in the literature [59, 63]. However, the assumption associated with control torque saturation is such that the actuator itself is capable of continuously producing applied torque and transferring its energy to the satellite body thereby suggesting that the actuator itself is able to accelerate continually.

However, by examination of Figure 3.4 (obtained through the numerical integration of Eq. (2.29)) it is seen that during the saturation interval of [0.01s 2.649s], ω_{fl_1} is constant and not accelerating thus indicating that the assumption has an inconsistency with hardware performance. In the case of the PFLA, at fluid saturation, the motor will rotate with a constant angular velocity as seen in Figure 3.4 thereby generating zero acceleration of the fluid (i.e.

constant fluid velocity). Based on the conservation of angular momentum, the resulting applied torque to the satellite is then zero and not constant as is portrayed in Figure 3.3. Therefore, the satellite cannot experience an increase in angular velocity, without external disturbance, if the conservation of momentum is to be held valid; that is to say that the angular velocity of the satellite will become constant during actuator saturation and will not increase or decrease linearly as shown in Figure 3.2. It is evident that actuator saturation differs from control torque saturation; however, in the literature the relationship between the two has not been addressed. To better understand this, consider the same case as above however, instead of a constant torque being applied during actuator saturation; the applied torque is zero as is the case of real systems. This model can be applied to a theoretical control algorithm in order to obtain results that depict the real response of a satellite under actuator saturation.

The sliding plane and the first time-derivative of the Lyapunov function are illustrated in Figure 3.5.

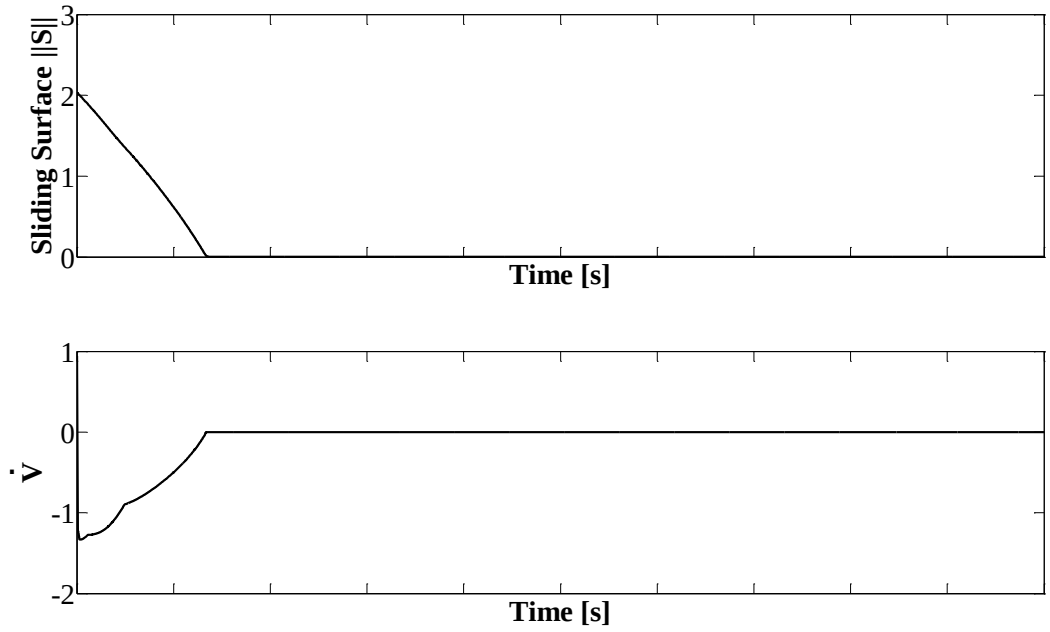

Figure 3.5: Sliding Surface and First-Derivative of Lyapunov Function

3.3.1.2 Case II: Actuator Torque Saturation ($\tau_{fl} = 0$ for $\omega_{fl} = \omega_{fl,sat}$)

For consistency, by once again examining the roll axis results, it is evident that the satellite is stabilized however with an increased settling time of 20 s (Figure 3.6) as opposed to 12s (Figure 3.1) with the VDNCL. By examining the profile of the applied control torque as presented in Figure 3.9, it is clear that the profile does not behave similarly to that of the VDNCL. A closer examination of the fluid velocity on the interval of [6.19s 10.93s] in Figure 3.8 shows that when the angular velocity of the fluid is constant, the applied control torque tends to zero. The absence of fluid acceleration, therefore, suggests that the maximum possible angular momentum exchange is achieved between the fluid and satellite. This statement indicates that zero applied torque does not need to happen at maximum velocities but rather requires the occurrence of constant velocity over time to be defined.

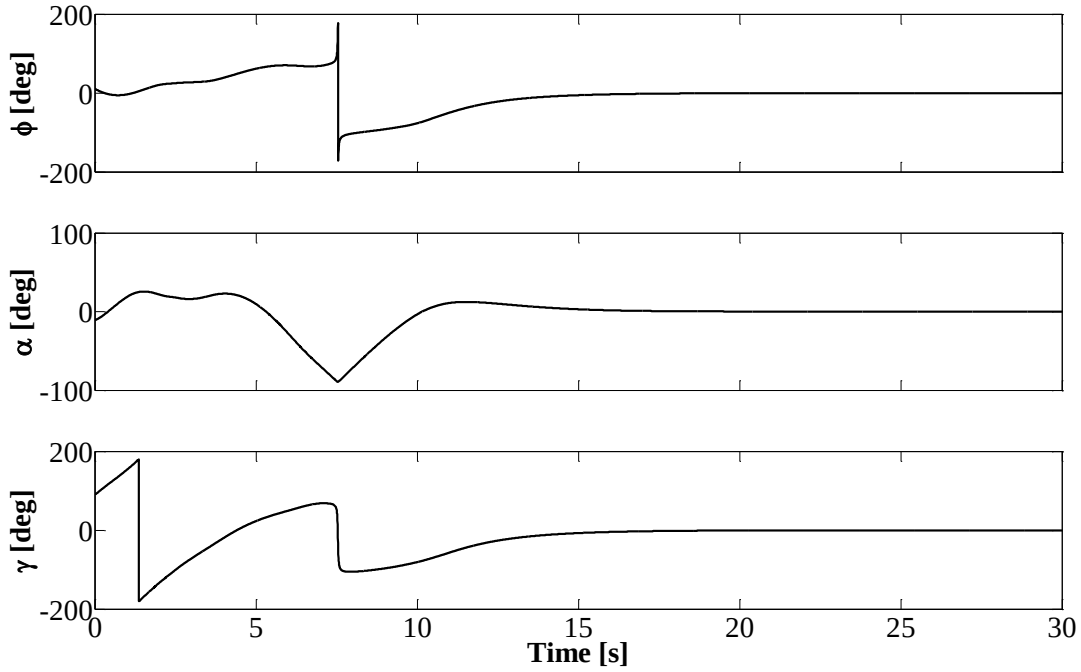

Figure 3.6: Satellite Attitude Response

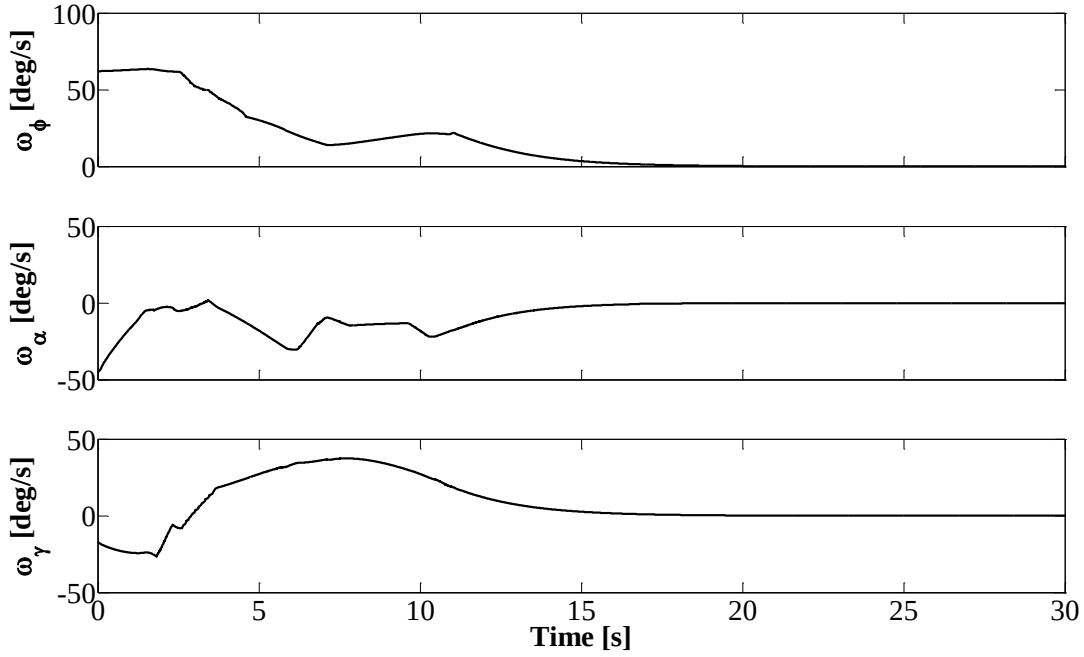

Figure 3.7: Satellite Angular Velocity Response

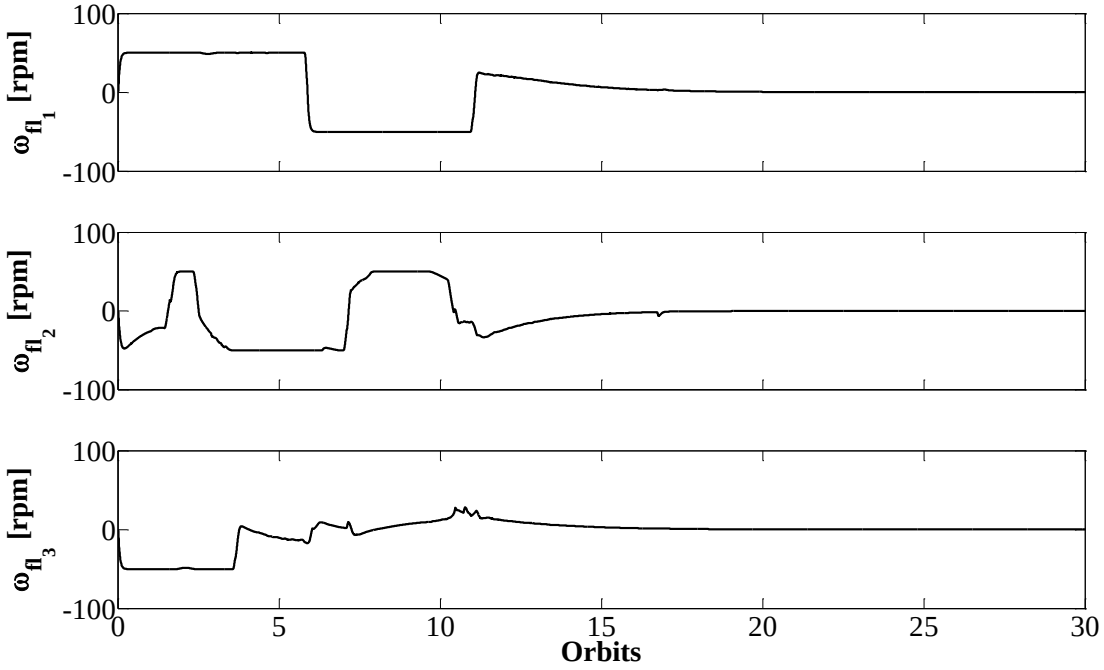

Figure 3.8: Fluid Angular Velocity Saturation

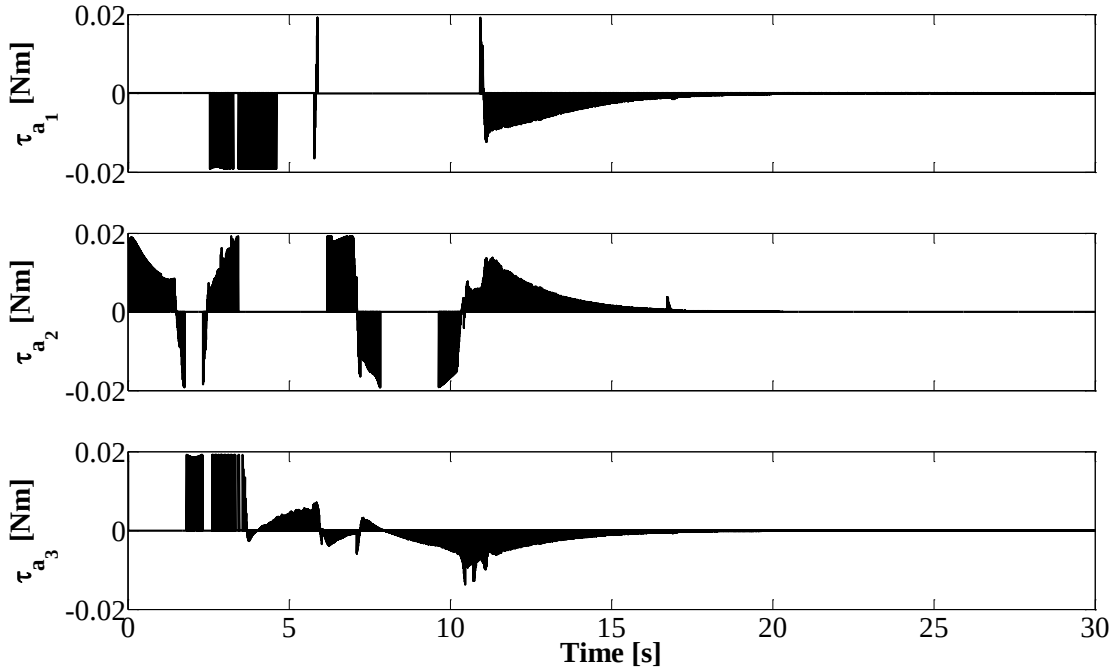

Figure 3.9: Applied Control Torque Profile

The angular velocity of the satellite has a tendency to be controlled by the initial applied torque as depicted in Figure 3.10 at 2.64s. However, as the applied control torque is nulled at saturation at time ~ 2.645s, its absence causes the satellite angular velocity to stay constant. As the control algorithm attempts to regain control, it once again commands an impulsive saturated torque at 2.65s that further controls the satellite state. This phenomenon behaves periodically to stabilize the satellite as can be seen from the density of the control torque profile in Figure 3.9 and in the detailed view on the interval [2.6s 2.7s] in Figure 3.10.

From Figure 3.9 it is clearly evident that the periodic behavior is not limited to upper saturation limits and occurs even at lower limits; since the velocity of the fluid at those instances remains constant, it therefore also produces a zero applied torque to the satellite. The implementation of this model on the VDNCL converts the sliding mode controller into a bang-bang-like controller that accounts for the interface between actuator control torque and the applied reaction torque to the satellite.

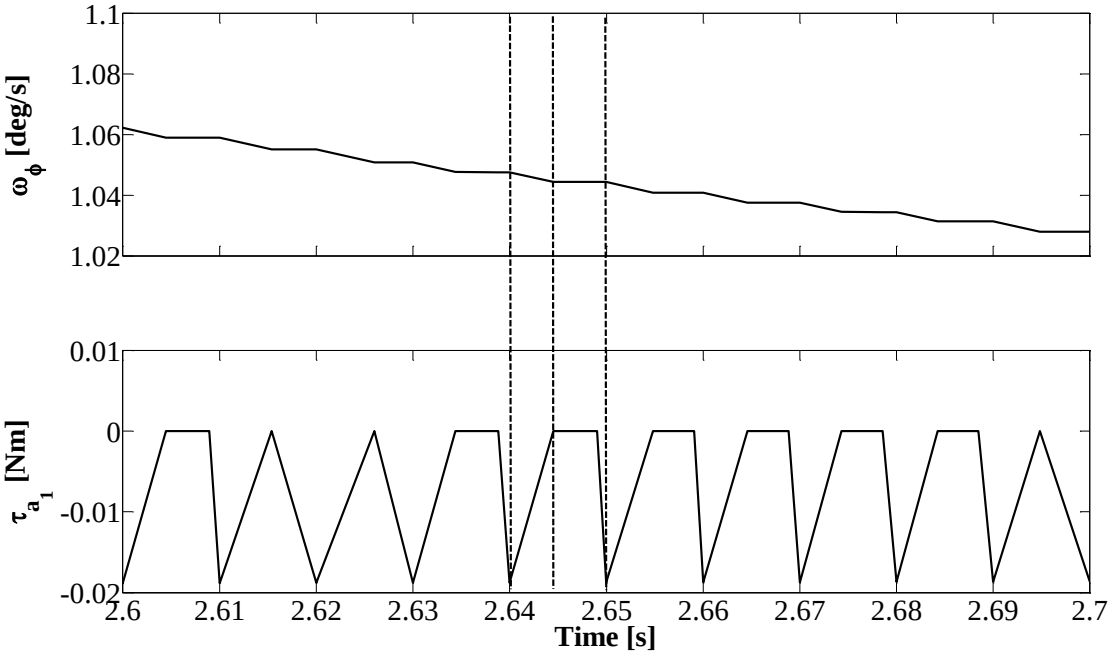

Figure 3.10: Effect of Actuator Saturation on Satellite Velocity for t = [2.6s 2.7s]

This phenomenon is not seen in Figure 3.4 and Figure 3.3 for the VDNCL. In that respect, during control torque saturation, the VDNCL provides a constant torque that continues to control the angular velocity of the satellite under actuator saturation and acts in opposition to the results presented in Figure 3.6 to Figure 3.10. The proposed model indicates that the theoretical control method used in the literature do not account for the behavior of the hardware even though control torque saturation is considered as part of the algorithm.

In this section, an applied torque model was proposed to address the interface between the actuator control torque and the satellite reaction torque. This model introduces a null torque during constant input voltage to the motor, and the results confirmed its representation of real hardware. The application of the proposed model is not limited to the PFLA and can be adopted to provide a practical representation of the hardware performance while using theoretical control algorithm. In this study, the control law presented in Section 3.2 was used and demonstrated the viability of its algorithm for practical applications while driving the voltage of the PFLA motors.

The results further revealed that the response of the satellite and actuator differ significantly from what is proposed in the literature through the solely theory-driven control approaches. The proposed model can be used as a method to verify the practicality of complex nonlinear or linear control algorithms and should be implemented in theoretical control laws in order to obtain a more realistic account of the satellite and actuator behavior.

3.3.2 Attitude Tracking Maneuver

This study takes advantage of the P4 structure for attitude maneuver using the PFLA as this configuration has been verified for minimal power consumption as demonstrated in the subsequent section. The initial angles and body rates are selected for a 3-2-1 rotation sequence as $\theta_0 = (30°,\ -10°, 15°)$ and $\omega_{BO_0} = (20.05,\ -28.65,\ -37.24)\ °/s$. The attitude maneuver that is to be tracked in this simulation is governed by the angular velocity profile in Eq. (3.26) and its norm is depicted in Figure 3.11.

$$\omega_d = \begin{bmatrix} \omega_\alpha \\ \omega_\varphi \\ \omega_\gamma \end{bmatrix} = 0.05 \begin{bmatrix} sin\left(\frac{1.5\pi t}{100}\right) + 0.1 \\ sin\left(\frac{1.2\pi t}{100}\right) + 0.35 \\ sin\left(\frac{2\pi t}{100}\right) + 0.8 \end{bmatrix} \tag{3.26}$$

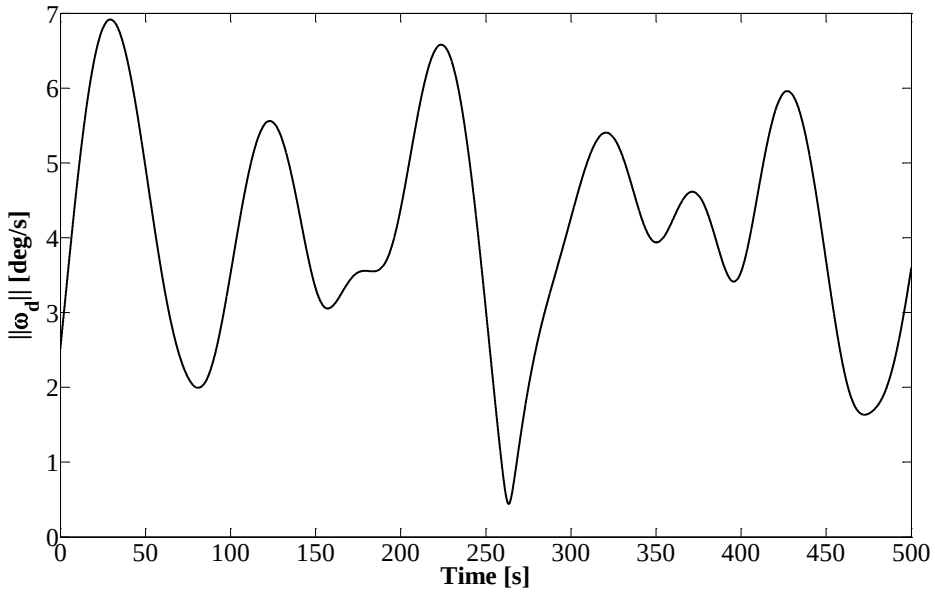

Figure 3.11: Norm of Time-Variant Desired Angular Velocity

The time-variant angular velocities have amplitudes of ~2.87 °/s for all axes and a frequency of oscillation selected as 0.0075 Hz for roll, 0.006 Hz for pitch, and 0.01 Hz for yaw. The objective of this case study is to determine the feasibility of using the PFLA to perform attitude tracking of a time-variant trajectory while subject to uncertain mass moment of inertia defined by

$$J = J_s + \Delta J_s + A_{act} J_{fl} A_{act}^T + A_{act} J_{fl,sum} A_{act}^T \tag{3.27}$$

$$\Delta J_s = 1e^{-3} \cdot \begin{bmatrix} sin(0.1t) & 0 & 0 \\ 0 & sin(0.2t) & 0 \\ 0 & 0 & sin(0.3t) \end{bmatrix} [kg \cdot m^2] \tag{3.28}$$

The uncertain mass moment of inertia is presented in Figure 3.12 is implemented to account for fluid sloshing motions inside the PFLA that are caused during the acceleration and deceleration of the fluid. Since the loops are considered fully filled with liquid, the effects of sloshing are negligible. However, an uncertain mass moment of inertia is considered herein due to potential cavitation that may occur inside the pumps caused by the high angular velocities of the pump impeller.

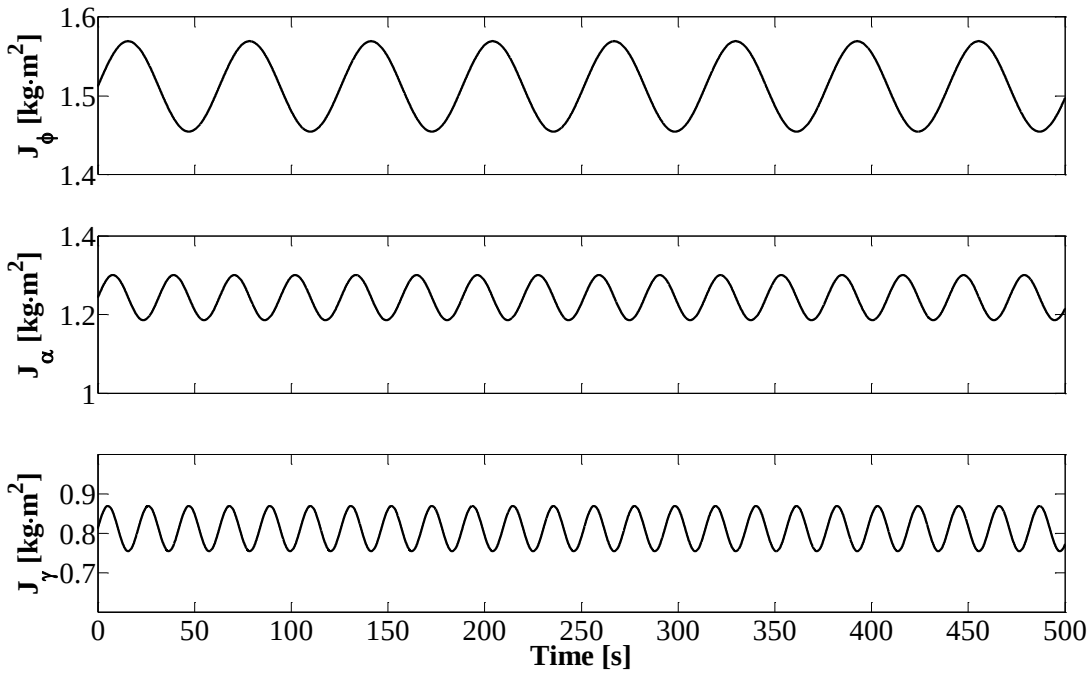

Figure 3.12: Uncertain Mass Moment of Inertia due to Fluid Sloshing

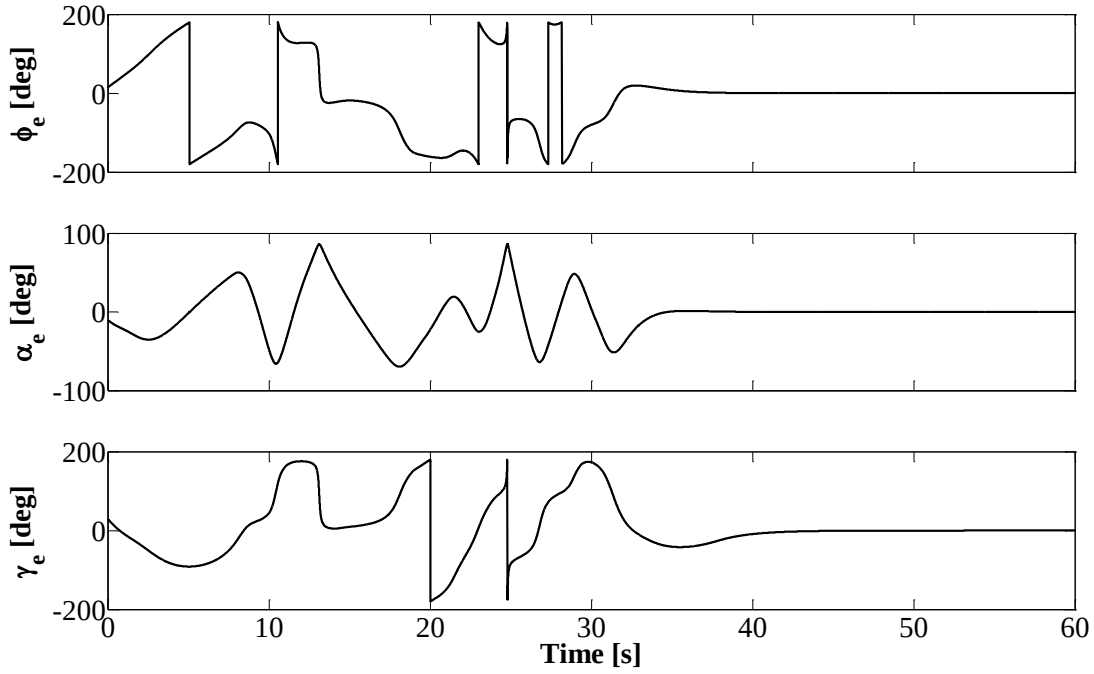

Figure 3.13: Satellite Attitude Error for ATM

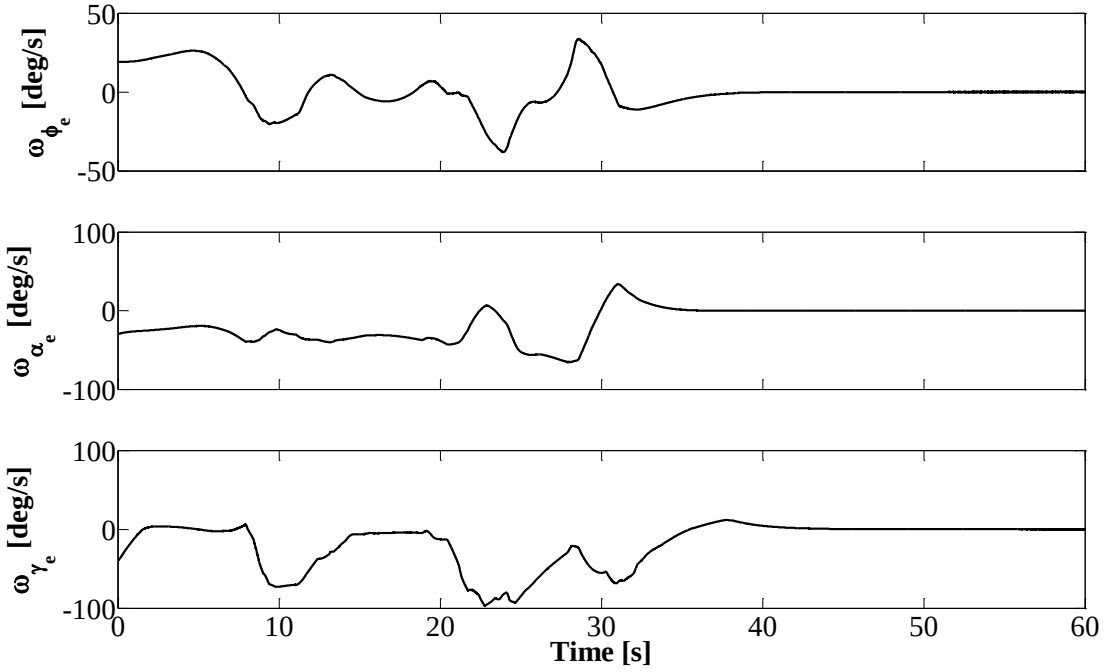

Figure 3.14: Satellite Angular Velocity Error for ATM

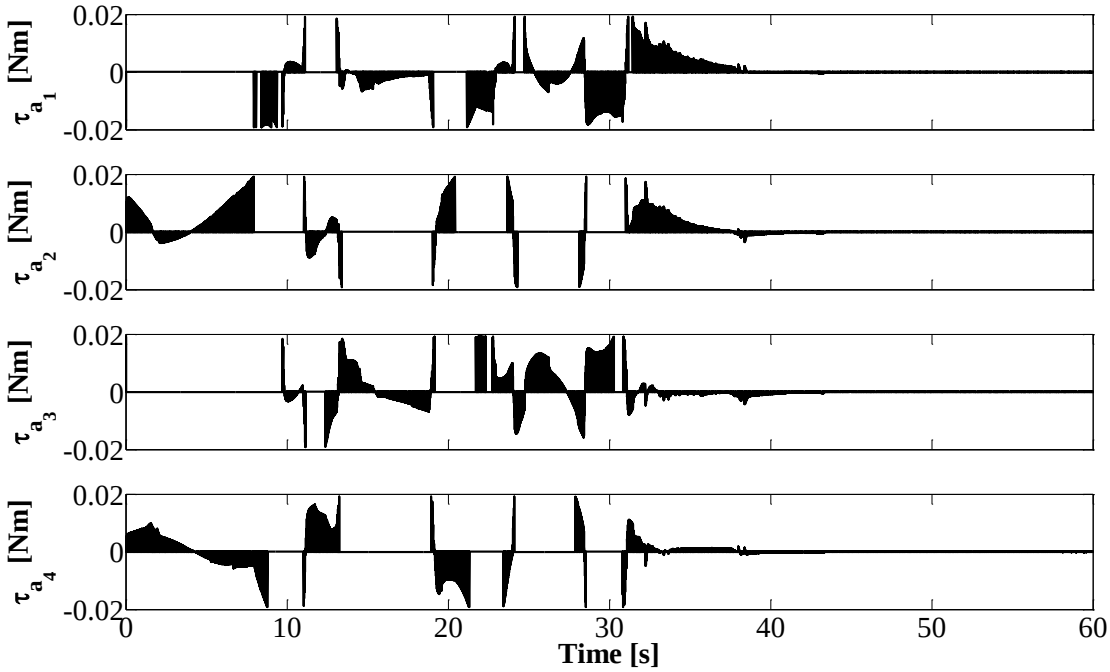

Figure 3.15: PFLA Applied Torque for ATM

The results presented in this section indicate that a satellite equipped with four PFLA in the P4 configuration can provide control torques to track a time-dependent attitude velocity trajectory. The PFLA is able to bring the satellite to its tracking trajectory within 50 s and continue to track the trajectory with a bounded error of [-0.01° 0.01°] as illustrated in Figure 3.13. The observed attitude error of ±0.01° is attributed to the time-dependent desired angular velocity and the sinusoidal uncertain mass moment of inertia due to fluid sloshing.

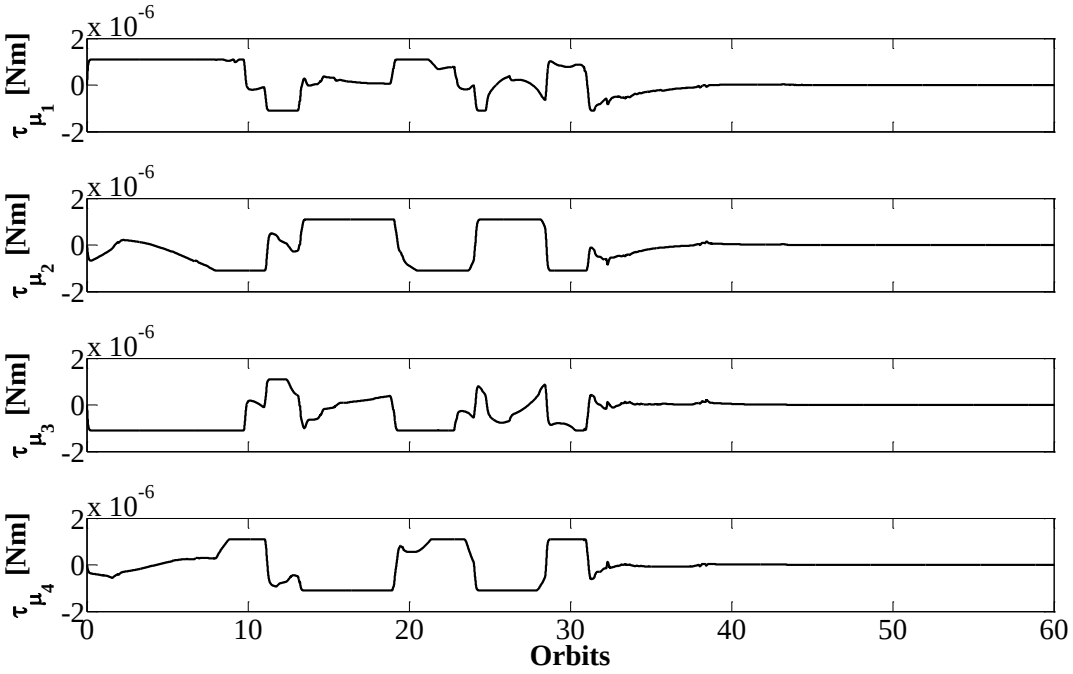

Figure 3.16: Friction Torque due to Fluid Rotation inside the Loops for ATM

The chattering effect has been effectively minimized through the use of the boundary layer method as presented in Eq. (3.25) wherein σ has been selected to eliminate chattering. Although the friction torque is small on the order of 10^{-6} (in the first 45s) and even smaller by two orders of magnitude once the satellite is stabilized, its effects are amplified by the ratio of the motor control constant to the armature resistance. The amplification is portrayed in the applied control torque profile as dense command torques in an attempt of the VDNCL to overcome the friction effects caused by the sloshing motion of the fluid and to mitigate the angular velocity errors.

The practicality of the PFLA system in the P4 configuration is demonstrated for performing time-dependent attitude tracking maneuvers, and the results indicate that a high attitude accuracy of ± 0.01° is possible using the PFLA. Furthermore, the implementation of the practical torque model allowed the PFLA to be examined from the hardware perspective for attitude tracking maneuvers without the necessity of conducting hardware-in-the-loop (HITL) simulations.

3.3.3 Power Consumption

For space missions, one performance measure that must be optimized is the power consumption of subsystems. One method of optimizing power is by reconfiguring the placement of the actuators onboard the satellite. In this section, we address the performance of the PFLA subjected to elevated levels of sensor noise in a trade-off between power consumption and attitude accuracy of the PFLA for performing P2P maneuvers while assessing two actuator configurations, S4 and P4 as described in Section 2.2. The model proposed in Section 3.3.1.2 is used in order to obtain the practical representation of the hardware. Furthermore, a high-fidelity model of the PFLA as presented in Section 2.1 is used to examine the current draw and power consumption of the pumps' motors. The specifications of the PFLA pump are presented in Table 2.1.

This study is examined through a large angle ($\geq \Delta 30°$) P2P maneuver using the PFLA. In this section, the satellite undergoes a maneuver from its initial rest state at $\theta_0 = (31°, -20°, -80°)$ to secondary rest state. The desired attitude angles and angular body-rates are selected $\theta_d = (0°, 50°, -20°)$ and $\omega_{BO_d} = (0,0,0)\ °/s$ and control gains $\delta_1 = 10$ and $\delta_2 = \delta_3 = 1$. Furthermore, the case considers rate sensor noise as an additive fault into the states.

Sensor noise has been examined for the rate gyro sensor provided in Table 3.1, and the results did not conclude the advantage of one actuator configuration over the other since the magnitude of the sensor noise as an additive system fault was quite small at 0.015 °/s. Although the results are not explicitly expressed in this study, the results follow the trend of the nominal profiles in the graphs presented in this section. Therefore, in order to influence the satellite response to determine the optimal actuator configuration under elevated disturbance levels, additional additive error has been introduced into the system to increase the magnitude of the rate gyro error by a factor of ~ 60 thereby resulting in an error of ~ 0.9 °/s at 1 Hz as presented below.

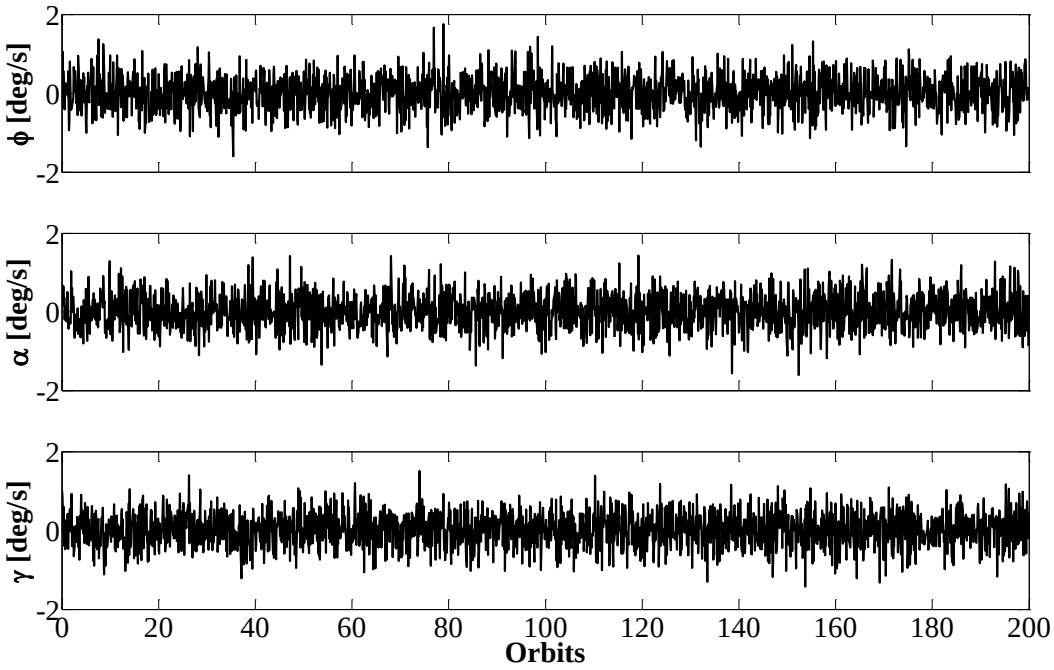

Figure 3.17: Rate Gyro Sensor White Noise

The satellite attitude errors in Figure 3.18 and Figure 3.19 demonstrate that the satellite's response when using the P4 configuration is more readily capable of following the nominal case while subject to high limits of sensor noise as opposed to the S4. The S4 configuration exhibits greater initial deviation from the nominal case. However, its settling time is merely increased by one second from that of the P4 configuration at 138.5s.

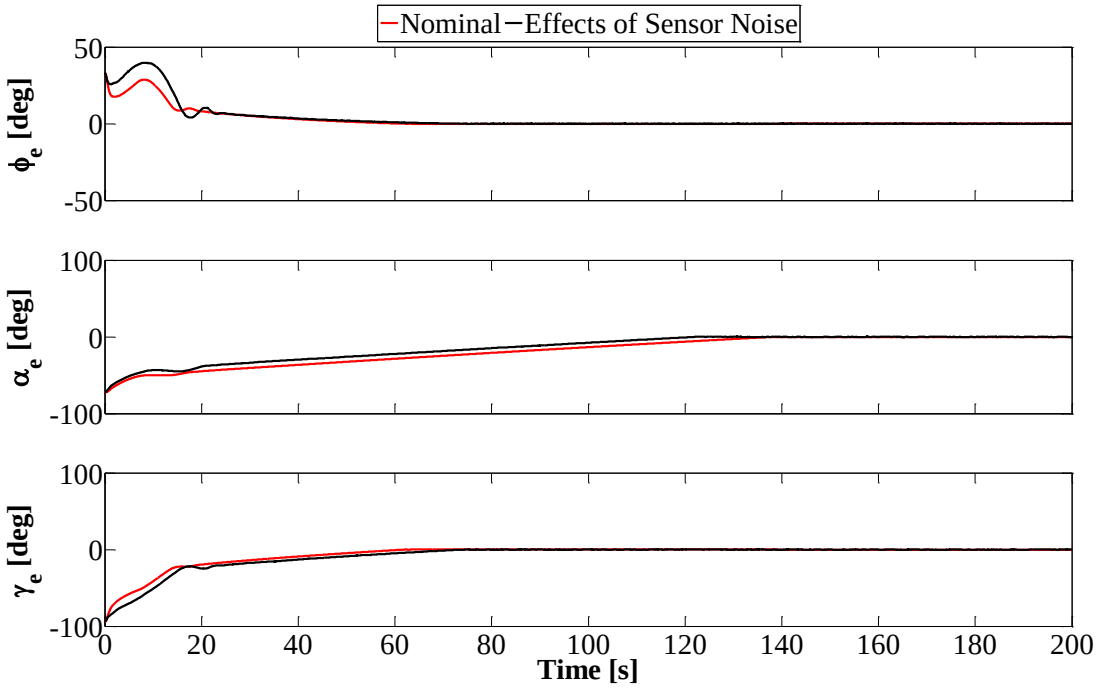

Figure 3.18: Attitude Error using S4 Configuration

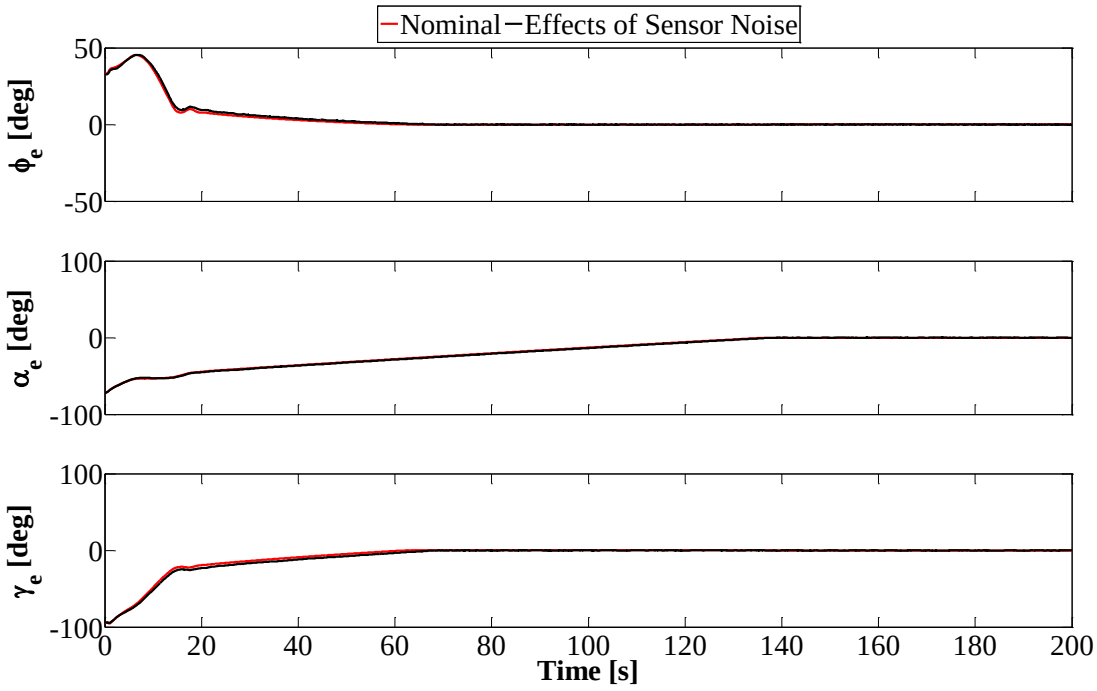

Figure 3.19: Attitude Error using P4 Configuration

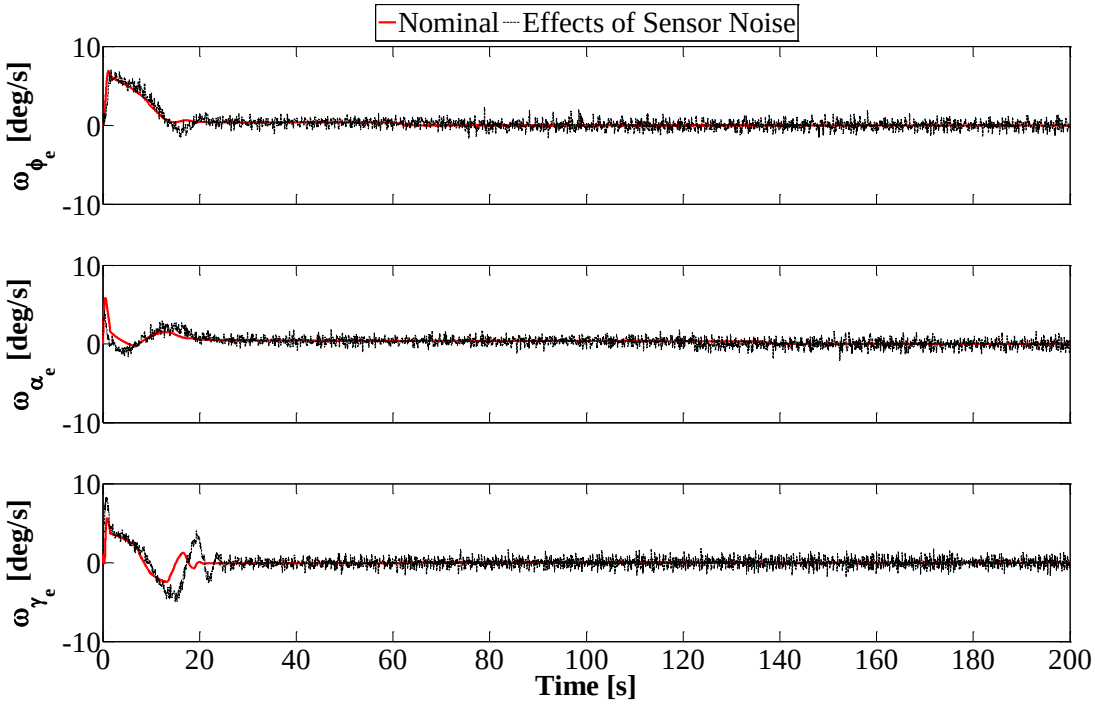

Figure 3.20: Satellite Angular Velocity Error using S4 Configuration

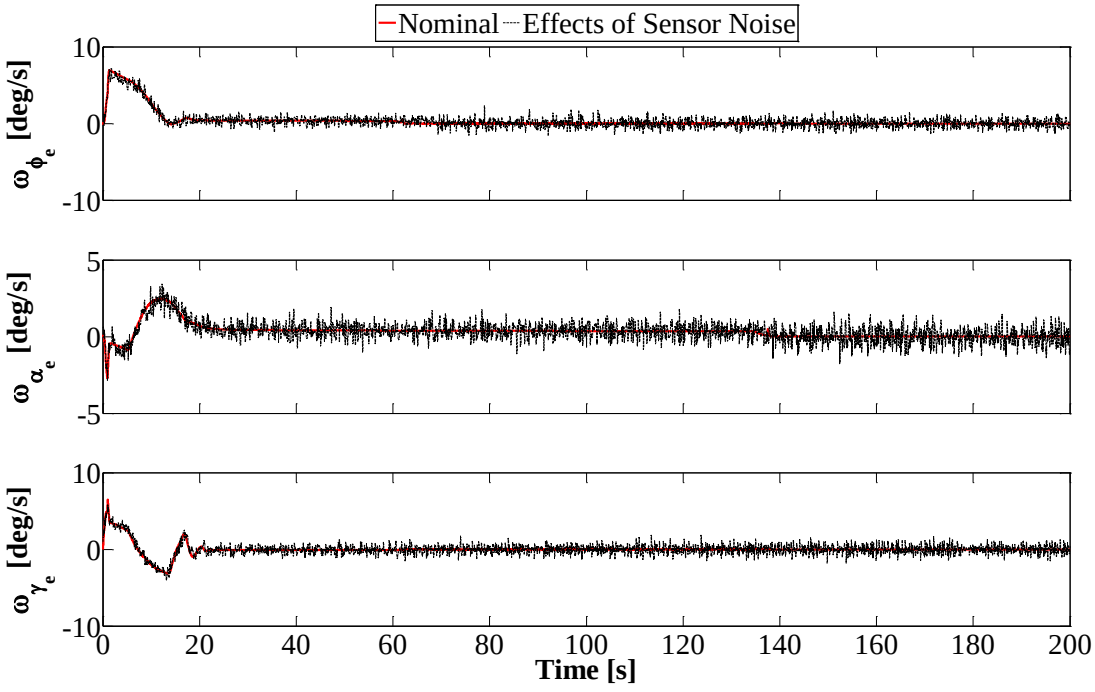

Figure 3.21: Satellite Angular Velocity Error using P4 Configuration

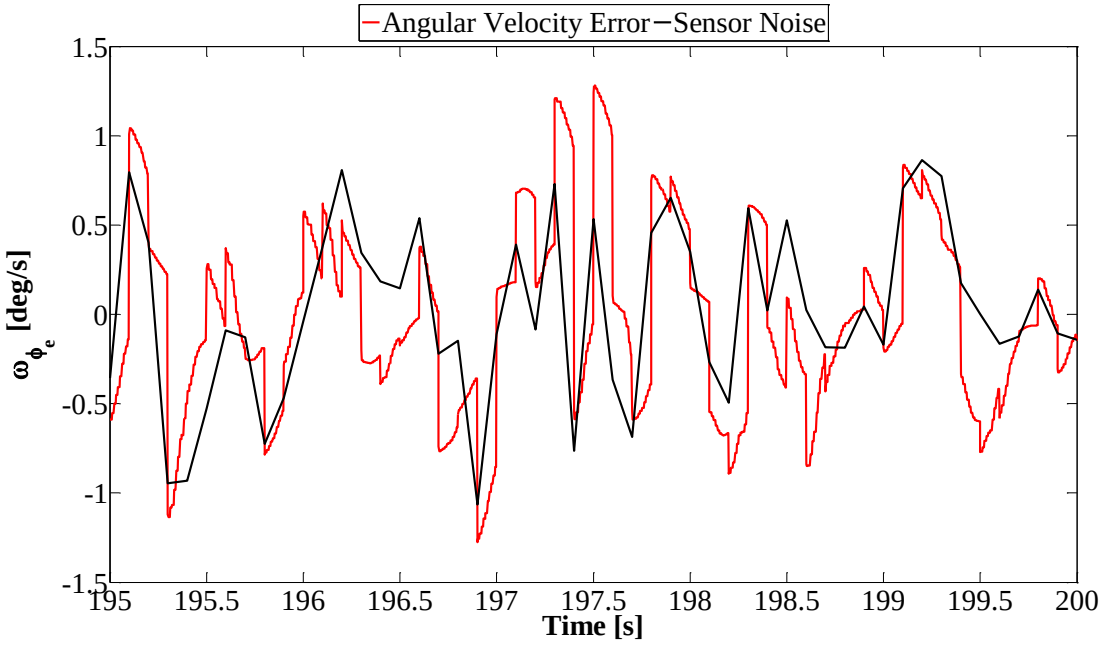

Figure 3.22: Effects of Sensor Noise on Attitude Performance

By examining the angular velocity profiles of the satellite in Figure 3.20 and Figure 3.21 for S4 and P4, respectively, it is evident that the P4 case again follows the trend of the nominal case more effectively that the S4 configuration. Furthermore, a detailed view of the angular velocity error about the roll axis on the interval of [195s 200s] as shown in Figure 3.22 depicts the sensor noise oscillations indicating that when the satellite is stabilized, the control algorithm will need to continue providing control torque in order to maintain the satellite attitude. However, the case considered herein examines an extreme additive fault in the form of elevated sensor noise. The control required for the nominal case will be null once the satellite has been stabilized.

It is interesting to understand why the P4 case is less influenced by the high sensor noise as opposed to the S4 configuration. The notion is a direct result of the manner by which fault is introduced into the system and the positioning of the PFLA; a rate gyro is always positioned with its sensing axes along the primary axes of the satellite. This means that with S4, three of the four axes experience the maximum effects of the additive sensor noise thus resulting in the initial deviations from the nominal. However, with P4, since the PFLA do not line up with the major axes, the effect experienced due to the sensor noise is mitigated, and the PFLA tends to follow

the nominal trend more efficiently thereby requiring less control input. The effects of the S4 and P4 configuration on the power budget must be considered in order to determine the optimal power configuration for P2P maneuvers. Table 3.2 presents the power budget available for various satellite classifications for practical space missions [64].

Table 3.2: Satellite Power Budget

Satellite Class	Power [W] (Body Mounted Cells)	Power [W] (Solar Arrays)
Microsatellite	5.6-46	26-120
Nanosatellite	1.2-10	5.7-26
Picosatellite	0.26-2.1	1.2-5.7
Femtosatellite	0.06-0.47	0.27-1.2
Attosatellite	<0.1	<0.27

In the case of the study herein, typical nanosatellite missions have had a maximum power budget of 26W when using solar arrays and 10W when using body mounted cells. The power consumption from the PFLA is obtained from the DC-motor model in Section 2.1.1; by multiplying the current draw from the pump by the applied motor voltage in Eq. (3.6). The applied motor voltage is presented in Figure 3.23 and Figure 3.24 where it can be seen that for the S4 configuration, motor numbers 3 and 4 required greater than the nominal voltage in the first 20 s that required in the P4 configuration. With reference to the attitude error in Figure 3.18, the necessity for the increased voltage is due to the initial error as caused by the sensor noise. In order for the satellite to be controlled, the control law commands a greater applied voltage that saturates the actuators in order to minimize the standard deviation from the nominal performance. The saturation limits at 12V as seen in the motor voltage graphs generate spikes of increased power consumption as presented in Figure 3.25 and Figure 3.26.

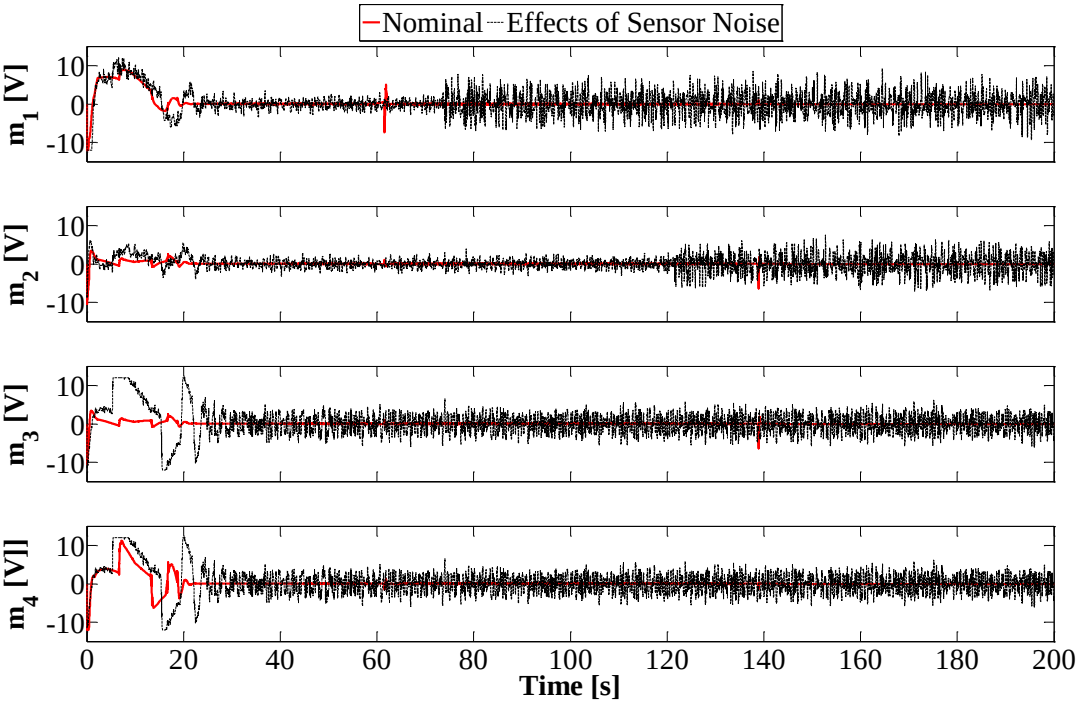

Figure 3.23: Applied Motor Voltage on S4 Configuration

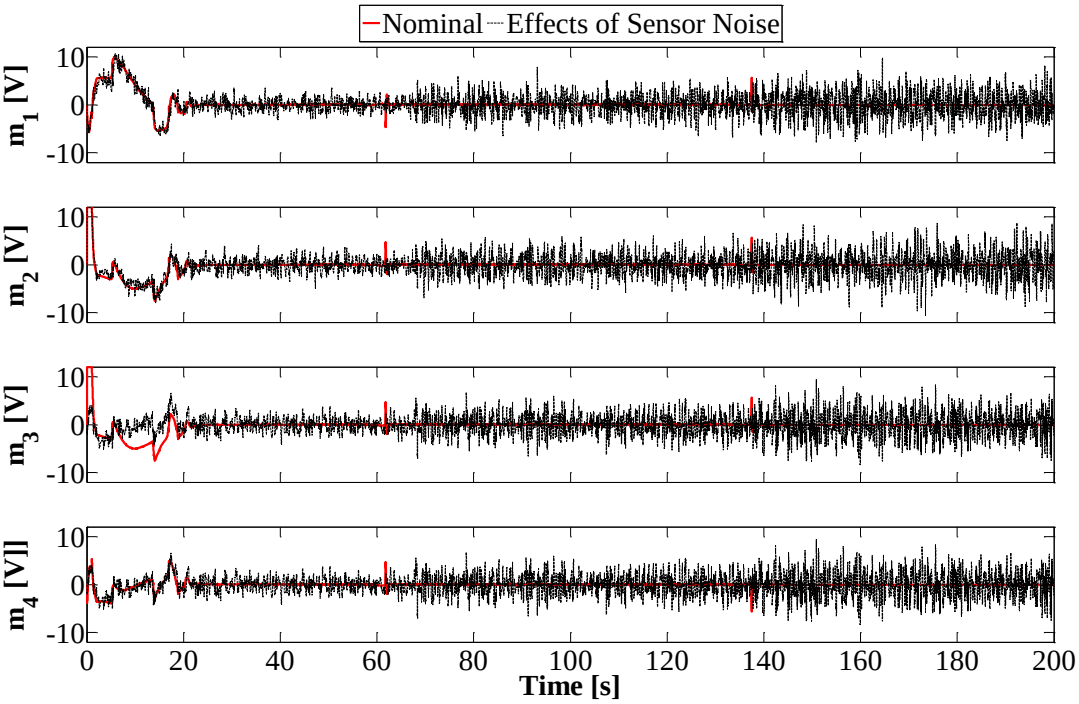

Figure 3.24: Applied Motor Voltage on P4 Configuration

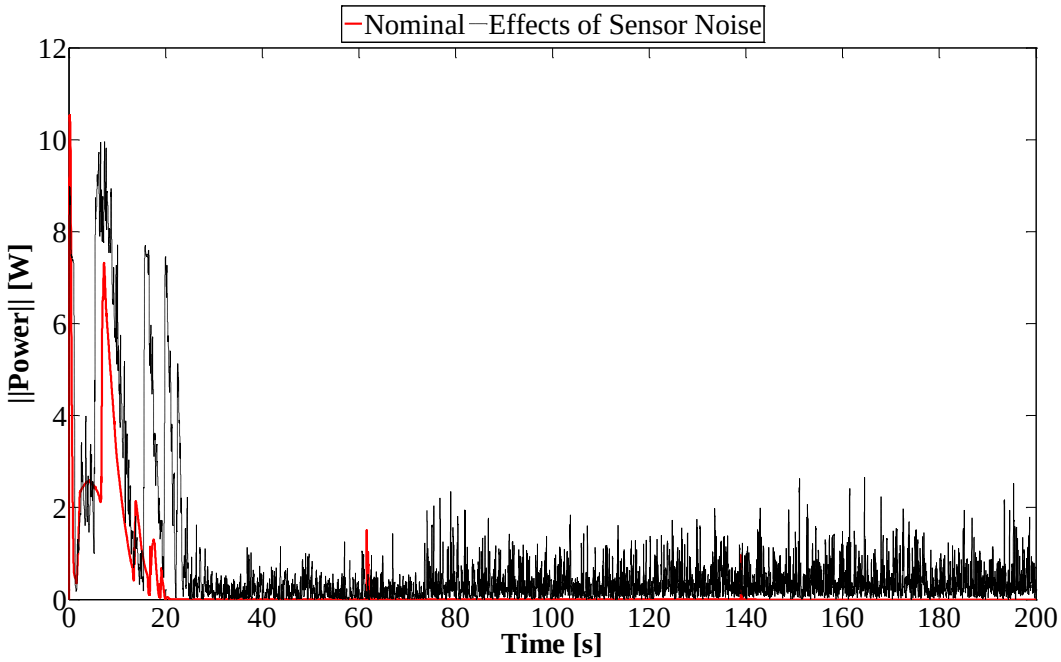

Figure 3.25: Total Power Consumption on S4 Configuration

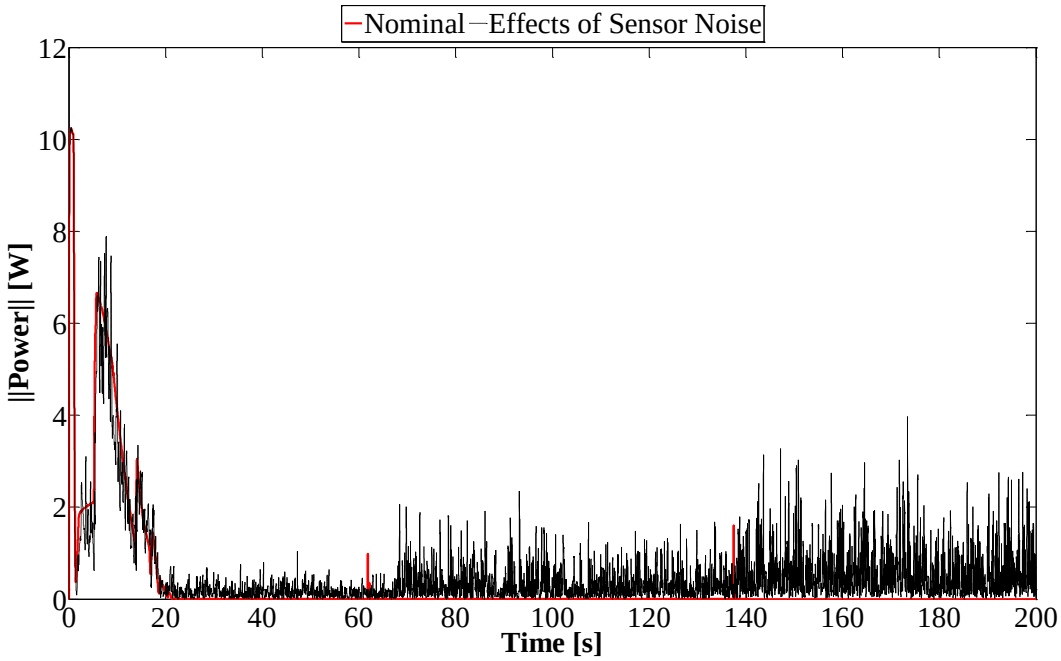

Figure 3.26: Total Power Consumption on P4 Configuration

The saturation limits, although consuming maximum power at 7.1W (per PFLA motor), produce zero effective control torque as was demonstrated in Section 3.3.1 and therefore waste energy. By examining the P4 configuration, the even distribution of applied control voltage as seen in the voltage profile of the four PFLA, do not experience saturation and therefore maximize their control effort without wasted energy.

Further consideration of the power consumption indicates that higher power peaks exist when using S4. Based on the considerations aforementioned and the case under consideration, it is clear that the P4 configuration requires lower peak powers and does not saturate the PFLA thereby maximizing the applied control effort by the actuators. As a result, while the attitude accuracy and settling time of both configurations is comparable, the power consumption of the PFLA under increased additive sensor noise faults exhibits appreciable performance in P4 over the S4 configuration. Furthermore, the normal (noise-free) case of P4 requires lower peak power consumptions than those in the S4 as shown in Figure 3.25 and Figure 3.26.

The increase in control time associated with continuous ATMs as opposed to P2P requires an efficient method that does not waste control torque effort and energy over the duration of the maneuver. As such, for the purpose of demonstrating the attitude tracking capabilities of the PFLA, the optimal power P4 configuration should be used to examine the ATM problem.

It is important to note that during saturation when the satellite angular velocity has exceeded the 7.91º/s upper limit capable of being induced by the PFLA, in order to control the satellite, the control law commands high torque requirements that continuously saturate the PFLA as was demonstrated in this section. Although the coupling effects of the three PFLA tend to stabilize the satellite under these conditions, they consume high power as was seen in Figure 3.25 and Figure 3.26. In section 6.2.3, an alternative approach is proposed that enables a satellite to use less energy when using the PFLA is to still stabilize a satellite without the need for high power requirements during saturation of the PFLA.

3.4 Conclusions

In this chapter a high-fidelity model is introduced to enhance simulation results for attitude control; the model introduces a zero applied torque to the system when constant angular momentum is applied by the actuator. The model was applied to a nonlinear voltage-driven control scheme and examined using the PFLA system for agile attitude maneuvers. The results presented the practicality of the PFLA for active stabilization of a satellite.

The power-optimal configuration of the PFLA was determined by assessing the S4 and P4 configurations and it was determined that configurations of the actuator system can help not only to reduce power consumption but also, the configuration of the satellite plays a robust role from the hardware perspective in the event of additive faults from the rate gyro sensors.

The PFLA was also examined for its feasibility to perform rest-to-rest (P2P) maneuvers and attitude tracking maneuvers of the satellite angular velocity. The results indicated that the PFLA is able to stabilize the attitude of a satellite with an accuracy of ± 0.01° and also bring the satellite to its desired trajectory.

CHAPTER 4
DESIGN AND SIMULATION OF A PUMPED FLUID SPHERICAL ACTUATOR

LIMITATIONS of existing actuators restrict the applications of satellites for space missions. It is evident from the research conducted by [29, 30] that passive attitude stabilization with the PFLA is only possible if the external disturbance torques act on the satellite about the PFLA torque axis. This assumption limits the effectiveness of the PFLA as the cross-sectional diameter must be significantly smaller than the radius of the loop, $D \gg r$. In practical applications the external disturbances will act on the satellite body and generate a resulting torque about some arbitrary axis that is not necessarily the PFLA torque axis. Therefore, in order to alleviate the assumption for the PFLA, stabilization torque must be possible about any arbitrary axis for passive methods.

In order to effectively dampen external torques and provide stabilization about any arbitrary axis without singularities, studies in the literature as presented in Section 1.1.3 express the advantages of spherical design. By using this theory and applying it to the PFLA system, a novel fluid dynamic actuator known as the PFSA is proposed in this chapter. The PFSA takes advantage of spherical design for both active and passive attitude control unlike any actuator to date. By using wall friction effects through the principles of Hagen-Poiseuille flow, the PFSA can effectively passively stabilize a satellite subjected to external disturbance torques about any arbitrary axis. Furthermore, the PFSA is able to create CMG-like angles without the need for additional gimbals.

This chapter is initiated by first introducing the fundamental design of the PFSA in Section 4.1. The governing equations and a simplified Hagen-Poiseuille flow are presented in Section 4.2. to validate the simulations carried out henceforth and to ensure the appropriate extrapolation of results for the PFSA are presented; the optimized design of the PFSA is introduced as determined from CFD analyses and its active and passive capabilities are demonstrated through

simulation in Section 4.3; and, the PFSA is introduced as a simultaneous sensor in the event of rate-gyro failure. Lastly, the conclusions are presented in Section 4.4.

4.1 Design

The structural design of the PFSA is inspired by the studies conducted on the Earth's dynamo effect wherein the angular momentum of the molten outer core generates Earth's magnetic field. The liquid outer core behaves similar to 3-dimensional Hagen-Poiseuille flow, a simplification of which has been studied in Section 4.2. The Earth's crust acts as one wall, and the solid inner core acts as the second. This method is entirely passive and requires no external involvement to operate. By scaling this natural phenomenon and examining its effects through Hagen-Poiseuille flow, a damper is designed wherein fluid has the ability to rotate in the volume generated between two concentric spherical shells, this dynamo-like effect can then be regarded as a method of passive satellite attitude stabilization where the fluid dynamics can be obtained through computer simulation of the Navier-Stokes Equations (NSE).

The PFSA has been designed with three pairs of inlets-outlets; one pair for each major axis of the satellite to which a pump is attached thereby providing three degrees of active attitude control. The flow is regulated from the inlet as it exits the pump, and returns back to the pump after the flow has rotated 315° inside the cavity as is illustrated by the internal section view in Figure 4.1. Furthermore, the inlets and outlets of the PFSA have been designed to be tangent to the internal surface of the cavity. This is to ensure that as the fluid enters and leaves the spherical annulus, it is not disrupting the rotation and/or direction of the flow. The bi-directionality of the pump allows for flow rotation in both clockwise and counter-clockwise directions inside the annular cavity.

The configuration of the pumps is similar to an S3 configuration with one minor difference. Two pumps are positioned in-plane about two primary axes (roll and yaw) and, the other is positioned 90° out of a plane from the third axis (pitch). The reason for this is to maximize the uniformity of the flow throughout the spherical annulus during the interaction of the fluid when pumps are operated simultaneously.

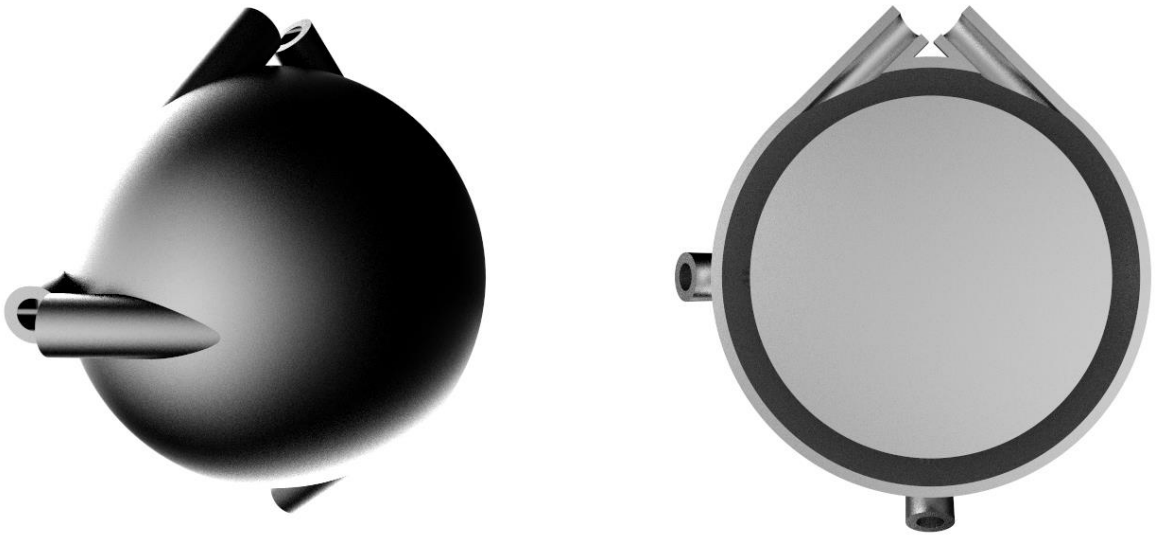

Figure 4.1: Design of the Pumped Fluid Spherical Actuator (PFSA)

The thickness of the annular cavity i.e. (the difference between the radius of the inner face of the outer shell and the outer face of the inner shell) plays a significant role in the torque management of the fluid. With consideration and dependency on the pump performance (output flow rate), with decreasing inner sphere radius, the flow entering the annulus does not attach to the walls but rather falls into the cavity and does not effectively rotate around the circumference of the PFSA to provide control torque about its directed axis.

To initiate the design of the PFSA, a base structural ratio between the inner and outer core was required and selected to match that of the Earth's inner core ratio to its outer and given as ~ 2.86. Next, the design was integrated with SolidWorks Flow Simulation and FEA to obtain the torque and flow characteristics of the PFSA; this formed the basis of this study. The design was then altered by increasing and decreasing the inner core radius to determine the optimal torque-generating ratio. After extensive studies, it was determined that the optimal radius ratio between the outer and inner spherical shell is 1.155 while using the same pump as the PFLA system and an outer shell diameter of 76.2 mm. This optimal ratio provides a balance between active attitude performance and passive attitude stabilization.

For the manufacturing of the PFSA model, the problem associated with modern ACSs that require high precision machining at increased costs has been addressed by its design through additive manufacturing methods. Advanced additive manufacturing has not been extensively explored for the purpose of ACSs of satellite and is introduced here for its simplification of design and capability for manufacturing internal structures, as required in the PFSA model. The PFSA takes advantage of additive manufacturing methods in order to reduce production cost and assembly costs while providing superior attitude control capabilities.

4.2 Computational Fluid Dynamics Model

In order to validate the numerical simulation using SolidWorks Flow Simulation for the PFSA flow field, a laminar flow between two parallel plates is analyzed, and the obtained results are compared against the available theoretical and experimental data in the literature.

A laminar flow between two parallel plates is considered. Flow enters the channel from one end and exits at the other. Since the flow through the channel is symmetric, 2D symmetry can be used to simplify the problem. The boundary conditions are set as a velocity inlet into the channel and a static pressure outlet. To ensure the accuracy of the mesh, the grid-independent solution has to be achieved. This approach involves the fine tuning of a mesh until the results between two different meshes converge within minor and acceptable error. The length of the channel is set to 200 mm with a height of 10 mm, as shown in Figure 4.2. A uniform inlet velocity of 0.01 m/s is considered - the flow is considered to be steady-state, laminar, and fully-developed at the inlet boundary and a pressure outlet is defined and set to 1 atm.

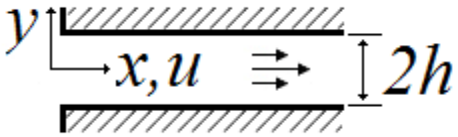

Figure 4.2: Channel Geometry

The flow is determined using the Navier-Stokes momentum equation along the x-direction as governed by:

$$\frac{dP}{dx} = \frac{d\tau}{dy} = const = \frac{\tau_{wall}}{h} \tag{4.1}$$

where $\frac{dP}{dx}$ is the longitudinal pressure gradient along the channel, $\frac{d\tau}{dy}$ is the flow shear stress across the channel opening, τ_{wall} is the shear stress acting on the wall, and h is the height of the channel. The fully developed flow profile for the Newtonian fluid (water) considered herein is presented as

$$u(y) = -\frac{1}{2\eta}\frac{dP}{dx}\left(\frac{h^2}{4} - y^2\right) \tag{4.2}$$

where η is the fluid dynamic viscosity. The pressure gradient along the channel can be obtained using

$$\frac{dP}{dx} = -\frac{3\eta u_{avg}}{h^2} \tag{4.3}$$

where u_{avg} is the average flow velocity defined by the volumetric flow rate divided by the channel cross-sectional area. To assess the governing computational fluid dynamic (CFD) problem, the channel model was designed in SolidWorks and presented in Figure 4.3. The obtained numerical results are compared against the available theoretical data provided in [65] at two locations: 1) a horizontal line along the channel located at h/2, and 2) a vertical line located at 20 mm before the outlet pressure boundary.

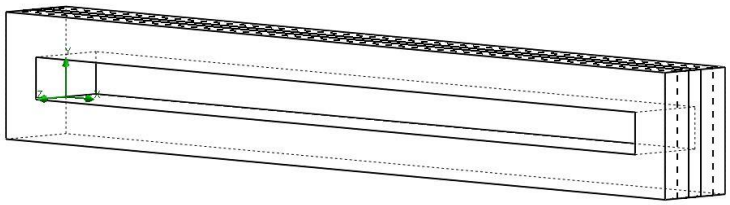

Figure 4.3: Channel Model Designed in CAD for CFD

Simulation results have been presented in Figure 4.4. The resulting velocity profiles at the channel outlet have been validated against theoretical results as presented in [65]

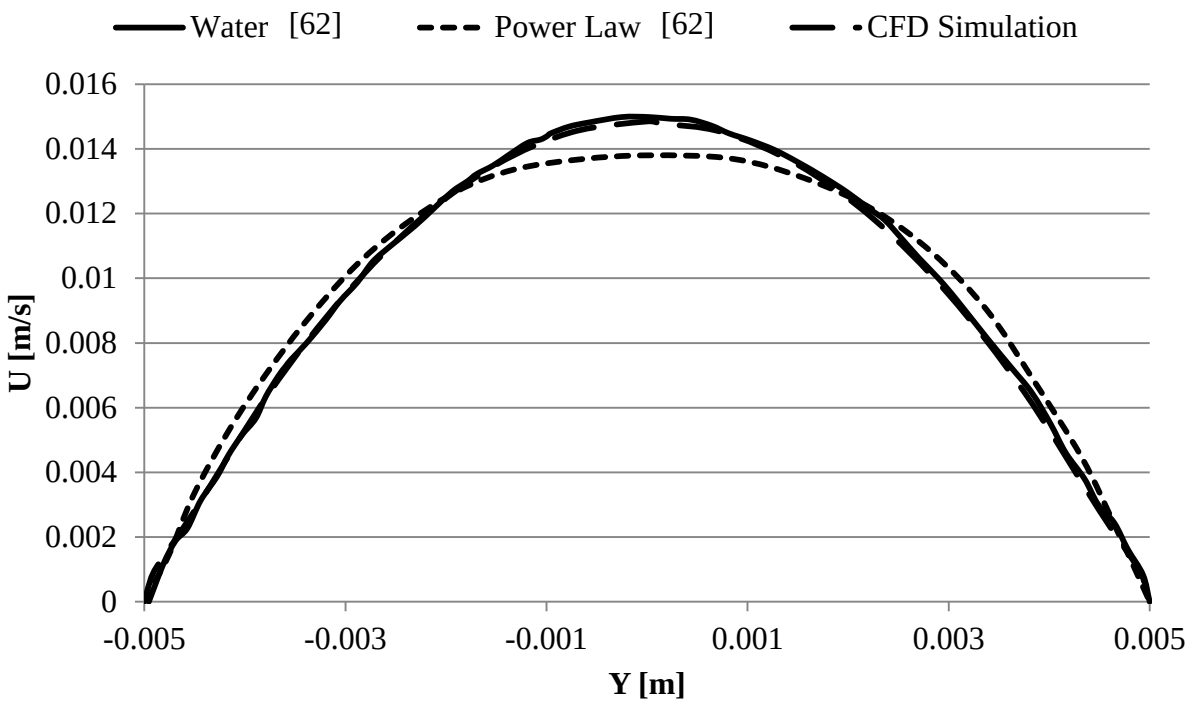

Figure 4.4: CFD Couette-Flow Simulation Validation

It is evident from the simulation carried out in this section that the results of this study match closely to the theory found in the literature as presented in [65]. The analysis of 2D laminar flow between two parallel plates provides validation and merit to the CFD simulation carried out henceforth in this study. The simulated case suggests an accuracy of ~1.2% to the results obtained in the literature. The validated CFD results obtained in this section along with the selected boundary conditions and flow field assessments will be extended to the PFSA as an approximation for Hagen-Poiseuille flow between two concentric spheres to produce the equation that defines the performance of the novel actuator.

4.3 Computational Fluid Dynamics Simulation Results and Discussion

In this section, the performance of the PFSA is studied through CFD; and numerical simulations are carried out in order to determine its feasibility for active satellite attitude control and passive stabilization.

4.3.1 Active PFSA

In this section, the fluid dynamics results of the optimal PFSA configuration using the TCS-M400S pump are presented as obtained from SolidWorks Flow Simulation. The inlet volumetric flow rate is set based on the 12V input of the pump Table 2.1 and the material of the PFSA for CFD simulation and building of the beta-prototype was selected as ABS plastic for its manufacturing process through additive manufacturing.

The axis of rotation (AOR) of the fluid inside the cavity is dependent on the input voltage ratio of the pumps. With the operation of single pumps at any given instance, single axis control torques are made available to the satellite body. However, the advantage of the PFSA exists in its ability to operate like a VSCMG by simultaneously operating multiple pumps at variable voltages. The variance in voltage generates variable torques and changes the inclination angle of the AOR of the fluid. The combination of multiple pumps at steady-state creates a single fluid AOR that drives the attitude of the satellite about the specified axis. Several CFD cases are presented herein to illustrate the active performance of the PFSA.

To ensure the validity of the CFD simulated results, the grid-independent solution was obtained using 359,633 total hexahedral mesh cells using the grid-independent solution for Medium-Fine mesh (Figure 4.5); the grid is presented in Figure 4.7. Figure 4.5 illustrates the grid-independence for the PFSA CFD simulations wherein four mesh variations were considered to capture the flow regime: Coarse (4,810 cells), Medium (103,374cells), Medium-Fine (359,633 cells), and Fine (1,315,200 cells). It is evident from Figure 4.5 that the Medium-Fine mesh is indirect agreement with the Fine mesh while using a much lesser number of cells and therefore reducing the computational cost.

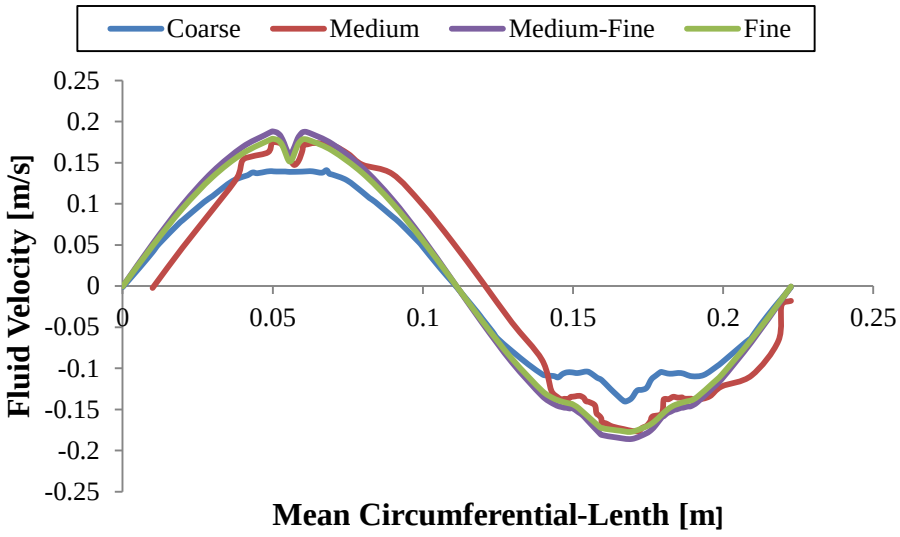

Figure 4.5: Grid-Independent Solution

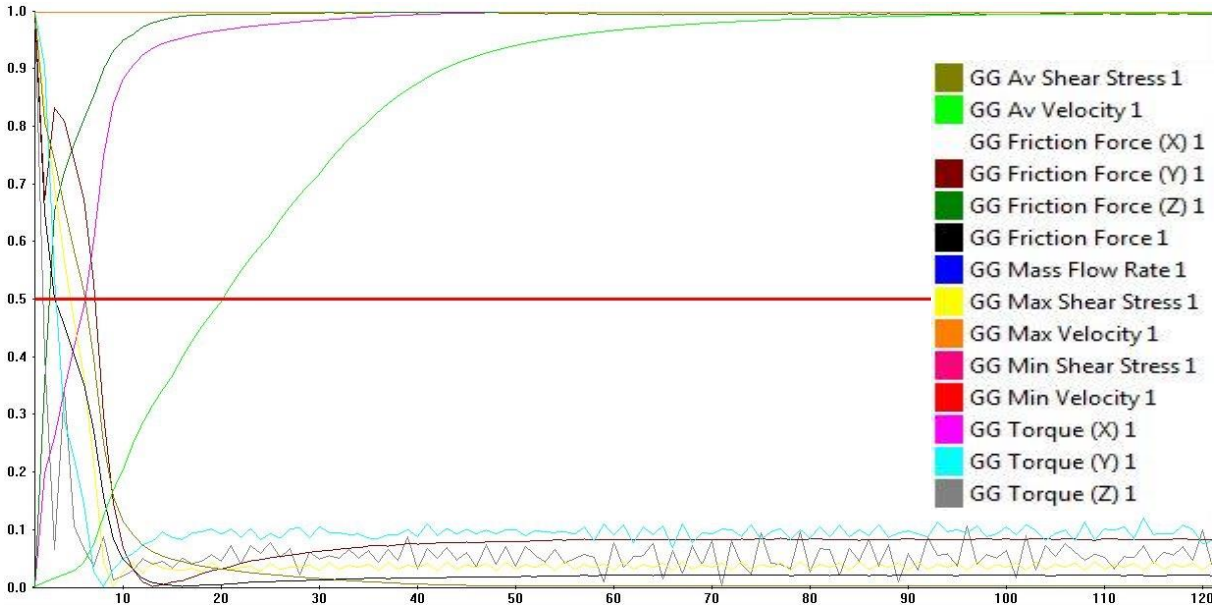

Figure 4.6: Normalized Parameter Convergence Goals

The validation of the CFD results is complimented by the convergence of the desired goals as illustrated in Figure 4.6 in order to correctly assess the flow regime inside the PFSA.

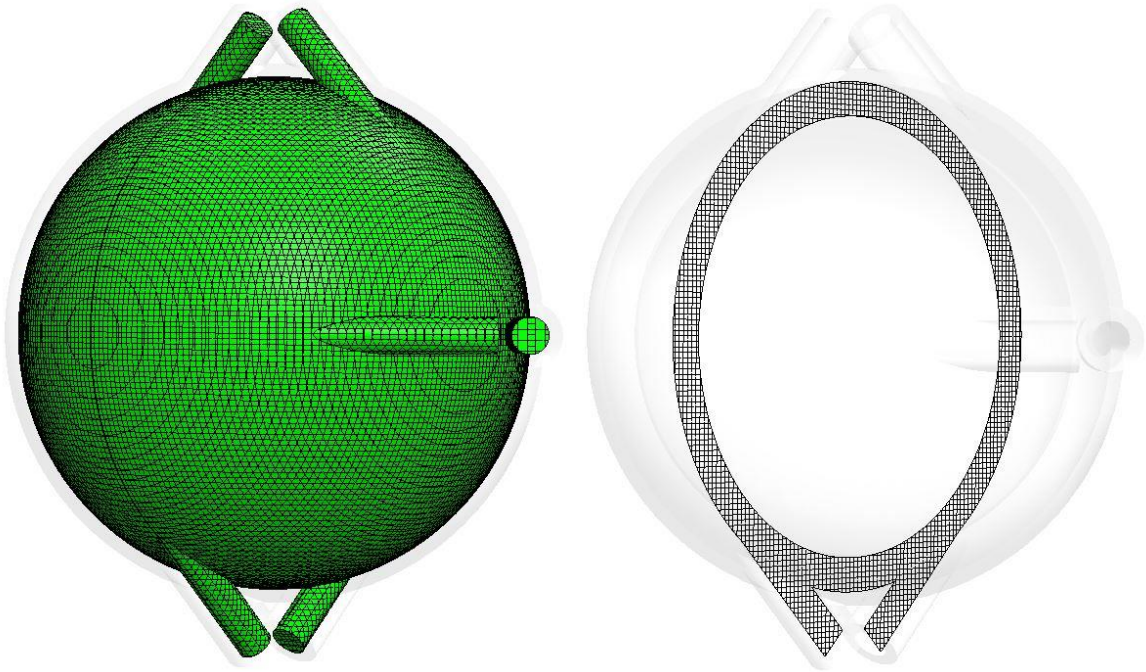

Figure 4.7: Grid Independent Fluid-Mesh for PFSA CFD

Upon obtaining the CFD flow simulation results of the PFSA, the model was imported into SolidWorks FEA to obtain the torque output of the proposed actuator. Three mounting legs were designed and used as fixed joint constraints in order to obtain the resultant torque output of the PFSA system on to a fixed body. The legs were positioned 120° apart at 45° in-plane inclination angles as depicted in Figure 4.8.

Figure 4.8: Finite Element Analysis of PFSA Structure (Fixed-Constraint)

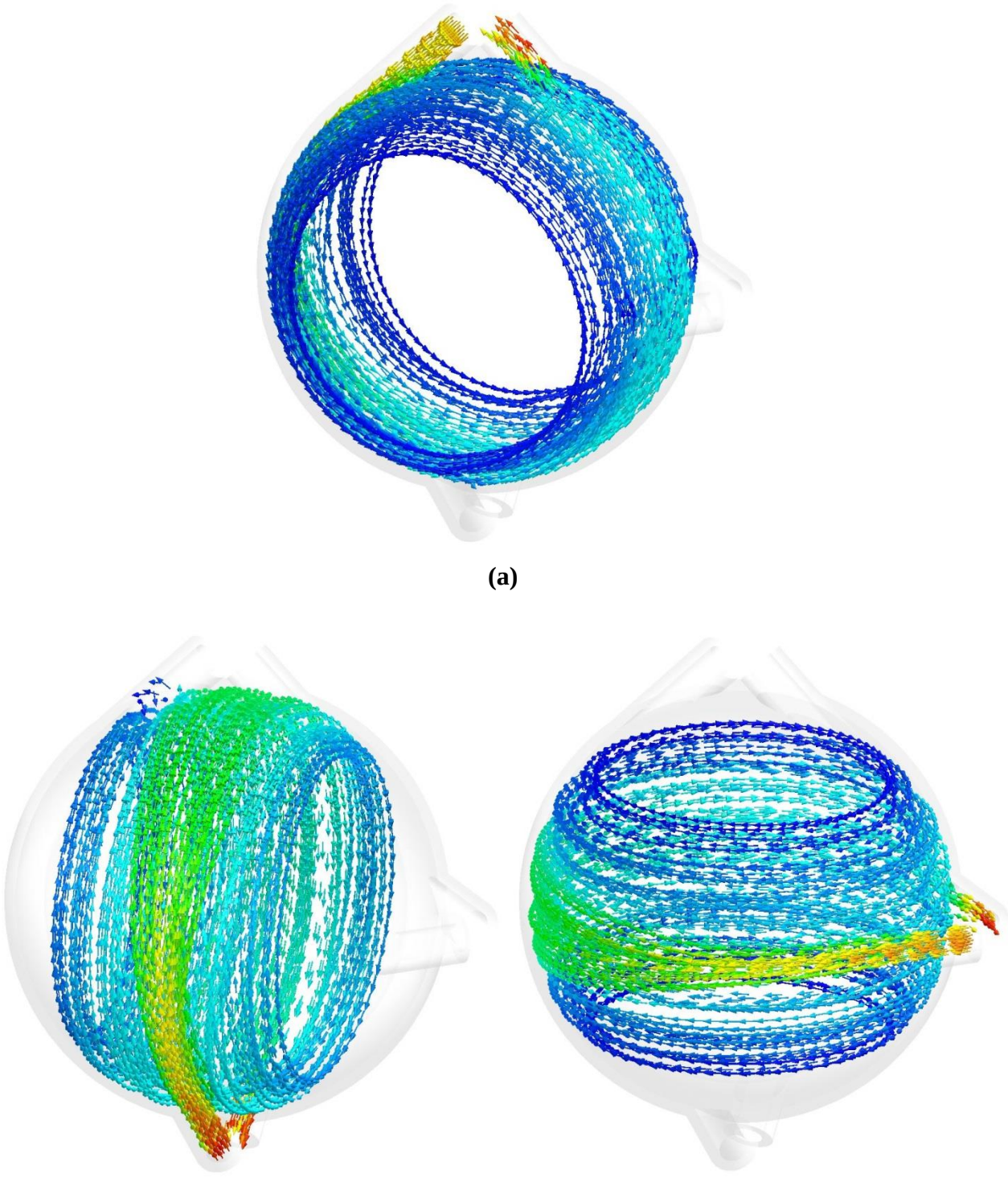

(a)

(b) **(c)**

Figure 4.9: PFSA – Fluid AOR; (a) Roll, (b) Pitch, and (c) Yaw

The results presented in Figure 4.9 illustrate only a single rotational direction about the roll, pitch, and yaw fluid motion inside the annular cavity of the PFSA; the reversal of the pump produces identical results as depicted therein however in the opposing direction. It can be seen that the fluid flow is concentrated about the mid-plane of the respective rotation axis. As the flow enters the annulus, it begins to diverge out from the mid-plane. This fanning effect transfers momentum to the entire region of flow inside the annulus and is equivalent to "stacking" multiple PFLA with decreasing loop radii against one another. From the FEA model, the maximum torque generated by the PFSA about a single axis was obtained to be ~ 0.0175 Nm and is comparable to the maximum torque generated by the PFLA which is 0.0192 Nm.

As aforementioned, the cavity thickness has been designed and optimized to eliminate fluid vortices and back pressures to occur when the flow enters and exits the annulus. It is evident from the results that the flow about the AOR is laminar and symmetrical about the mid-plane. The radii ratio of 1.155 ± 0.25 for this geometry ensures that the flow remains attached and aids in keeping the flow uniform inside the spherical annulus.

The performances of the single-axis results of the PFSA are reflective of each induvial PFLA positioned about the primary body axes of the satellite. However, instead of requiring three individual systems, the PFSA compounds all three PFLA into a single and smaller device while maintaining the torque performance of the PFLA. The reduction in the size of the PFSA presented herein compared to the PFLA is accounted for by the additional volume of fluid that is encompassed inside the spherical annulus of the PFSA that inflicts and increased angular momentum per axis, thereby making up for its smaller size.

Since the pumps of the PFSA operate using the same fluid reservoir inside the PFSA, they can be combined to produce CMG-like angles by varying the voltage ratio to two pumps simultaneously to generate a resultant AOR. The illustrations presented in Figure 4.10 demonstrate this phenomenon and are generated inside the PFSA by using a 12V input voltage from the pump at voltage ratios of 1:1 for pairs of pumps. In Figure 4.10a, a distinct 45° AOR is illustrated as the resultant of simultaneously operating the pitch and yaw axis pumps. Similar effects are presented in (b) and (c) wherein the 1:1 voltage ratio combination is shown to produce a new AOR of the fluid.

(a)

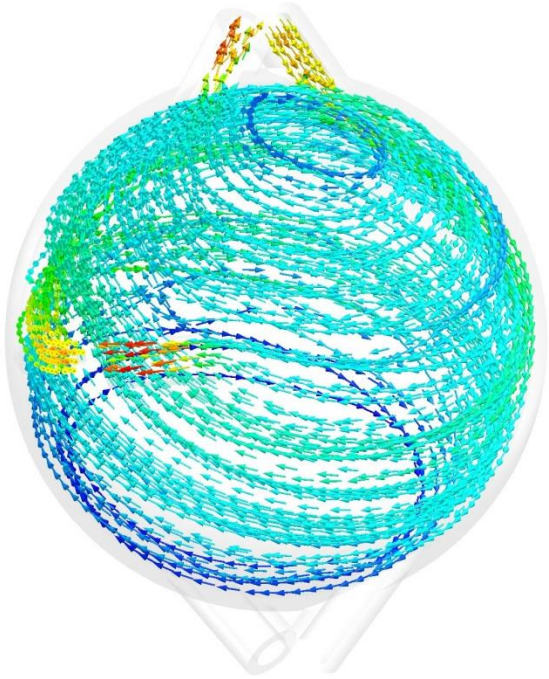

(b)

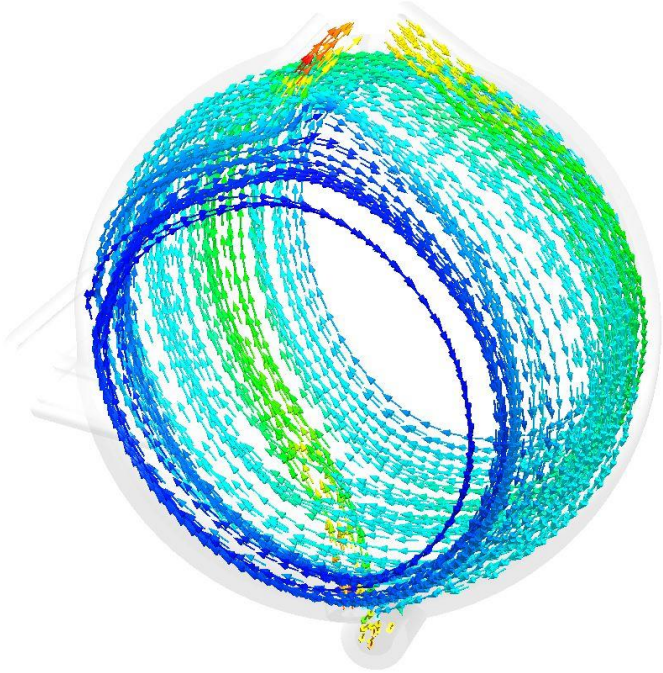

(c)

Figure 4.10: PFSA 45° AOR, (a) Pitch-Yaw, (b) Roll-Yaw, and (c) Roll-Pitch

The AOR induced by the pumps is not limited to 45° and can be varied from 0° to 90° in each of the eight quadrants (Figure 4.11) based on the pump flow directions and the voltage ratio inputs of the operational pumps.

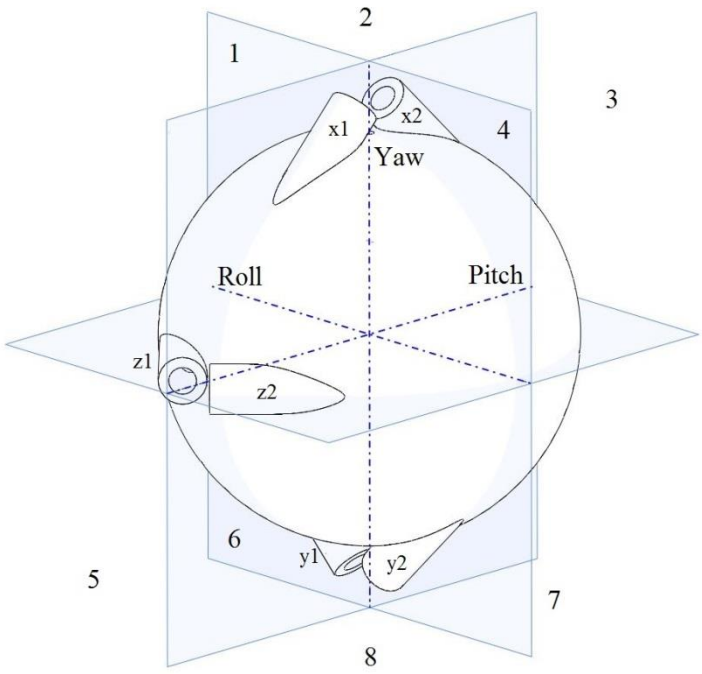

Figure 4.11: Flow Quadrants of PFSA

For instance, to the results in Figure 4.10a as obtained by inlets y1 and z1 as shown in Figure 4.11 and their respective outlets y2 and z2. The AOR that is generated lies on the pitch-yaw plane and is inclined at an angle of 45° due from the roll-pitch plane due to the 1:1 voltage ratio of the pumps (i.e. the flow velocity ratio is also 1:1 due to the linear performance of the pump). By increasing the voltage for the inlets $y1/z1 \geq 1$, the AOR angle will increase linearly between 45° to 90° on the pitch-yaw plane. Conversely, by reducing the ratio of $y1/z1 \leq 1$, the AOR will decrease linearly towards the pitch-yaw plane between 0° and 45°. To better understand the generation of an arbitrary rotation axis using variable voltage ratios, six cases are presented to illustrate this effect and are depicted in Figure 4.12. To obtain the results in Figure 4.12, voltage ratios are applied to two pumps, and a resultant AOR is obtained.

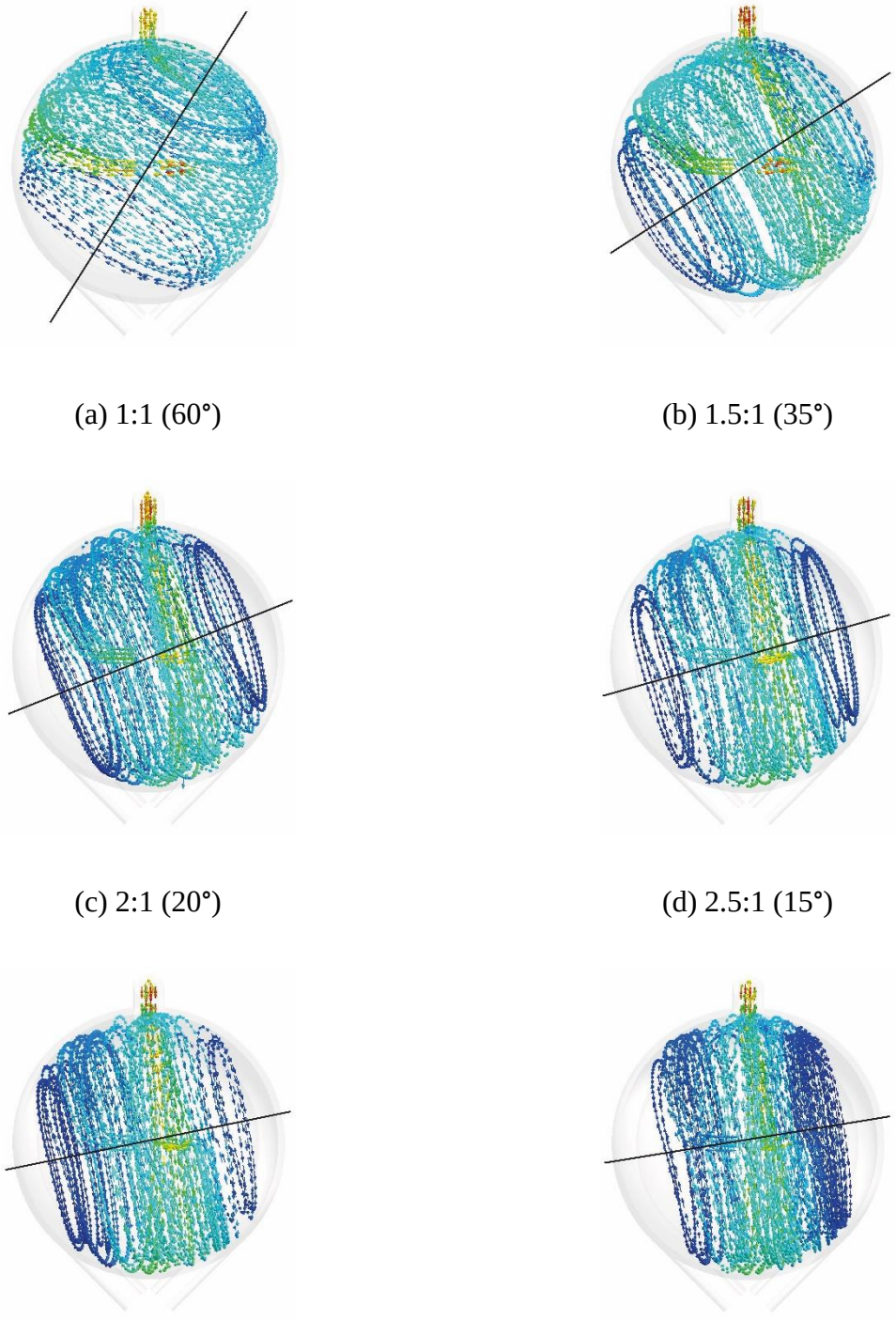

(a) 1:1 (60°) (b) 1.5:1 (35°)

(c) 2:1 (20°) (d) 2.5:1 (15°)

(e) 3:1 (12°) (f) 3.5:1 (10°)

Figure 4.12: Variable AOR using Voltage Ratios on Roll-Yaw

The geometrical location of the pumps dictates the behavioral interaction of the fluid when multiple pumps are operating simultaneously. In order to obtain the optimal pump positions without over-actuating the PFSA, numerous variations of three pumps were considered that would generate control torques about any arbitrary axis when operating simultaneously. The positions presented in this study have been determined to be the optimal configuration. However, the current positions have one drawback when simultaneously operating inlet combinations (z1, x2) and (z2, x2). The reason for this is that the flow from z1 and z2 must travel 180° around the annulus before they interact with the x2 inlet flow. At the point of interaction, the flow velocity of x2 is greater than z1 and/or z2 and therefore provides a bias angle from the 45°. This effect can be recognized by Figure 4.10b wherein the flow AOR is inclined at ~ 60° from the roll-pitch plane in quadrant 4 at a 45° in-plane angle. This notion only exists for the specified inlet and outlet pair due to the difference in travel distance of the flow before contact. In inlet pairs of (x1, y1), (x1, y2), (x2, y1), and (x2, y2) the flow travels 180° from each inlet before contact, and therefore a uniform 45° is evident Figure 4.10c. Similarly, inlet pairs (y1, z1), (y1, z2), (y2, z1), and (y2, z2) have equivalent flow travels of 90° prior to contact and thus also generate a uniform 45° flow.

Lastly, to control the in-plane angle of the PFSA AOR, all three pumps can be simultaneously operated as depicted in Figure 4.13. Three additional planes of rotation can be generated that pass through the roll, pitch, and yaw axes at 45° planes when using 1:1:1 voltage ratios of the three pumps. The flow is able to move from the top four quadrants (1, 2, 3, and 4) in Figure 4.11 to the bottom four quadrants (5, 6, 7, and 8) and vice-versa through the use of the pump direction sequences that generate CMG-like angles. The sequences are presented in Table 4.1 wherein one end of the bidirectional pump may behave as an *Inlet* or *Outlet* to reverse flow direction.

Table 4.1: Pump Direction Sequences for CMG Angles

Pump-Roll	Pump-Pitch	Pump-Yaw
INLET	INLET	INLET
INLET	OUTLET	OUTLET
INLET	OUTLET	INLET
INLET	INLET	OUTLET
OUTLET	OUTLET	OUTLET
OUTLET	INLET	INLET
OUTLET	INLET	OUTLET
OUTLET	OUTLET	INLET

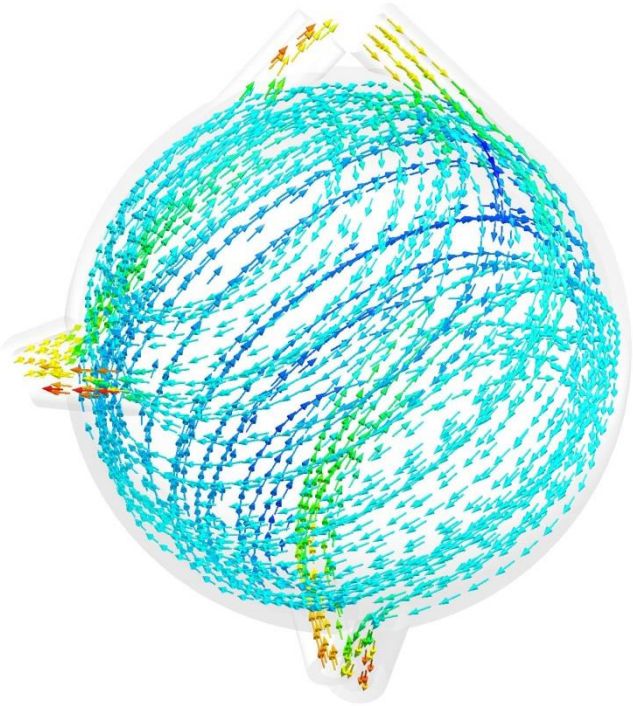

Figure 4.13: PFSA Roll-Pitch-Yaw AOR

As indicated by the results in Figure 4.13, the simultaneous operation of all three pumps allows for the control of out-of-plane AOR. Furthermore, the variability in the voltage ratios between pumps allows for the PFSA to cover variable in-plane and out-of-plane angles in all eight quadrants. This notion enables the PFSA to act as a gimbal and generate CMG-like axes of rotation about its center of rotation. However, due to the flow uneven flow travel distance between the yaw (180°) and pitch (90°) inlets before flow interaction, the 1:1:1 voltage ratio does not produce a 45° AOR about all planes. To alleviate this problem and increase the performance of the PFSA the positional drawback of the pump must be alleviated. This can be accomplished by incorporating one additional pump on the pitch-roll plane to ensure 90° flow interaction with the x1 or x2 inlet.

4.3.1.1 Design Approximation for Active Model

To simplify the complex mathematical model governing the behavior of the fluid inside the spherical annulus, the PFSA can be regarded as a product of sequentially smaller PFLA positioned tangentially alongside one another with reducing radii that maintain tangency about

the surfaces inside the annulus as presented in Figure 4.14. This simplification is introduced since the PFSA can rotate about any necessary arbitrary AOR. Thus, this simplified design ensures rotation about a single AOR. In order to maintain the same wetted surface area as the PFSA's two concentric spheres, 75% of the additional wetted surface area in the simplified design is subtracted to account for an equivalent surface friction.

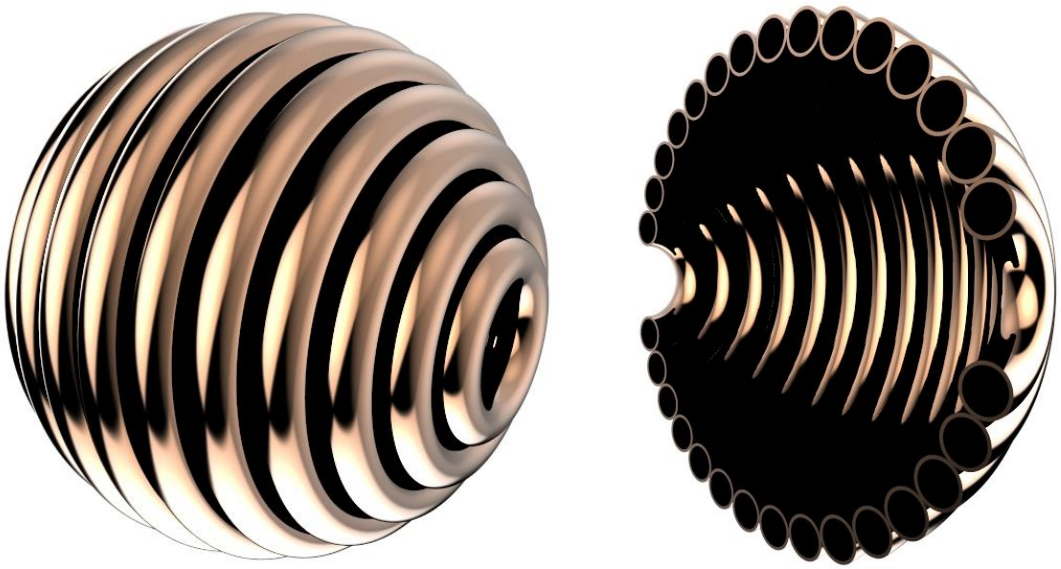

(a) **(b)**

Figure 4.14: Design Simplification for Active Attitude Simulations

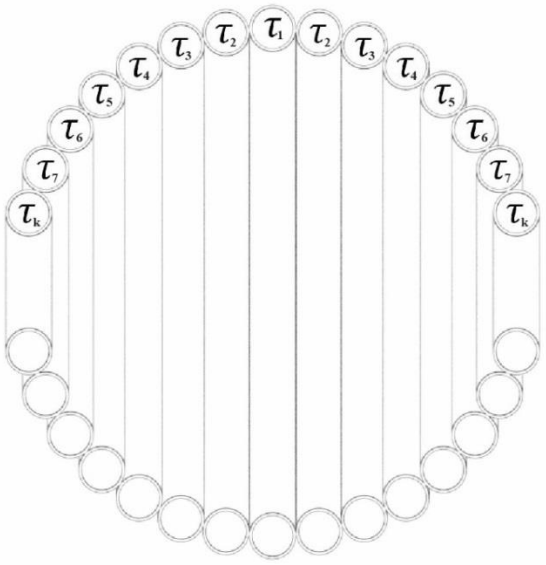

Figure 4.15: Applied PFSA Torque with Design Simplification

With consideration of Figure 4.15, the applied torque of PFSA can be approximated by using the applied torque of a series of connected PFLA and governed by

$$\tau_{fl} = \tau_1 + 2\sum_{i=2}^{k}\tau_i + 0.75\left(\tau_{ff_1} + 2\sum_{i=2}^{k}\tau_{ff_i}\right) \tag{4.4}$$

where k is the number of PLFA required to fill half of the annular cavity inside the PFSA. By using the results obtained through FEA in Section 4.3.1 and the applied torque from Eq. (4.4), the attitude response of the PFSA can be approximated through numerical simulation as presented in the subsequent section.

4.3.1.2 Attitude Maneuver Simulation

To compare the active attitude maneuver performance of the PFSA with that of the PFLA, the initial attitude conditions are selected to match those of Section 3.3.1.2.

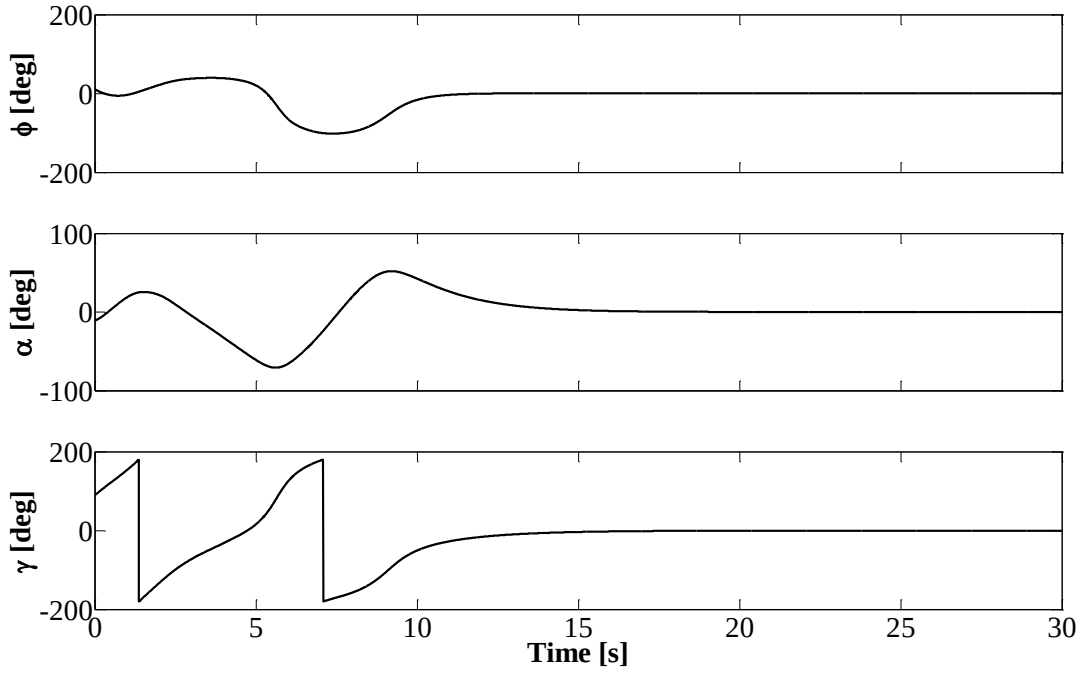

Figure 4.16: Satellite Attitude Response

It is evident from Figure 4.16 that the satellite reaches its desired attitude through a P2P maneuver in approximately 17.5 seconds. The attitude simulation results of the PFSA using the

simplified mathematical model are comparable to those obtained previously using the PFLA for the same maneuver as presented in Figure 3.6. Although the profile of the two cases is different due to the increase in frictional torque by a factor of approximately 1.5 as described by Eq. (4.4), both actuators are able to stabilize the satellite with similar settling times.

4.3.2 Passive PFSA

To overcome the limitations existing with the PFLA, in this section the PFSA's unique ability to imposed control torques about any arbitrary resultant axis of rotation of a satellite subject to an external disturbance is addressed. The novel geometrical design of the PFSA alleviates the assumption of $D \gg r$ as considered when analyzing the PFLA system for passive stabilization. In the case of the PFLA, since the cross-sectional radius r of the tube must be much smaller than the diameter of the loop D, the limitation imposes that a torque must only act about the torque axis of the loop or the frictional torque will not be significant to damp the satellite motion. Conversely, with the spherical design of the PFSA, the fluid is free to rotate about any arbitrary axis and is not limited to the assumption aforementioned. For the results presented herein, one direction of the flow is considered since the spherical design ensures symmetry about any arbitrary axis.

4.3.2.1 Passive Stabilization

Passive stabilization techniques including passive magnetic stabilization, gravity gradient stabilization, and aerodynamic stabilization in LEO harness the geometric and magnetic design of the satellite to passively stabilize the satellite. In general, stability is often only achieved about two of three rotation axes. For magnetic stabilization, the rotation about the magnetic axis is uncontrolled; for aerodynamic stabilization techniques, the roll is typically uncontrolled; and the boom axis is uncontrolled for gravity gradient methods. This section considers the practical passive stabilization application of fluid actuators that has not yet been considered in the literature. It is evident that studies in the literature, to date, [29, 30] make one critical assumption that does not apply in the real applications. This assumption is such that the fluid in PFLA loops can rotate about any eigen-axis and thus can provide passive stabilization through the fluid wall friction and satellite momentum exchange. However, this assumption is invalid for all external

disturbance cases but one; when the disturbance forces generate torques that act directly about the rotational axis of the PFLA. To mitigate this assumption, the works in the literature use PFLA with a loop diameter much greater than that of its cross-section.

4.3.2.2 Satellite Model

In this section, the satellite dynamic equations governing the passive stabilization of a satellite using fluid is presented. The fluid dynamics differ herein as compared to active control due to the absence of a pump. Herein, the control torque from the fluid is not due to the motor but rather the frictional torque generated between the fluid and walls.

For passive stabilization, the angular momentum stored in the satellite is transferred to the freely-rotating fluid inside the cavity, and the frictional torque acts to dampen the rotation of the satellite. The lossless angular momentum transfer between the fluid H_{fl} and the satellite H_s are represented by the continuity equation as adopted from Eq. (2.31) as

$$\left(J_s + J_{fl,sum}\right)\dot{\omega}_{BI}^{B} = -\omega_{BI}^{B\times}\left(J_s\omega_{BI}^{B} + J_{fl}\omega_{fl} + J_{fl,sum}\omega_{BI}^{B}\right) - \tau_{fl} + \tau_e \tag{4.5}$$

The resultant fluid angular velocity caused by the angular momentum exchange of the satellite onto the fluid can be described by Eq. (2.23) and Eq. (2.30) when $\tau_m = 0$ and $\tau_{mf} = 0$.

$$J_{fl}\dot{\omega}_{fl} + J_{fl,sum}\dot{\omega}_{BI}^{B} = \tau_{fl} = -\tau_f \tag{4.6}$$

By substituting the fluid velocity obtained from Eq. (4.6) into Eq. (2.20), the damping friction torque can be found for passive stabilization.

Passive stabilization using fluid can allow for greater fluid velocities to be obtained in the loops and cavities as the angular velocity of the fluid is no longer limited to motor saturation limits. As such, the effect of increased fluid velocity can produce friction torques that are greater than those presented during forced pump flow, to effectively stabilize a disturbed satellite by passively damping the angular velocity of the satellite to zero ($\omega_{BI}^{B} = 0$).

In works conducted in the literature have examined passive stabilization for only small initial angular velocities and have not addressed the effects of large initial angular errors and their corresponding satellite response. Herein, several initial velocity conditions have been examined

to determine the effects of using fluid for both small and large initial disturbances and the performance of the fluid for such cases.

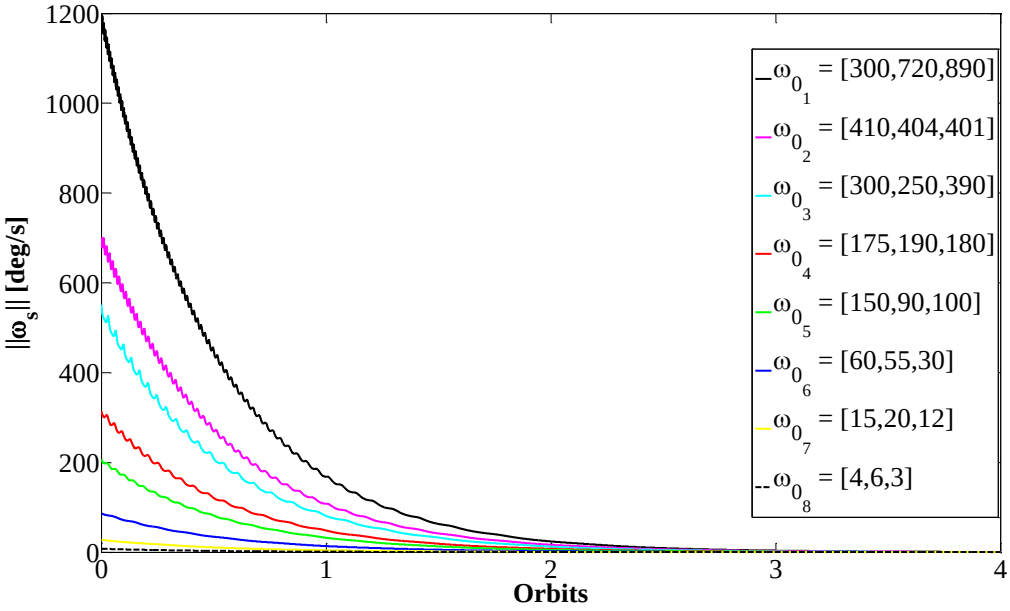

Figure 4.17: Effect of Initial Satellite Angular Velocity on Passive Stabilization

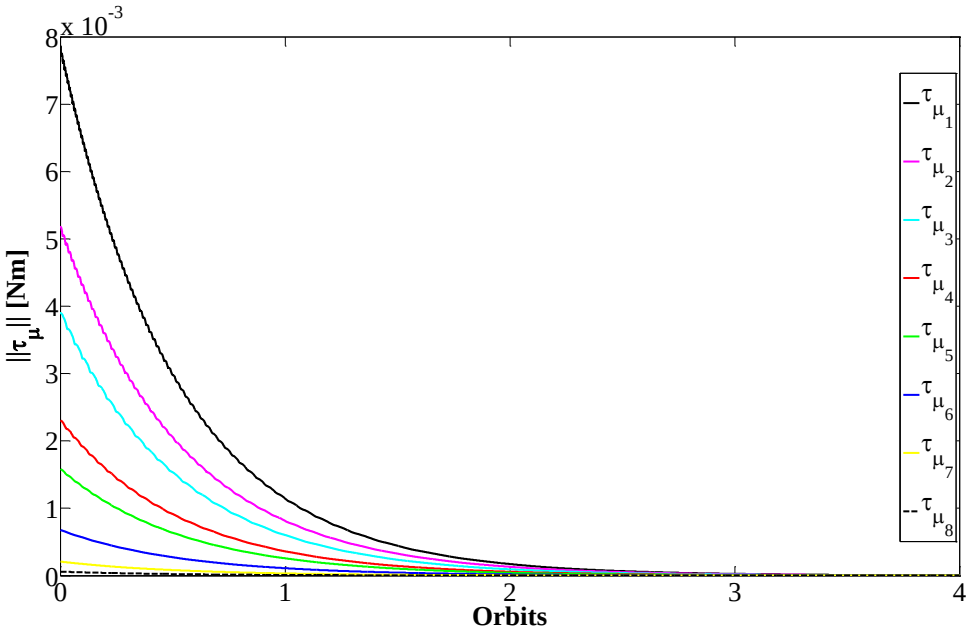

Figure 4.18: Effect of Initial Satellite Angular Velocity on Friction-Torque

By examining the initial angular velocities from Figure 4.17 with their corresponding friction torque profiles in Figure 4.18, it is evident that a trend exists wherein the magnitude of the friction is proportional to the angular velocity of the satellite. The response is negative exponential wherein the rate of change of the friction torque is greater at higher velocities and reduces exponentially as the velocity of the satellite approaches zero. Furthermore, by a closer examination of the oscillatory profile in the norm of the angular velocity, it is clear that the oscillations are in agreement with those depicted in [29]. It has also been examined that the governing factors that affect the settling time are in fact attributed directly to the viscosity of the fluid and the geometry of the fluid cavities as governed by Eq. (2.18) to Eq. (2.20).

Effects of Fluid Viscosity and Density

The effect of fluid viscosity and fluid density on the satellite attitude response is also examined. Fluid viscosity and density are increased and decreased one at a time by a multiple of 10 while other fluid parameters are maintained as constant. The results are illustrated in Figure 4.19 and Figure 4.20, where it is examined from Figure 4.19 that as the fluid viscosity increases, the settling time decreases and vice versa. Conversely, as the fluid density increases in Figure 4.20, the settling time also increases.

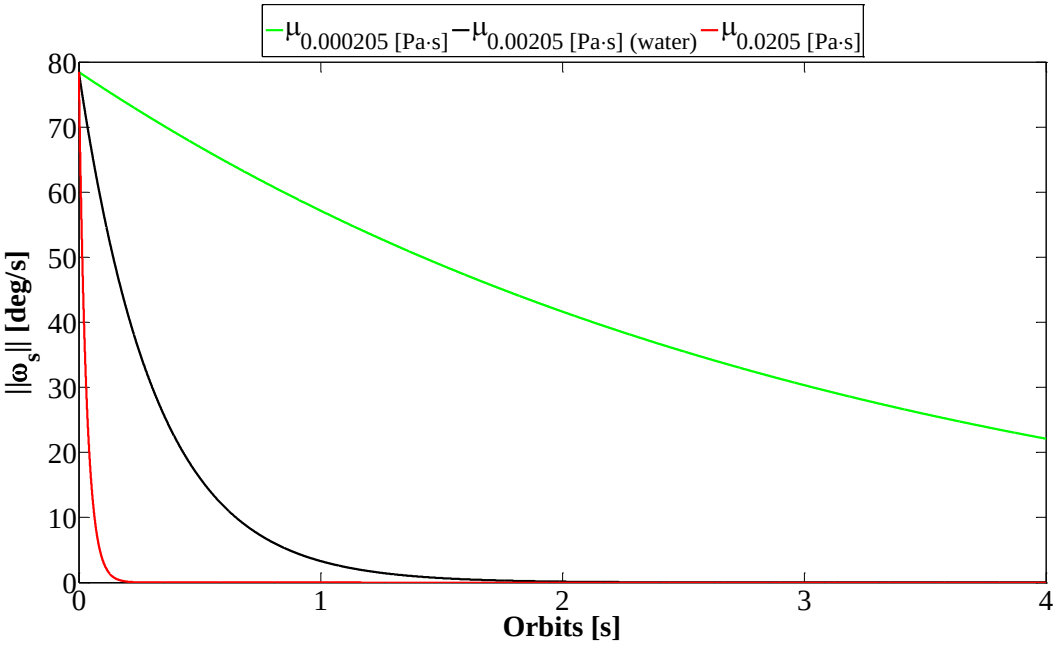

Figure 4.19: Effect of Fluid Viscosity on Satellite Attitude Response

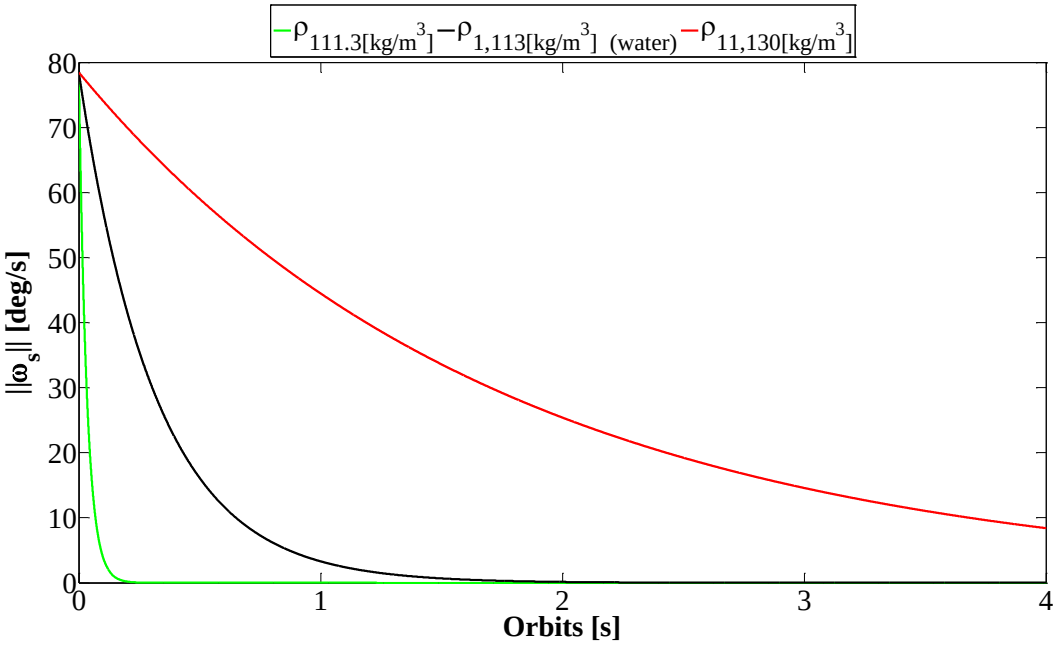

Figure 4.20: Effect of Fluid Density on Satellite Attitude Response

4.3.2.3 Computational Fluid Dynamics Simulation

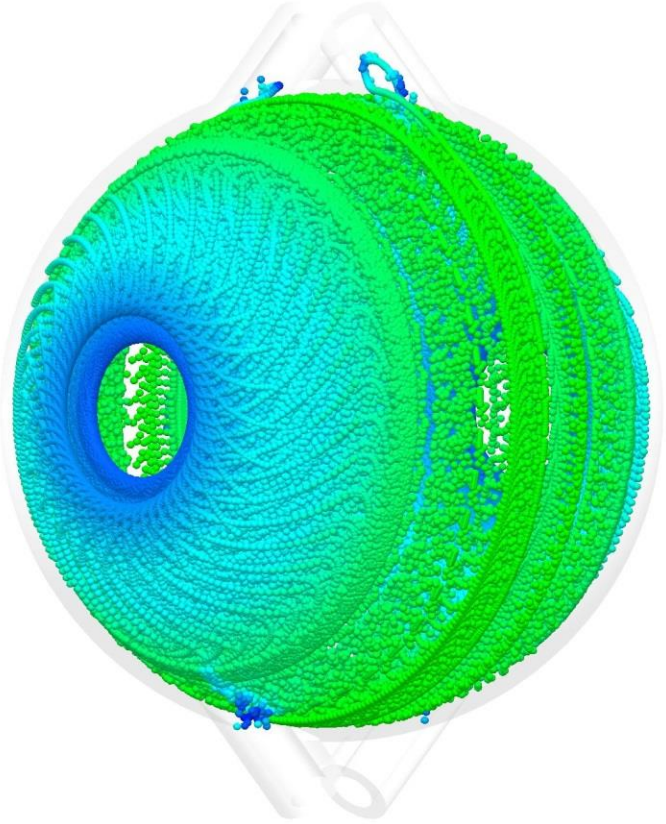

Figure 4.21: PFSA Passive Fluid Rotation

To illustrate the motion of the fluid inside the PFSA without active pumps, and only through the angular momentum transfer between the satellite and the PFSA, the satellite was subjected to an angular velocity of 5 rad/s about the yaw axis. Since the PFSA is fixed to the satellite body, the same angular velocity is induced onto the PFSA walls. The walls are defined as real walls inside the simulation boundary conditions and no inlet or exit velocity, or pressure is defined. The rotation of the fluid as depicted in Figure 4.21 is due to the friction effects at the wall surfaces inside the cavity and the angular momentum exchange between the satellite and the fluid. By examining the left most side Figure 4.21 (blue region), a torsional profile is visible about the rotation axis. This torsion is due to the viscosity of the fluid and demonstrates the no-slip wall

boundary conditions of the flow; wherein the fluid velocity at the fluid-solid boundaries is equal to that of the solid boundary.

The friction torque generated on the inner surfaces of the annulus have been extracted from SolidWorks CFD, and an equation relating the friction torque to the fluid angular velocity for the geometry considered herein has been obtained using a curve-fitting function governed by the second-order polynomial equation:

$$\tau_{ff} = -\left(sgn\left(\omega_{fl}\right) \cdot 2.47e^{-8}\omega_{fl}^2 + 3.46^{-7}\omega_{fl}\right) \tag{4.7}$$

The wetted surface area of the PFSA is 31294.67 mm^2 compared to 12534.4 mm^2 for the PFLA. The significant increase in fluid-solid interaction results in increased friction by approximately one order of magnitude even though the diameter of the PFSA is ~2.1 times smaller than that of the PLFA. To better examine the passive advantage of the PFSA over the existing PFLA, Eq. (4.7) is used to examine the passive stabilization performance of a satellite equipped with the PFSA at its center of rotation; the results are presented in the following section.

4.3.2.4 Passive Attitude Stabilization Simulation

In this section, the performance enhancement gained from the increased surface area of the PFSA as opposed to the PFLA with respect to friction torque is demonstrated. The initial satellite state is subject to the following initial conditions $\theta_0 = (0° \; 0° \; 0°)$ and $\omega_{BO_0} = (62, \; -45, \; -17) \; °/s$. By examining the results presented herein, it is evident that the satellite equipped with the PFSA stabilizes in ~ 15 orbits as opposed to 40 orbits as was obtained by using the PFLA in [29, 30].

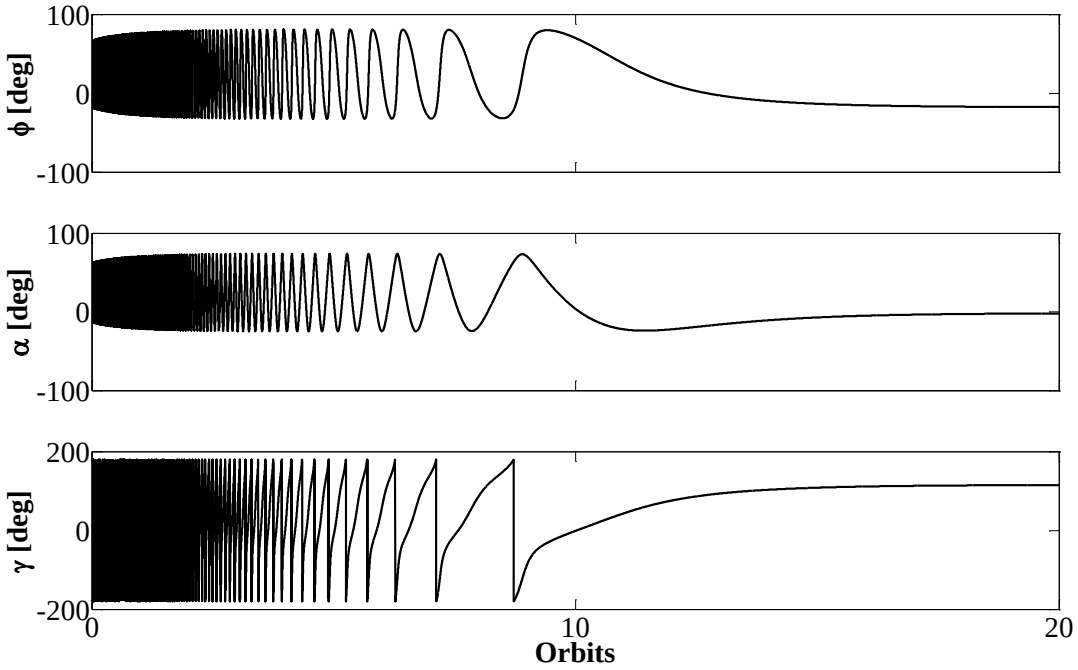

Figure 4.22: Attitude Response for Passive Stabilization using PFSA

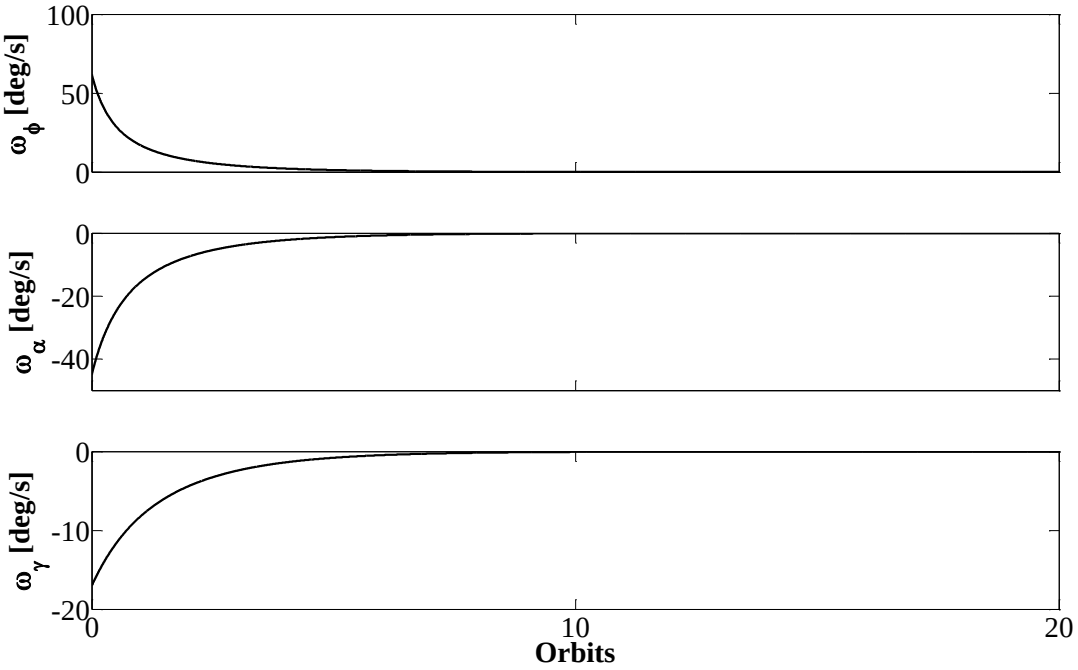

Figure 4.23: Satellite Velocity Response for Passive Stabilization using PFSA

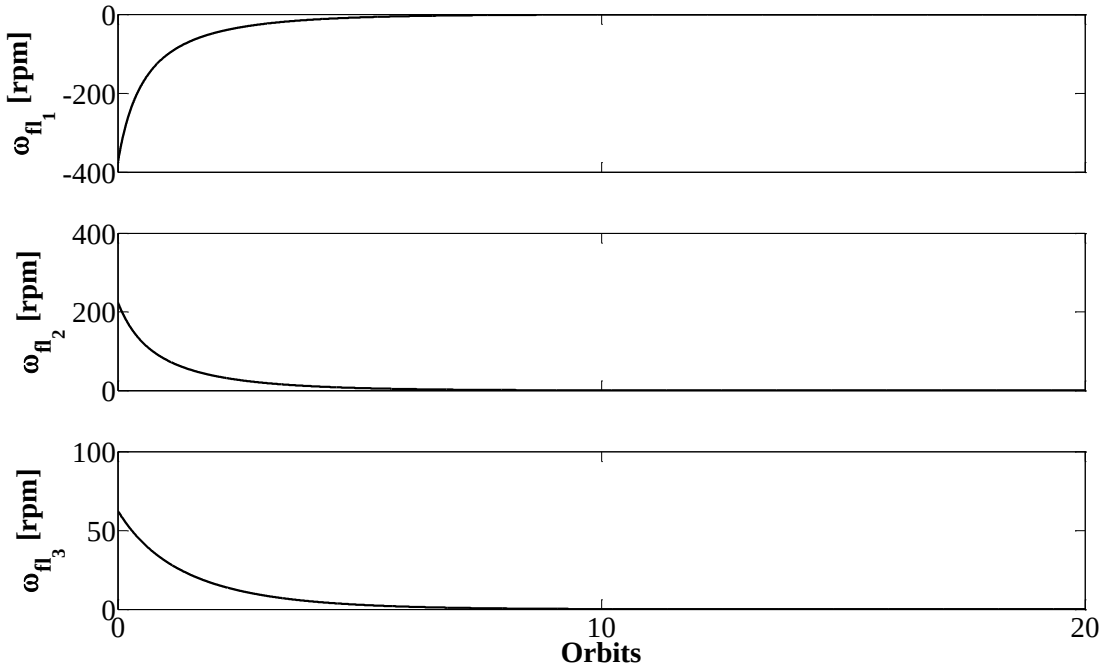

Figure 4.24: Fluid Angular Velocity for Passive Stabilization using PFSA

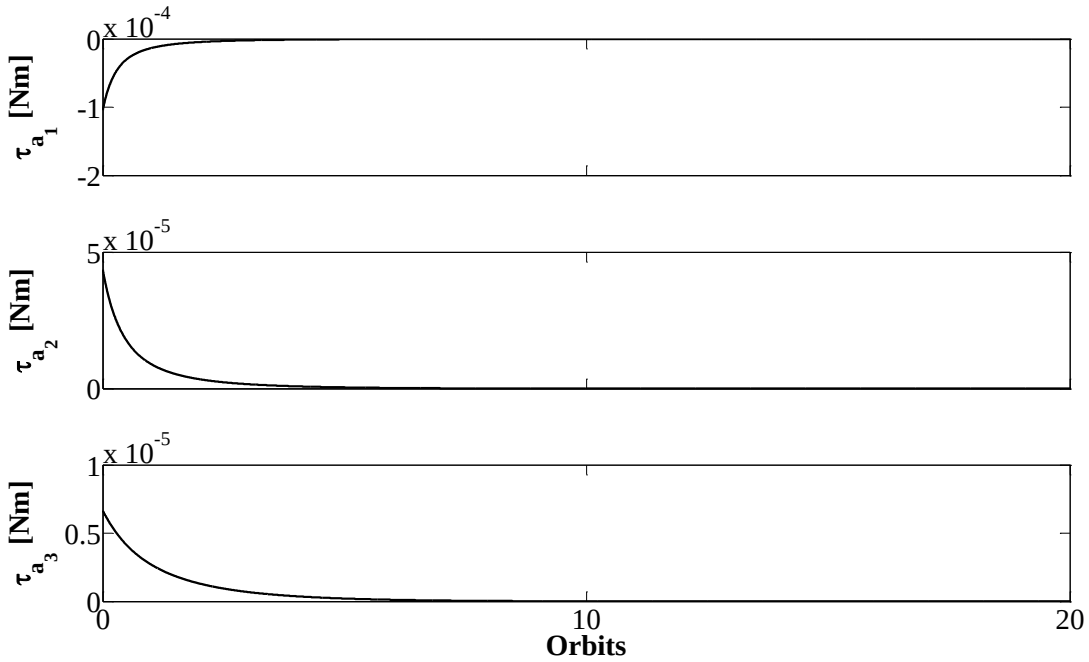

Figure 4.25: Passive Stabilization Friction Torque from PFSA

In line with the approximate three-fold increase of wetted surface area in the PFSA cavity as opposed to the PFLA tube, the friction torque has increased by one order of magnitude and supplements the reduction in settling time.

Furthermore, by examining the response of the satellite angular velocity, it is evident that the profiles between [29] for the passive PFLA differ greatly from those presented in Figure 4.23 while using the PFSA. The PFLA profile suggests that the satellite experiences clockwise and counter-clockwise oscillations before settling. However, with the PFSA the satellite angular velocity is reduced without oscillation. This notion is caused by the unique ability of the PFSA to provide stabilization torque directly about the Euler-axis of rotation of the satellite; the rotation of the satellite about the single Euler-axis is simplified into a single-axis problem for the PFSA, and therefore the three-axis stabilization results generate single-axis response profiles for passive stabilization.

The spherical configuration of the PFSA allows for passive stabilization performance that is superior to that achieved by the PFLA without the need for PFLA geometrical assumptions.

4.3.2.5 PFSA as an Angular Rate Sensor

To further the performance capabilities and the application using fluid actuators, this section examines the use of fluid to obtain attitude information in the event of rate gyro sensor failure for passive attitude stabilization. Without rate gyro information, the satellite command and data handling (C&DH) unit would be unable to determine if the satellite has been stabilized. Herein, the conservation of angular momentum is used to establish the relationship between fluid velocity and the satellite angular velocity while considering the dynamic equation adopted from Eq. (2.31) as

$$\left(J_s + J_{fl,sum}\right)\dot{\omega}_{BI}^{B} = -\omega_{BI}^{B\times}\left(J_s\omega_{BI}^{B} + J_{fl}\omega_{fl} + J_{fl,sum}\omega_{BI}^{B}\right) - \tau_{fl} + \tau_e \tag{4.8}$$

Since $\omega_{BI}^{B\times}\left(J_s\omega_{BI}^{B} + J_{fl}\omega_{fl} + J_{fl,sum}\omega_{BI}^{B}\right) \ll \left(J_s + J_{fl,sum}\right)\dot{\omega}_{BI}^{B}$ the simplified equation governing the angular velocity of the satellite from the fluid velocity can be approximated as

$$\dot{\omega}_{BI}^{B} = -\left(J_s + J_{fl,sum}\right)^{-1}\left(J_{fl}\dot{\omega}_{fl} - \tau_e\right) \tag{4.9}$$

In the event of sensor failure where the angular velocity of the satellite is no longer available, the fluid angular acceleration, $\dot{\omega}_{fl}$, that may be obtained in practice using hall sensors, can be used to determine the velocity of the satellite and relay that information back to the C&DH by integrating Eq. (4.9).

To understand this theory, it is evident from Figure 4.23 and Figure 4.24 that the in event of failure of the rate gyro, due to the proportionality of the fluid angular velocity and the satellite body rate, the fluid angular velocity can be used as a substitute to obtain the satellite angular velocity. The fluid velocity information can then be relayed to the C&DH of the satellite in order for the attitude determination subsystem to know when the satellite has stabilized about its new equilibrium attitude. In passive stabilization, since the fluid velocity behaves the same as that of the satellite however in the opposing direction, the equivalence in profile allows for the rate sensor information to be extracted from the fluid rotation.

4.4 Conclusions

In this chapter, a novel fluid actuator is proposed. The actuator, termed PFSA, takes advantage of spherical design for both active and passive satellite attitude control. The design of the PFSA is proposed, and CFD results are presented to illustrate the flow performance of the PFSA for variable voltage ratios. The torque generated by the novel actuator is examined through FEA, and its advantages in generating CMG-like angles are outlined. The torque generated by the PFSA is obtained and examined to be comparable to the performance of the PFLA for active control as found in the literature. A 3D printed prototype of the PFSA was manufactured and tested in a lab environment. The initial experimental results indicate ~ 15.8 mNm of torque generated about a single axis, yielding an accuracy of ~ 90% when compared with active CFD simulation results presented herein. More comprehensive experimentations should be conducted in order to fully define the attitude performance of the proposed actuator.

CFD simulation results are used to obtain the torque model for the active and passive methods of the PFSA. The obtained models are simulated using MATLAB to examine the performance of the proposed actuator. The results indicate the feasibility of the PFSA for active control. Furthermore, it is demonstrated that due to the increased wall surface area, greater performance

is achieved for passive stabilization when using the PFSA as opposed to the PFLA. The friction torque generated by the PFSA is greater than that of the PFLA by approximately one order of magnitude.

The effect of the initial angular velocity on the settling time of passive stabilization has been examined. The results of eight different cases indicate that the settling time is independent of the initial velocity and is dominantly affected by the viscosity of the fluid and the geometry of the fluid cavities. Furthermore, with increasing initial satellite angular momentum, the settling rate of change of the satellite decreases exponentially. The results of passive stabilization also suggested that the upper fluid saturation limit of 5.25 rad/s associated with active control can be surpassed in passive methods since the primary method of fluid motion is due to the angular momentum exchange between the fluid and the satellite. It is also illustrated that the fluid is able to store greater angular momentum in its passive state as opposed to its active state since it is not limited by the pump performance.

The fluid motion inside the loops is then proposed as a supplementary replacement for the satellite rate gyro in the event of sensor failure. Due to the conservation of angular momentum exchange between the freely rotating fluid inside the loops and the satellite body, the angular momentum relation is used to obtain the satellite velocity from the ideal fluid motion. The simulated results indicate the feasibility of the proposed method.

The results presented in this chapter set the foundation for a novel actuator device for satellite attitude control that is capable of generating control torques about any arbitrary axis of rotation. The proposed actuator simplifies three-axis passive stabilization into a single-axis problem and dampens external disturbances more effectively and efficiently than other fluid actuator devices.

CHAPTER 5
THERMAL MANAGEMENT USING PFLA

SMALL satellites are often the preferred option for Earth observing missions due to their low cost. Modern space missions require complex payloads and thus result in increasing the overall satellite mass/volume budget. With increasing subsystem complexity, microelectromechanical (MEMS) systems are used to reduce cost, weight, and, power consumption. However, with continual high-performance requirements, heat is a by-product of the onboard electrical circuit in addition to the heat absorbed from the space environment. Satellites require thermal management systems to ensure the subsystems operate within their optimal performance characteristics to ensure the lifetime of the mission. The idea of combining subsystems to reduce weight and cost has become of increasing interest for researchers. In this chapter, the PFLA system is proposed as a combined attitude and thermal management system (CATMS).

Satellite thermal heating is categorized under two classifications: environmental heating and dissipative heating. Environmental heating, as the name suggests, is due to the energy interaction between the satellite's external surface and the space environment, primarily in the form of radiation caused by solar waves, charged particles, and other heavenly bodies. Environmental heating is generally managed by either reorienting the satellite body or by chemically treating the external surfaces. In contrast to environmental heating that is expansive and acts on the external surfaces of the satellite, dissipative heating is energy generated in the form of heat and typically released inside the satellite enclosure. All electrical subsystems inside the satellite dissipate heat during their operation. The heat is controlled by redirecting the energy to the external surfaces, via heat sinks and heat pipes that operate through convective and conductive heat transfer, where it is then rejected to the space environment.

This study begins with a literature review of fluid based heat transfer methods in Section 5.1 and heat transfer theory in Section 5.2. A redesign of the PFLA for thermal management is presented in Section 5.3. Numerical simulations of the fluid heat transfer from a simulated satellite body are examined in Section 5.4 followed by conclusions in Section 5.5.

5.1 Literature Review

The concept of using fluids in space has become of increasing interest with advancements in fluid sealing technologies; most notably, the use of fluid for thermal heating and cooling of satellite components to maintain their allowable operating temperatures. A promising technology is through the use of micro-electromechanical systems (MEMS) that circulate fluid through microchannel heat exchangers via a pump - to remove excess heat from electronic components as analyzed in the works of Birur et al. [66].

Heat pipes are common passive mechanisms used to effectively transport excess heat from electrical devices to onboard heat sinks, thereby allowing the energy to dissipate into space [67]. A heat pipe is a sealed evaporator-condenser system that contains a wick structure lined on the inner surface of the pipe. The type of fluid and pressure inside the pipe is reflective of the desired operating temperature of the structure. As heat is applied to the pipe, the liquid in the wick evaporates and spills through to the hollow inner core as depicted in Figure 5.1. As the vapor diffuses down the length of the pipe, it enters an adiabatic state wherein the liquid and vapor phases of the fluid flow in opposing directions through the core and the wick. The vapor then enters the condensation stage due to the thermal gradient caused by a heat sink (condenser) and heat is rejected from the source [68].

Heat pipes have proven application in aerospace, and they transport thermal energy at rates far greater than most efficient solid conductors and provide a superior energy-to-weight ratio. Recent investigations have been carried out to develop a miniature loop heat pipe (LHP) which is comparable to heat pipes with the advantages of longer operating durations and can operate independently of gravitational forces [69].

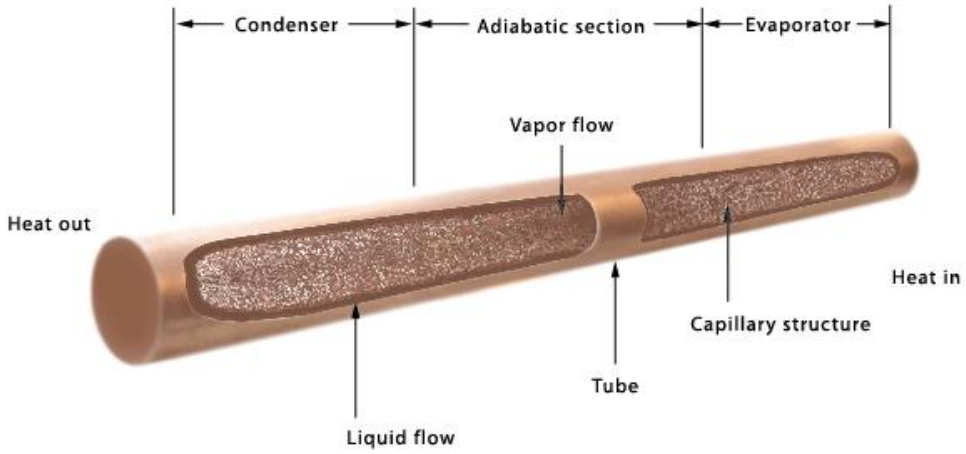

Figure 5.1: Heat Pipe [70]

Ku et al. [71] discuss the development of LHPs with two integrated evaporators and condensers. Their designs suggest the viability of such systems for serving as a thermal bus for multiple instruments onboard the satellite while reducing mass and radiator power requirements. Similar works by Wang et al. [72] demonstrate the high-performance and reliability of heat pipes for thermal management of miniature satellite. Several other investigations [73-77] confirm the validity of using LHPs to regulate the temperature of electronic components. In a recent publication by Ellis et al. [78] from Advanced Cooling Technologies Inc. two methods for passively managing the thermal environment for avionics in high temperatures are demonstrated; one approach of which uses the concept of LHPs to transport thermal energy to heat sinks. This method revealed a reduction in the temperature gradient by approximately 25°C.

In a similar attempt to dissipate undesired heat from electronics, [79] presents a MEMS-based approach using liquid metal mercury as the working fluid to provide thermal management. With metals having superior thermal properties in comparison to water or alcohol based fluids this method outperformed water-filled heat pipes by a multiple of 2.7. Jia et al. [80] demonstrated through simulation the feasibility of a MEMS-based micro-channel that provides adequate cooling for a nanosatellite (satellite 1-10kg) using active thermal control strategies. Although several other techniques for monitoring and managing the thermal environment of electronics and satellite do exist [81-85] the methods considered for the purpose of this research pertain to those requiring the transport of fluid across channels and heat pipes as these methods can also act

as attitude control mechanisms by exploiting the momentum from the motion of the fluid. It is well known that satellite consist of various subsystems that work in parallel to perform the mission at hand, as demonstrated here; two of such systems are the attitude control and thermal management subsystems. However, with increasing the number, and inherently the mass of subsystems onboard, the cost of launch is proportionally affected. To address the increasing demand for producing lighter and more reliable satellite the industry is researching in methods to combine the functionality of multiple subsystems into one multi-purpose unit, CATMS.

5.2 Heat Transfer Model

In this section, the heat transfer models are presented. Typically, in the vacuum of space, the primary mode of heat transfer is through radiation; conduction and even more so convection are almost non-existent. However, the existence of a moving fluid medium inside the PFLA introduces convection effects between the fluid and loop walls and therefore must be examined in order determine the effective thermal management performance of the PFLA. In this section, the thermal models are presented as applicable to a satellite equipped with PFLA.

5.2.1 Conduction

Conduction is defined as the transfer of energy from high energy particles to those of lesser energy due to particle interaction. In gaseous and liquid states, conduction occurs due to the random collisions and diffusion of active molecules. In solid states, conduction is owed to molecular vibration in the lattice structure, and the transport of energy by free electrons and is directly proportional to its *thermal conductivity*, k – a measure of the ability of a material to conduct heat. The rate of heat conduction through a medium is proportionally influenced by the temperature gradient across it and the heat transfer area, and inversely proportional to the geometric thickness of the medium and governed by

$$\dot{Q}_{cond} = -kA\frac{\Delta T}{L} \tag{5.1}$$

where L is the medium thickness, A is the area, and $\Delta T = T_2 - T_1$ is the temperature change across the medium. Eq. (5.1) suggests that the rate of heat conduction in a given direction is

proportional to the temperature gradient in that direction and is referred to as *Fourier's Law of Heat Conduction.*

5.2.2 Convection

Convection is the method of energy transfer between a solid body and an adjacent liquid or gas that is in motion. Convection involves the effects of both conduction and fluid motion. The convection heat transfer is directly proportional to the velocity of the fluid. However, in the absence of bulk fluid motion, heat transfer occurs solely through conduction with an adjacent solid body. Two categories of convection exist: forced and natural. *Forced convection* occurs when fluid is forced to flow over the surface by external means such as a pump. In contrast, *natural convection* occurs when density differences due to temperature gradients induce buoyancy forces on a fluid. Heat transfer processes that involve the phase change of a fluid, as in heat pipes presented in Section 5.1, are considered to be convective as fluid motion is induced during the process.

The rate of convective heat transfer is directly proportional to the temperature difference and expressed by *Newton's Law of Cooling* given by

$$\dot{Q}_{conv} = hA_s(T_s - T_\infty) \tag{5.2}$$

where h is the convection heat transfer coefficient obtained experimentally whose value depends on multiple factors such as surface geometry and bulk fluid velocity and does not only express fluid properties. The value of h ranges between 10-1000 W/m^2·°C for free convection of liquids and 50-20,000 W/m^2·°C for forced convection of liquids. A_s is the surface area through which convection occurs, T_s is the surface temperature, and T_∞ is the fluid temperature sufficiently far from the surface. At the surface of the solid body, the fluid temperature and body surface temperature are equal. Simply put, convection is "conduction with fluid motion".

5.2.3 Radiation

Radiation is the energy emitted by matter in the form of photons due to changes in the configurations of electrons in atoms or molecules. Unlike conduction and convection which require a medium in order to transfer energy, radiation does not require any medium and is the

primary source of thermal energy transfer in the vacuum of space. *Thermal radiation* is one form of electromagnetic radiation that is emitted by all bodies given that their temperature is above absolute zero or -273.15 °C. The radiation emitted internally in materials such as metals and wood never reaches the surface, and surface radiation incident on such bodies is typically absorbed within a few microns from the surface. The maximum radiation emitted from a surface of area A_s is governed by the *Stefan-Boltzmann Law* as

$$\dot{Q}_{emit} = \varepsilon \sigma A_s {T_s}^4 \tag{5.3}$$

where T_s is the thermodynamic surface temperature, $\sigma = 5.67 \times 10^{-8} W/m^2$ is the Stefan-Boltzmann constant, and $0 \leq \varepsilon \leq 1$ is the surface emissivity that measures how closely a real surface resembles a *blackbody* - an idealized body that emits the maximum radiation for which $\varepsilon = 1$.

Complementing the emissivity of a surface, the *absorptivity* α describes the fraction of radiation incident on a surface that is absorbed by the surface and has a value of $0 \leq \alpha \leq 1$, where $\alpha = 1$ is a blackbody that completely absorbs the radiation incident on it. Generally, α and ε of a given surface are dependent on temperature and radiation wavelength and are equal. Therefore, the rate at which a surface absorbs radiation can be obtained from

$$\dot{Q}_{absorb} = \alpha \dot{Q}_{incident} \tag{5.4}$$

and the portion of the radiation that is reflected away from the opaque surface is calculated by

$$\dot{Q}_{ref} = (1 - \alpha) \dot{Q}_{incident} \tag{5.5}$$

The net radiation heat transfer is calculated as the difference between the energy absorbed and the energy emitted and governed by

$$\dot{Q}_{net} = \dot{Q}_{absorbed} - \dot{Q}_{emit} \tag{5.6}$$

In general, it is difficult to determine the net heat transfer rate between two surfaces since it depends on multiple factors such as the properties of the surfaces, their orientation relative to one another, and the interaction of radiation with the medium in between the surfaces. However, a simplification of this model can be governed by

$$\dot{Q}_{rad} = \varepsilon\sigma A_s\left({T_s}^4 - {T_{surr}}^4\right) \tag{5.7}$$

wherein Eq. (5.7) describes the net rate of radiation between a surface with emissivity ε and area A_s at temperature T_s that is entirely enclosed by a larger surface with temperature T_{surr} and are completely separated by a gas that does not intervene with radiation. This is a special case that does not consider the emissivity and surface area of the surrounding face thereby suggesting that the heat transfer radiation rate from the surround body is negligible.

Radiation heat transfer of a surface that is surrounded by a gas occurs in conjunction with conductive and/or convective heat transfer between the surface and the gas. Radiation is typically superior to conduction or natural convection, but negligible relative to forced convection. Applications using forced convection that involve surfaces of low emissivity and low to moderate temperatures generally disregard radiation heat transfer.

5.3 Design of PFLA for Thermal Management

The unique properties of the PFLA allow for a device that can provide convective heat transfer in an environment where convection is otherwise non-existent. To examine the thermal management capabilities of the PFLA in this chapter we consider the thermal interaction between the satellite, the electronics onboard, and, the PFLA.

To exhibit thermal conduction through the copper body of the PFLA, the contact surface area between the loop and the heated surface must be maximized. The modern design of the fluid loop as a tube with a circular cross-section Figure 5.2(a) as examined by [29, 31, 86] does not allow for sufficient contact area with the satellite body and thereby cannot be used as an effective means of thermal energy transport, even though conduction. Herein, the cross section of the traditional PFLA is analyzed as a square with a circular cut-out Figure 5.2(b) in order to maximize the heat flux and thermal energy transfer between contacting surfaces. The proposed design has no effects on the attitude control performance capabilities; it simply provides the PFLA with thermal management capabilities.

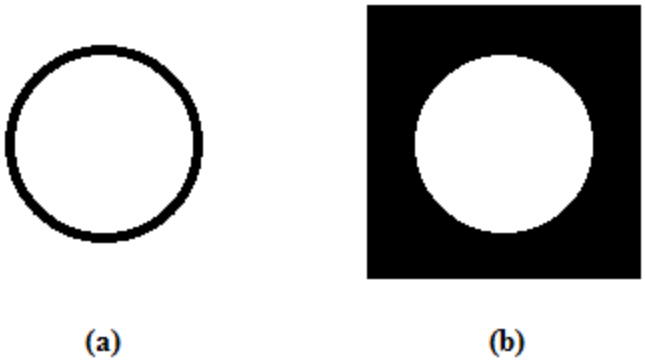

Figure 5.2: PFLA Cross-Section, *(a) Traditional, (b) Proposed*

The unique properties of the proposed PFLA allow for both conduction and convection to exist in the vacuum of space. Conduction will occur between the PFLA copper loop and the surface(s) it contacts i.e. PCBs or satellite structure. The thermal energy absorbed by the copper is transferred to the fluid by conduction and/or convection. The thermal energy is then dissipated from of the loop into a region of lower temperature. Generally, a greater contact surface area will result in increased thermal heat flux from one body to another. Furthermore, the presence of fluid inside the loops of the PFLA allow for energy transport through convection as the flow of fluid inside the loops is able to carry thermal energy across the loop. However, during the absence of fluid motion when the satellite is stabilized and requires no control torque input, the convective terms are null, and only conduction occurs between the fluid and the loop walls.

5.4 Heat Transfer Simulation Results and Discussion

In this section, results are presented to demonstrate the thermal management performance of the PFLA. Numerical simulations have been carried out using SolidWorks 2010 Flow Simulation. For each case considered in this section, the respective grid independent solution has been obtained to ensure the validity of the CFD results. The mesh inside the loop has been optimized to ensure the boundary layer is well captured by using increased mesh in the near wall region of the fluid-solid contact surface. In order to simulate a space-like control volume, an internal assessment is carried out to eliminate any convection effects with the external environment.

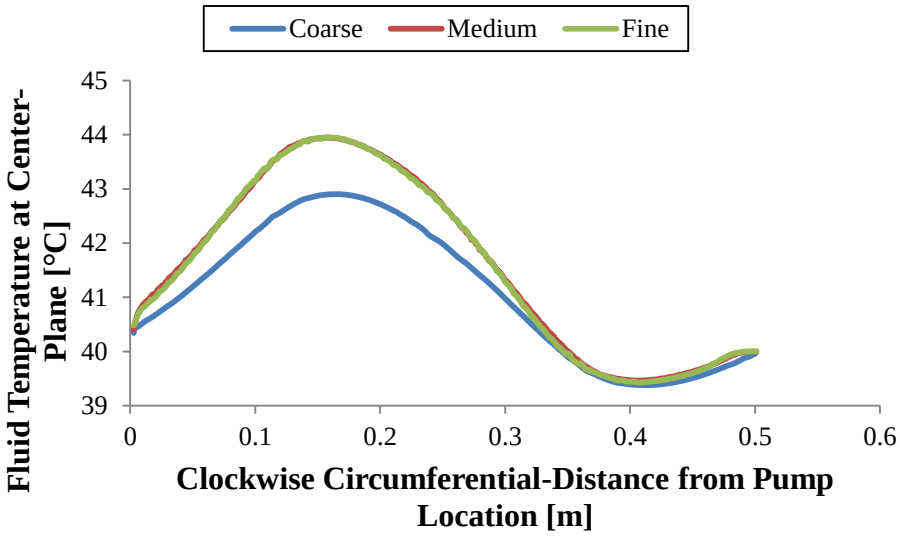

Figure 5.3: Grid-Independent Solution

To save on computational costs and to ensure the validity of the grid-independent solution, the results in Figure 5.3 illustrate the fluid temperature variance between three different mesh scenarios through the origin of the cross-sectional area of PFLA across its circumferential diameter. The Coarse mesh uses 695,382 hexahedral cells, the Medium mesh uses 1,458,485 hexahedral cells, and the Fine mesh uses 4,103,492 hexahedral cells. It is evident that the solution using the Medium mesh captures the thermal gradient in agreement with the Fine mesh at much lower computational cost. Therefore, the grid-independent mesh has been set up with 1,458,485 total cells, wherein 458,550 are fluid cells, and 999,935 are solid cells (461,652 fluid cells contacting solids) and is depicted below.

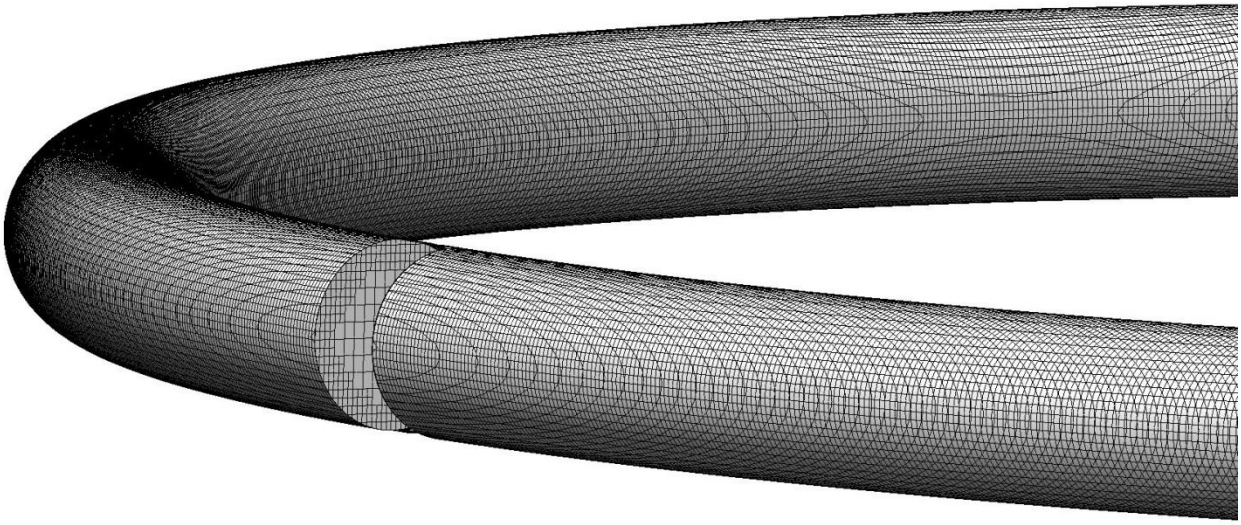

Figure 5.4: Fluid Volume Mesh (Medium – Grid Independent Solution)

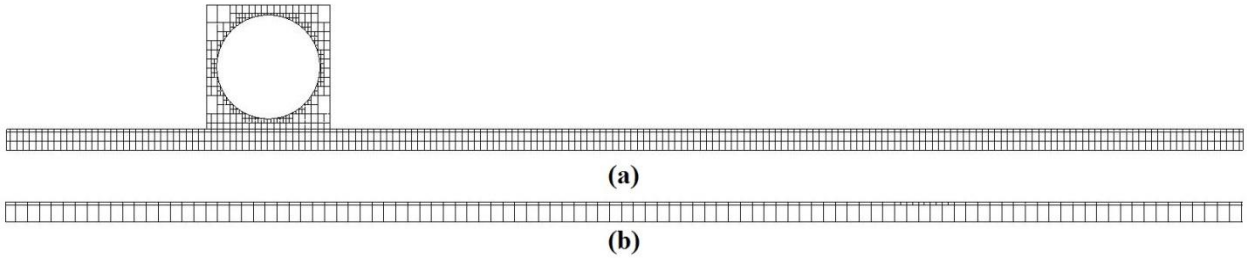

Figure 5.5: Solid Mesh cross-section; (a) PCB, (b) Satellite Structure

The mesh generated for the CFD model can be seen to have a high density at the outer edges of the fluid volume as seen in Figure 5.4 where there is a high thermal interaction between the copper tubing and the fluid. Furthermore, the higher density in that region allows for the wall boundary conditions to be captured. In Figure 5.5(a) the uniform cross-sectional mesh for the PCB is illustrated as well as that of the solid copper tube wherein it can be seen that the region near the flow interaction is again designed with high mesh density. Lastly, Figure 5.5(b) illustrates the cross-sectional mesh at the solid boundary of the satellite body.

For simplification of the CFD model (and to save on computational costs), the simulated loop is modeled without the TCS-M400S pump. However, the inlet and exit boundary conditions in the CFD model are chosen so as to reflect the real operational performance of the pump. The pump

characteristics have been determined through experimental testing, the volumetric mass flow rate of the fluid at 12V input is found to be ~1750ml/min, and the corresponding output pressure as defined in the pump datasheet is ~5.5psi. The resulting fluid flow is laminar and fully developed as it enters the loop. This assumption is validated by the pump design as the flow that exits the pump outlet first travels through an extended output pipe before entering the PFLA loop.

The material of the PFLA is selected as copper due to its high thermal conductivity. The fluid has been selected as ethylene glycol as it has the same consistency and density as water which makes it ideal for the pump (TCS-M400S) while ensuring operational temperature ranges in the space environment. The PCB has been selected as a standard FR4 4-layer board, and the structure of the satellite has been selected as Al 6061-T6.

5.4.1 PCB Thermal Management

For the first case considered in this section, the PFLA is positioned inside a satellite with 48% of its planar surface in direct contact with one face of the PCB; 48% of its planar surface in contact with the structure of the satellite and the remaining 4% is not touching the PCB or the satellite structure. The points of contact are solely from one planar side of the PFLA as depicted in Figure 5.6. The average thermal power output of the PCB is selected a 5W and is in agreement with the energy output from subsystems such as the communications and command and data handling for nanosatellite [87]. The space environment is set to 60°C, and the initial fluid temperature is 40°C. Two scenarios are studied in this section. The first considers a stabilized satellite where no fluid flow is present, and therefore only conduction effects exist, while the latter considers convection effects due to the thermal energy transport caused by the fluid rotation during the operation of the pump. To simulate the effects of convection using the pump, the inlet of the PFLA is selected as a mass flow rate based on the pump characteristics presented in Table 2.1, and the outlet is selected as a static pressure and is set to 5.5 psi based on the pump datasheet. However, to simulate conduction, the inlet is also selected as a static pressure at 5.5 psi.

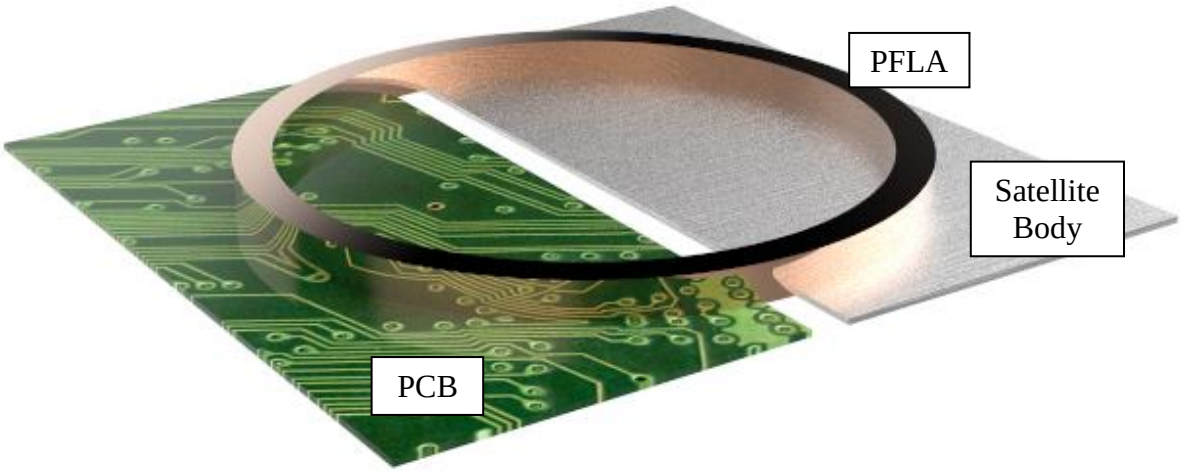

Figure 5.6: Thermal Contact Point of PFLA with PCB and Body

In the next two cases considered herein, the thermal energy transport enters and exits from only one side of the PFLA while its opposing face is open to the internal space environment of the satellite and is assumed to be isolated from external thermal radiation.

5.4.1.1 Conduction

The lack of fluid flow in the case herein eliminates convection, and only conduction effects become apparent. The heat emitted from the PCB is carried through the copper walls of the PFLA solely through conduction and then dissipated into the stationary fluid. The effects from the lack of fluid motion on thermal management capabilities of the PFLA are presented herein.

By examining the steady-state surface thermal gradient of the PCB and colder satellite structure illustrated below, it is evident that the temperature gradient without fluid motion is symmetric about the horizontal axis. Therein, the maximum temperature at the contact surface between the PFLA copper tube and the PCB is 62.84°C. It is also clear that the 5W generated from the PCB increases its surface temperature to a maximum 70.85°C at the center. Furthermore, the PCB temperature at the center of the structure is reduced radially outward as it approaches the inner contact edge of the PFLA as shown in Figure 5.7. The position at which the PFLA contacts the PCB is cooler than the PCB itself and its temperature decreases as it approaches the cooler satellite structure. A light temperature gradient is introduced into the cooler satellite body as the

temperature of the fluid heats up due to the thermal conduction between the copper and the fluid. This phenomenon is well represented in Figure 5.8 where it can be seen that the temperature of the fluid above the satellite body is ~57°C and reduces to its saturated 54.75°C at the opposing end of the horizontal axis. By examination of Figure 5.8 it is made clear that the fluid experiences an increase of 22.84°C at the location of maximum heat absorption.

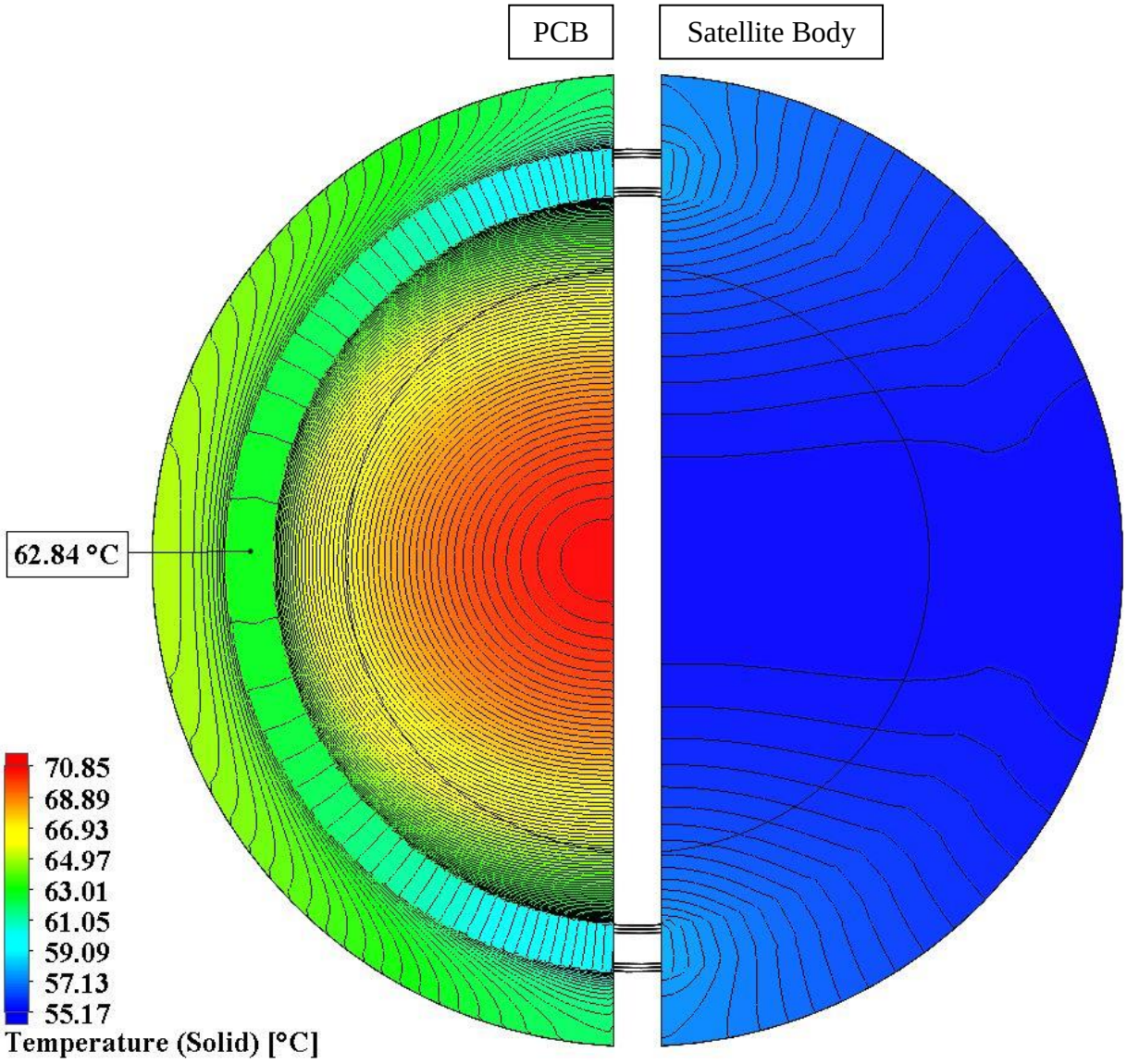

Figure 5.7: PCB Thermal Gradient with Conduction

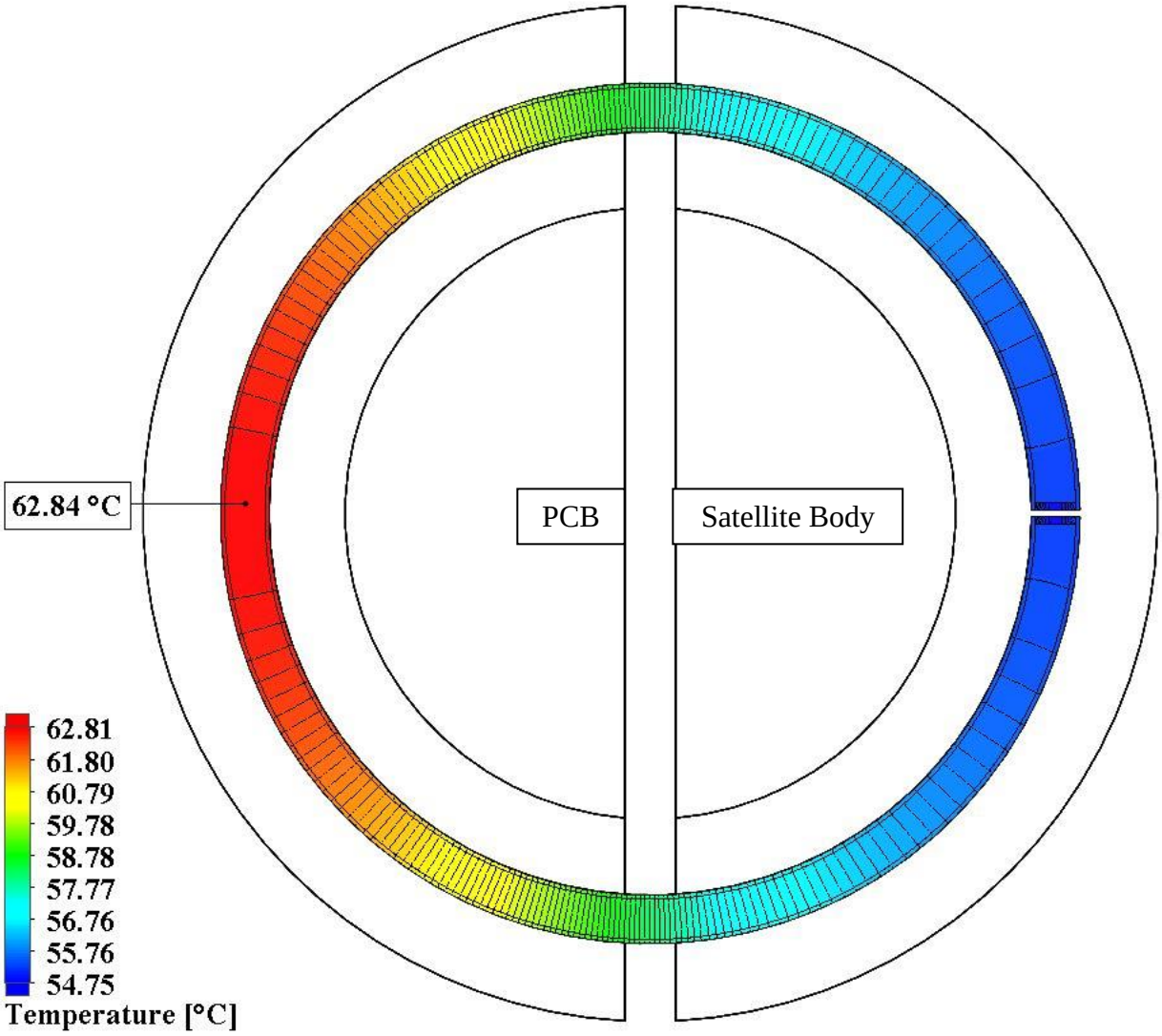

Figure 5.8: Thermal Dissipation inside Wall and Fluid @ Loop Center-Plane

Some portion of the heat has been transferred to the fluid as suggested by the increase in fluid temperature near the warmer region of the PCB. However in order to understand how effective the fluid has been to reduce the temperature of the PCB the following figures examine the heat flux between the PCB and the PFLA copper tube. Therein, it can be seen that the temperature of the fluid (Figure 5.9) is warmer near the surface of the PCB and decreases vertically as it approaches the top side of the tube cross-section. However, the temperature decrease is only 0.06°C from 62.84°C at its closest contact point to the PCB. This is due to the small cross-sectional diameter of the PFLA. At only 7.94mm in diameter, the vertical temperature gradient

cannot be significant without fluid motion. By examination of Figure 5.10 it is also evident that copper tube has also reached a temperature of ~ 63°C. This saturation of the thermal energy between the fluid and the tube limits the thermal cooling capability of the PFLA. It can be seen from the heat flux in the figures below, that the copper tube absorbs the heat generated from the PCB and through conduction heats up the motionless fluid.

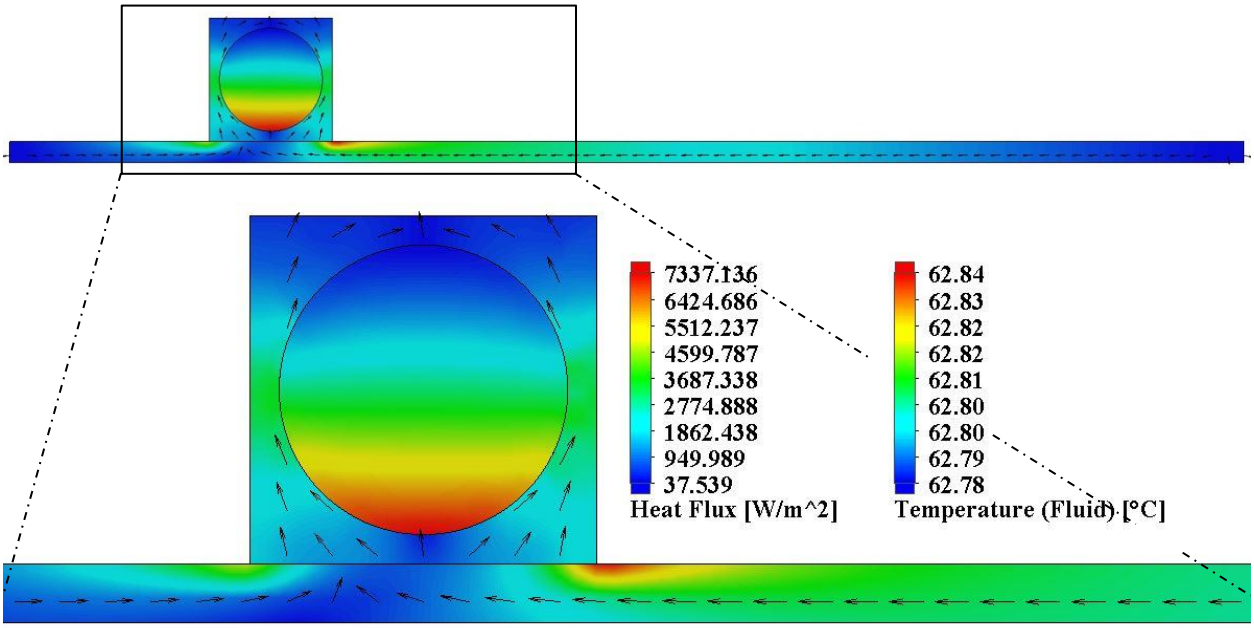

Figure 5.9: Fluid Thermal Gradient & Wall Heat Flux @ cross-section of 62.84°C

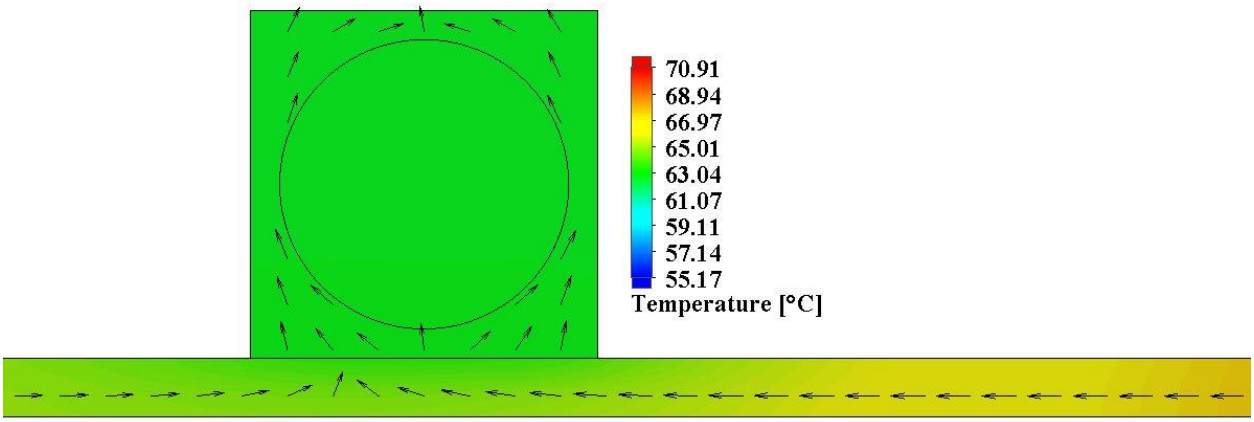

Figure 5.10: Fluid-Wall Thermal Energy Transfer @ cross-section of 62.84°C

Figure 5.11: Heat Flux of Satellite Structure@ cross-section of 62.84°C

From the perspective of the satellite structure, Figure 5.11 shows that without fluid motion, very little heat flux is generated at the cooler satellite aluminum body; there is approximately 0.44W of thermal energy transferred into the cooler body.

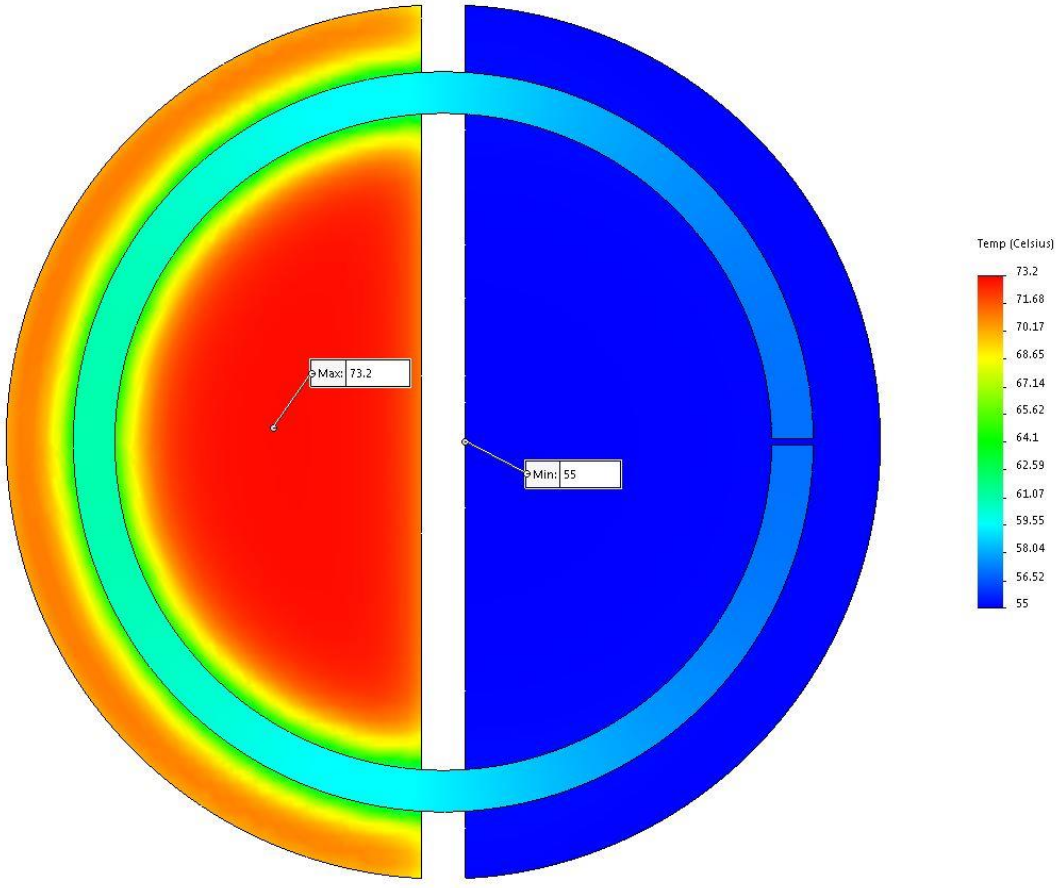

Figure 5.12: Thermal Analysis without the presence of Fluid

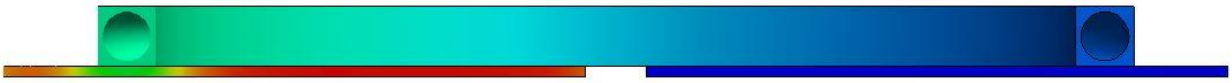

Figure 5.13: Thermal Analysis without Fluid (horizontal cross-section)

By examining the temperature of the solid copper wall in Figure 5.8, and considering that the temperature of the fluid is saturated by the temperature of the solid copper as depicted in Figure 5.10, it is made evident that with the lack of fluid motion the transport of thermal energy is primarily through the copper and not the fluid. Therefore, the fluid does not play a significant role in cooling down PCB. To validate this theory, a thermal analysis was carried out without the fluid medium. The results are presented in Figure 5.13 and are in close agreement with those presented in Figure 5.7. By examining the results of Figure 5.13, the temperature saturation of the copper tube is clearly represented wherein the temperature gradients are reprehensive of those presented in Figure 5.10 with the presence of fluid. Therefore, it can be concluded that if the fluid inside the PFLA is not rotating, the thermal dissipation of heat is dominant through conduction of the copper body of the PFLA and the fluid does not play a vital role in reducing the temperature of the PCB.

The next case examines the thermal management capabilities of the PFLA while considering convection as caused by the rotation of the fluid.

5.4.1.2 Convection

In this section, the study examines the ability of the PFLA for the transport of thermal heat energy from one area to another. The study examines the pump operation at 12V that generates a clockwise volumetric flow rate of 2.917×10^{-5} m^3/s. The initial temperature conditions and pump output pressure are set as previously indicated in this chapter.

By initial examination of the thermal gradient illustrated in Figure 5.14 it is immediately evident that the maximum temperature that was experienced without fluid rotation on the surface of the PCB is decreased by 18.17°C in the presence of fluid motion. It is further illustrated that the peak temperature at the point of contact of the PCB and copper tube is reduced from 62.84°C to 44.10°C.

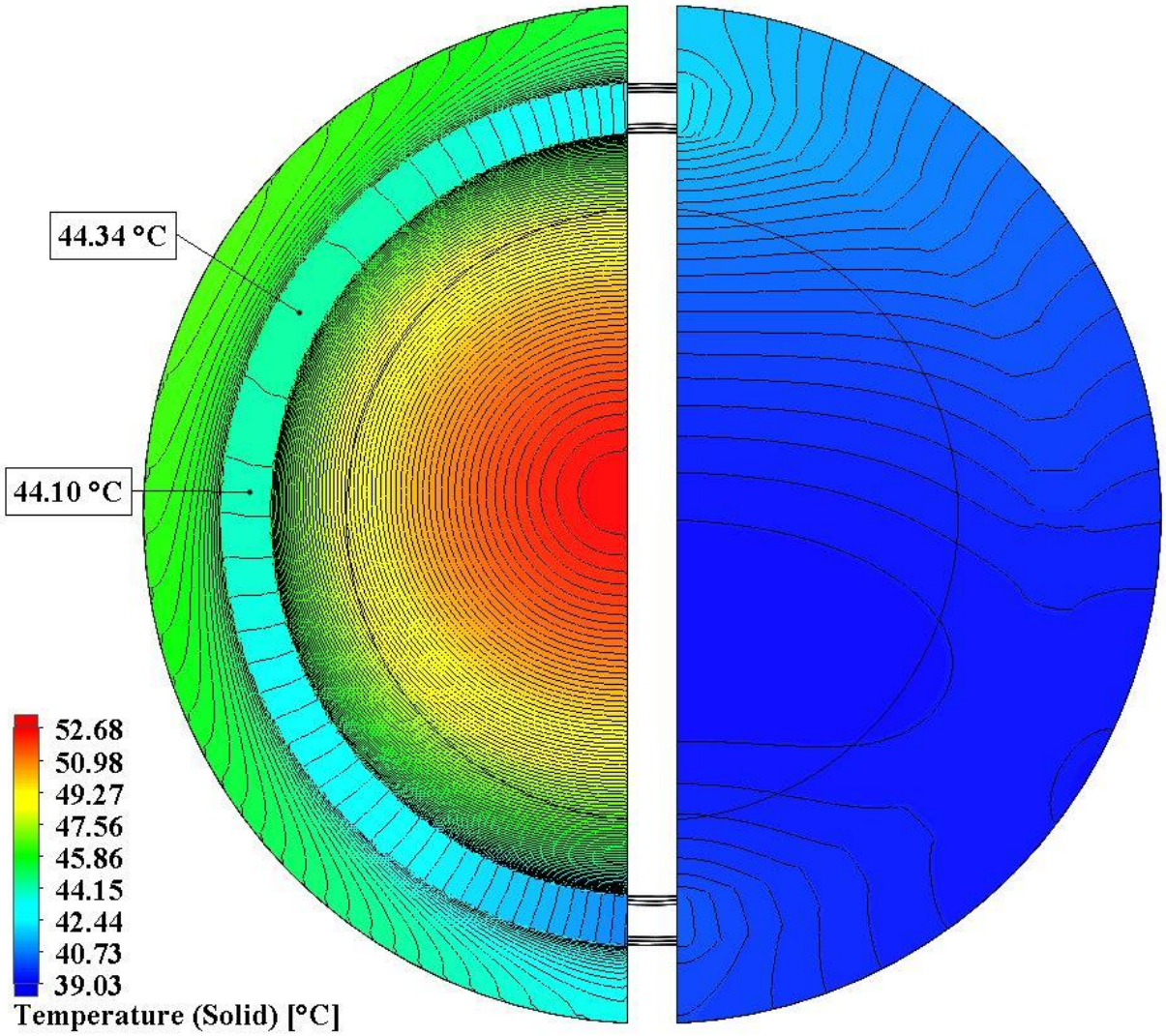

Figure 5.14: PCB Thermal Gradient with Fluid Convection

At the surface of contact between the PFLA and the PCB, a clockwise twist-like effect of the temperature gradient is visible in Figure 5.14 and is directly attributed to the fluid rotation as can be seen in Figure 5.15. The temperature gradient of the PCB and satellite body suggest that as the fluid is ejected from the pump, it enters a cool region of flow and pushes the cooler fluid into the warm region of the loop that is in contact with the PCB. It can be seen at the surface of the PCB, that because of the fluid rotation, the hottest position along the base of the PFLA is moved ~ 30° clockwise of the horizontal axis that saw the highest heat in the case considered previously without fluid rotation. The thermal transport of the fluid is better depicted in Figure 5.15 where it

can be seen that the fluid is bringing cooler temperatures into the PCB and absorbing the heat into the cooler satellite body. Furthermore, unlike through pure conduction that saturated the temperature of the fluid and the copper body, with convection is can be seen that the temperature at the surface of the copper tube in contact with the PCB is 44.34°C, yet the fluid at the same location is 43.49°C. This means that the fluid has been able to absorb greater thermal energy and transport it away from the heat source through the use of convection.

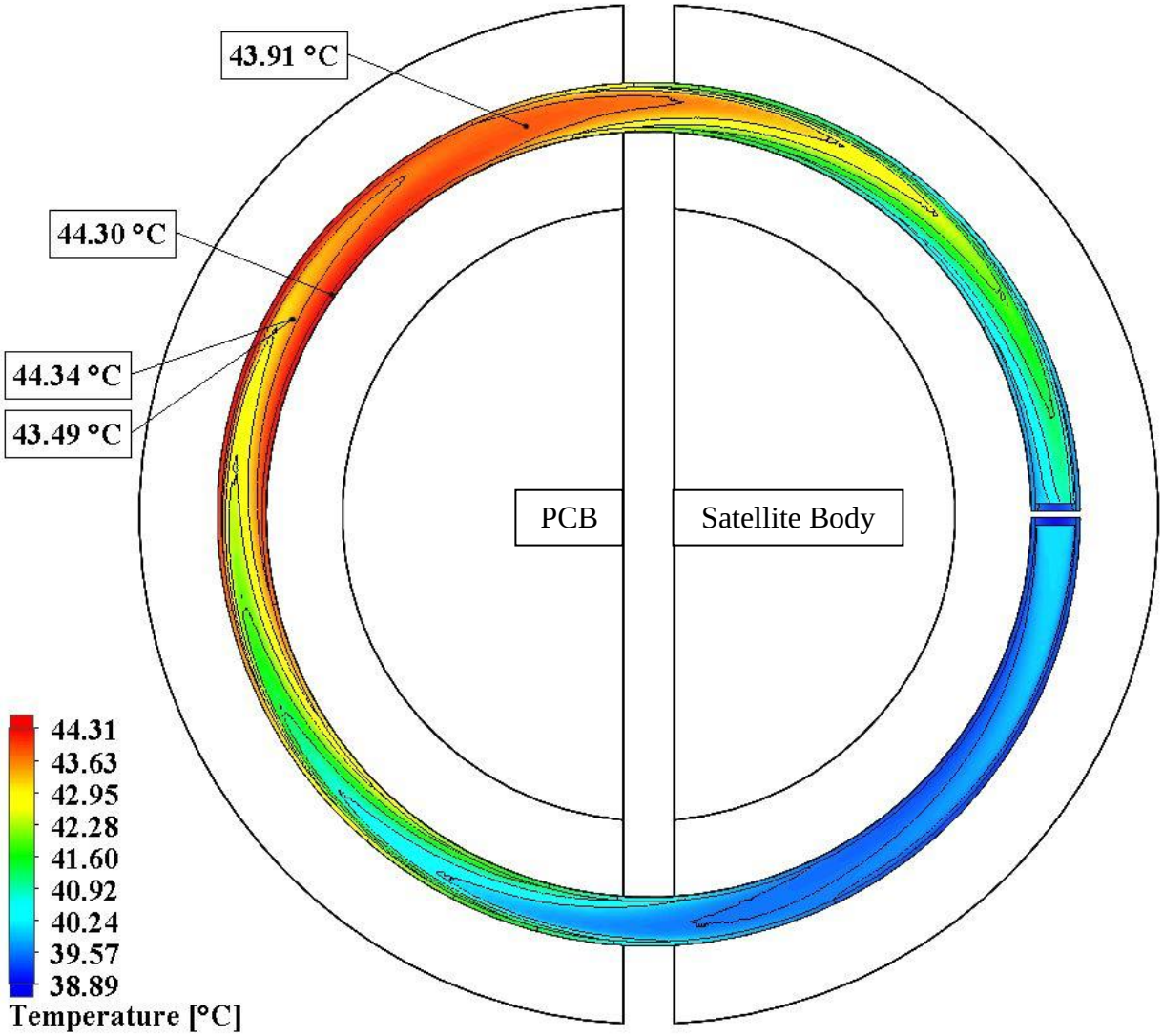

Figure 5.15: Thermal Dissipation inside Wall and Fluid @ Loop Center-Plane

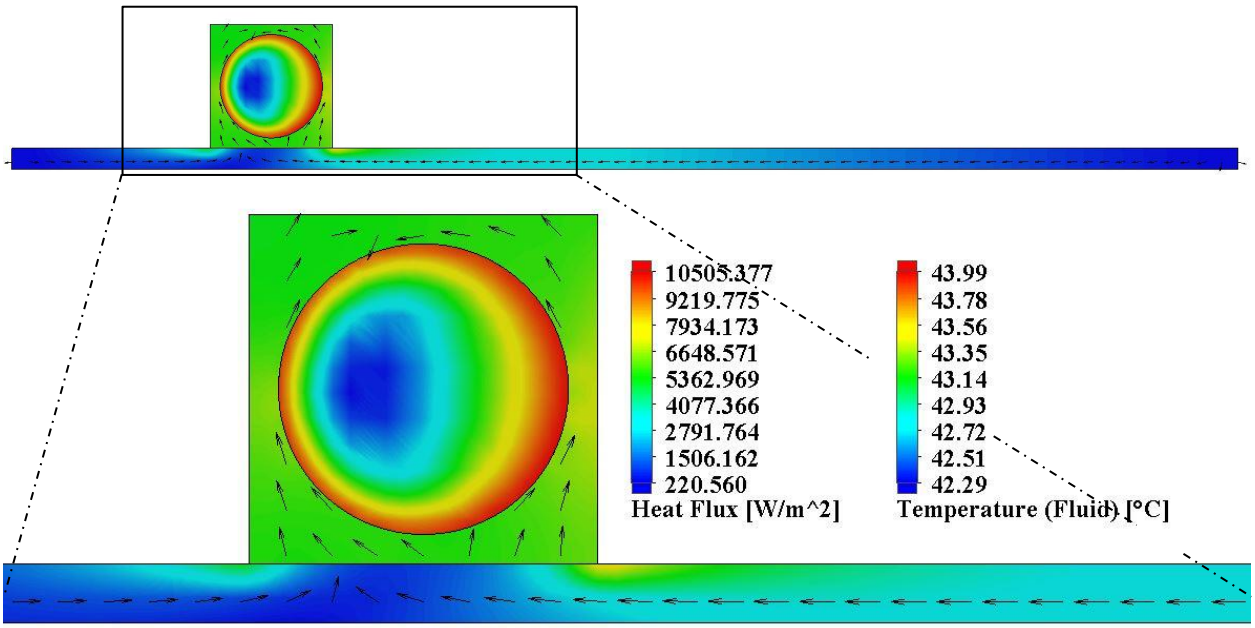

Figure 5.16: Fluid Thermal Gradient and Wall Heat Flux @ cross-section 44.1°C

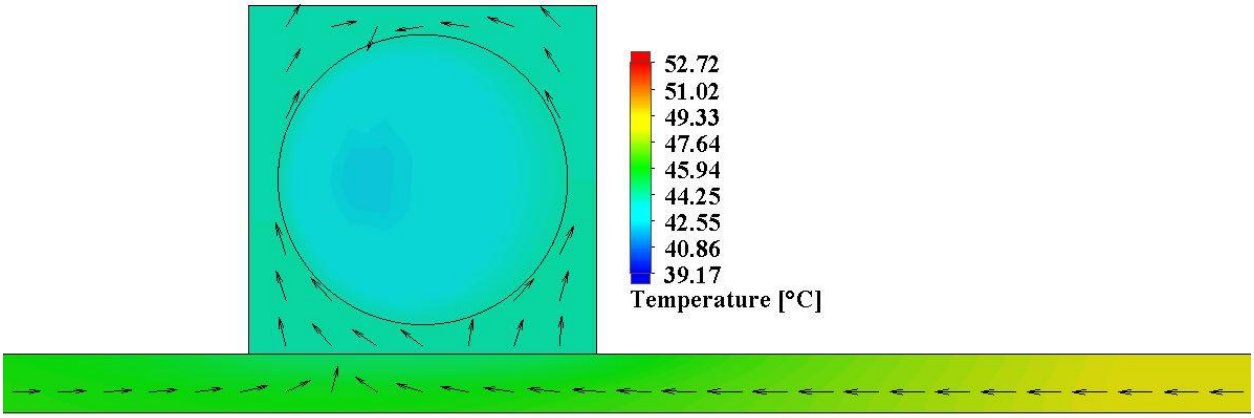

Figure 5.17: Fluid-Wall Thermal Energy Transfer @ cross-section of 44.1°C

It is also evident that higher thermal heat flux is generated at the horizontal plane of the PFLA as is demonstrated in Figure 5.16. Additionally, it can be seen that unlike the fluid thermal gradient that increased only 0.06°C vertically about the cross-section of the fluid reservoir in Figure 5.9, the temperature gradient is more prominent with flow as is seen in Figure 5.16. Therein, the fluid experiences a thermal gradient of 1.7°C, a factor of ~ 28 times that of what was examined

without fluid rotation. It is also evident from Figure 5.17 that the fluid is not saturated by the solid copper tube. A clear indication is visible of a cooler flow passing through the center of the cross-section that absorbs heat from the copper tube and therefore has a greater cooling effect on the PCB and limits the temperature of the copper from saturating the fluid.

Figure 5.18: Heat Flux of Satellite Structure@ cross-section of 44.1°C

With convection, the satellite body absorbs greater thermal energy that is transported from the PCB, and the heat flux is presented in Figure 5.18. Compared to Figure 5.11 where only 0.44W of energy was transported to the satellite body, through the advantage of convection ~ 8W of energy is absorbed by the satellite body in the case considered herein.

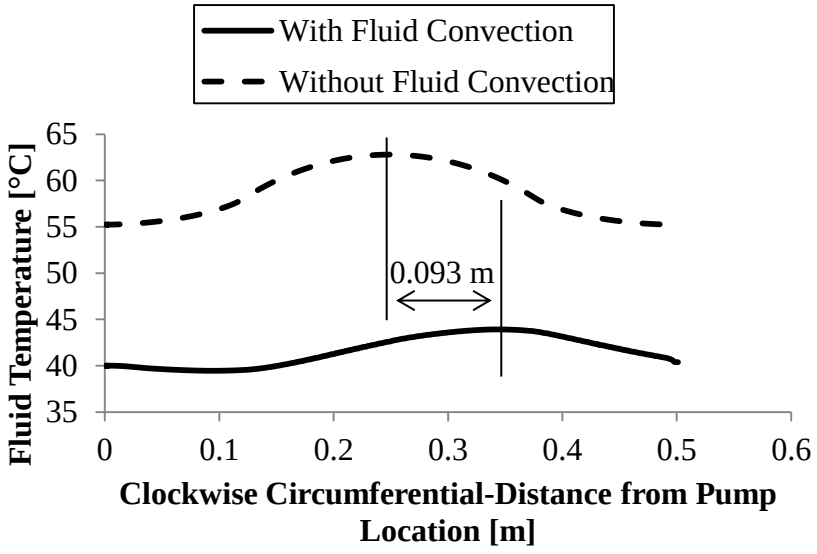

Figure 5.19: Fluid Thermal-Transport at Circumferential Mid-Plane of PFLA

By examining Figure 5.19, it is clear that the peak temperature is transported 93 mm circumferentially closer to the cooler satellite body with the presence of fluid convection.

The fluid transport capability for regulating the thermal heat of a PCB onboard a satellite has been successfully demonstrated in this section. It is established that the PFLA can be used to thermally cool a PCB or subsystem through the effects of conduction and convection wherein the latter presents elevated thermal cooling capabilities due to the ability of the fluid to transport the thermal energy away from the source and bring in cooler fluid.

The next case examines the PFLA for the purpose of isolating the internal subsystems from the effects of the external environment.

5.4.2 Thermal Isolation from External Environment

In this section the PFLA is sandwiched between the satellite body and the constituent PCB is mounted on the opposing face of the PFLA in order to eliminate its direct contact with the external environment as shown below.

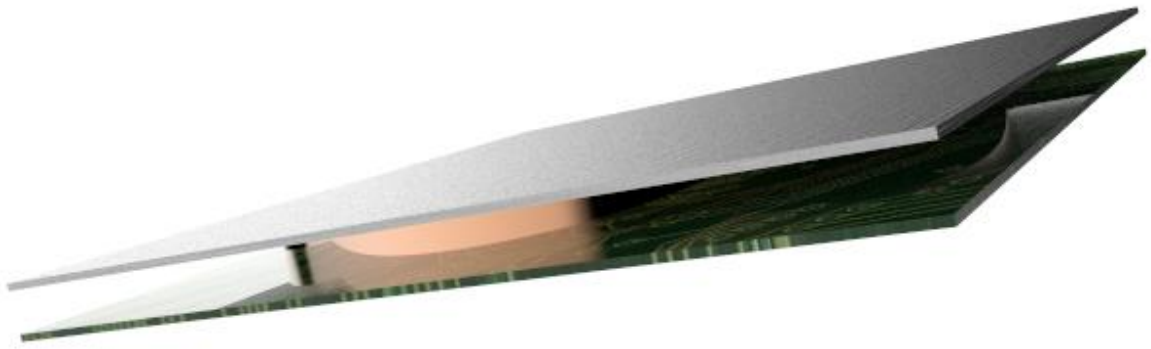

Figure 5.20: Thermal Isolation of PCB using PFLA

The steady-state results are presented herein and examine the point in time when the fluid temperature has been saturated inside the PFLA. The symmetry of the temperature gradient illustrated in Figure 5.21 shows that the maximum temperature reached by the PCB is 63.53°C on the surface of the board. The maximum temperature herein is less than the 70.85°C that was reached in the geometry proposed in Section 5.4.1.1. As seen therein, the saturation of the fluid temperature causes heat transfer to occur dominantly through the copper tube of the PFLA.

Similarly, in this section, the saturation of the fluid results in thermal dissipation to occur primarily through the copper tube.

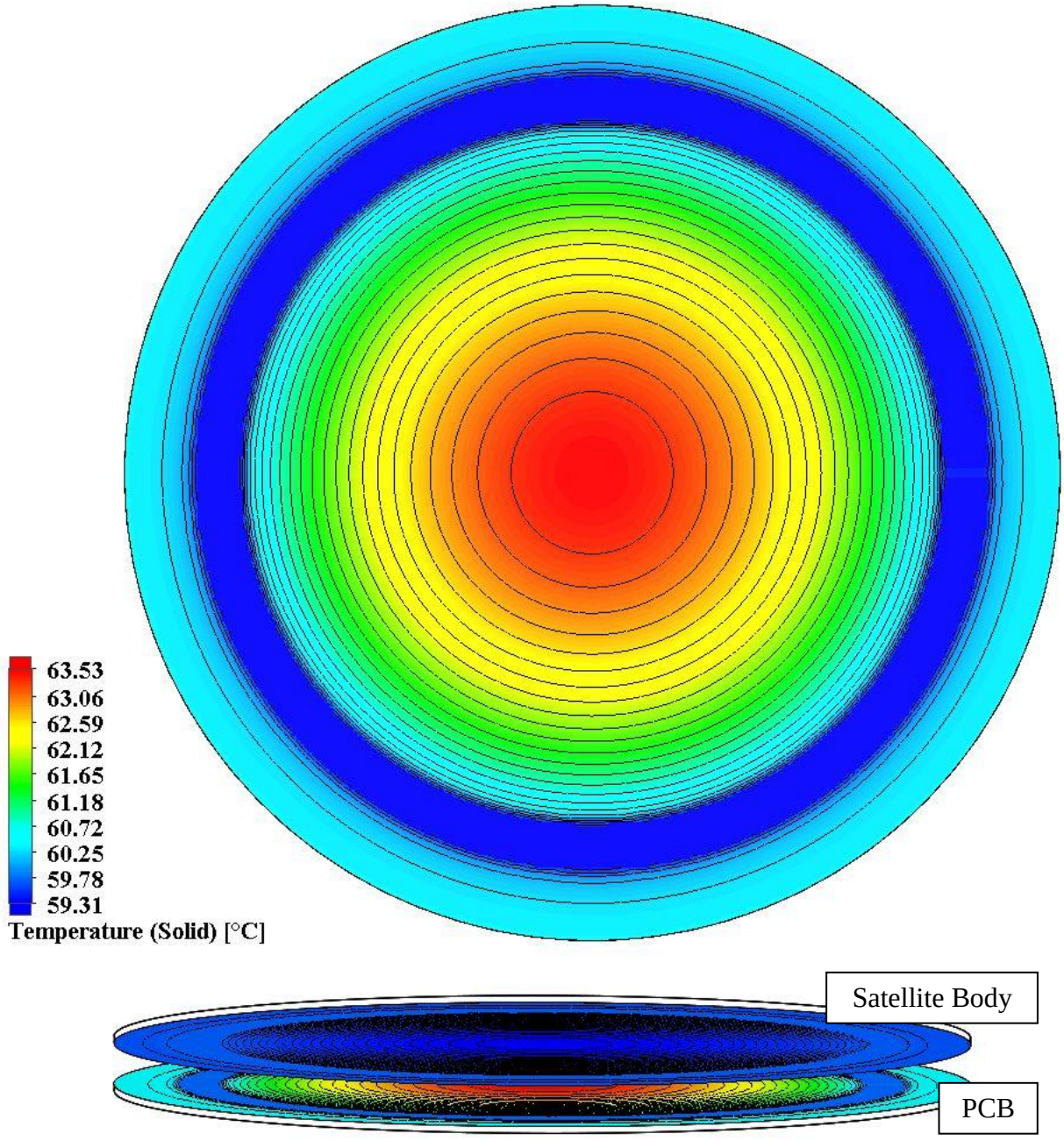

Figure 5.21: Thermal Gradient of PCB and Satellite Structure Surface

The effects of fluid flow through convection do not carry any added benefits in this section since the entire fluid is saturated at the same temperature as shown in Figure 5.22. The thermal heat transfer travels from the warmer PCB through the copper and is dissipated into the satellite structure as illustrated by the direction of the heat flux arrows in the image below. Furthermore, due to lack of fluid motion, the temperature gradient of the fluid is again seen to decrease vertically above the PCB. Although the gradient is not significant at 0.04°C (similar to 0.06°C as was seen before in conduction), the increase of contact surface area of the copper with the cooler satellite body significantly increases the temperature gradient of the PCB and transfers greater thermal energy to the satellite body thereby decreasing the temperature of the PCB.

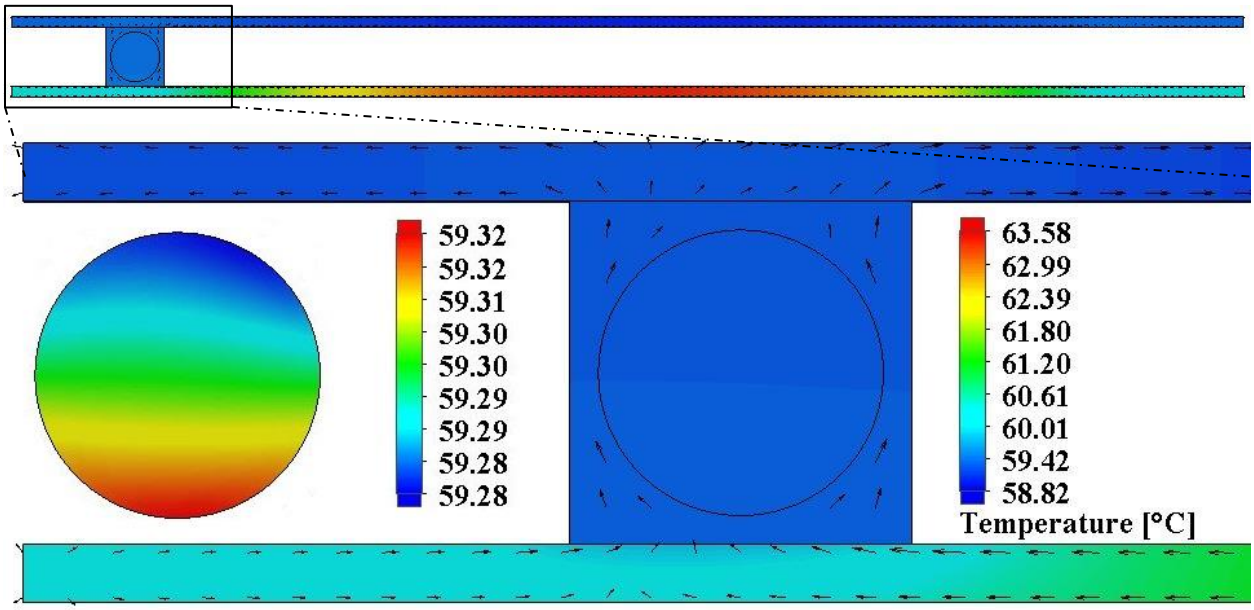

Figure 5.22: Thermal Energy Transport from PCB to Satellite Structure

In this section, the application of the PFLA for thermal isolation of the PCB board from the satellite structure has been illustrated, and the results indicated that heat transfer occurs through conduction between the PCB, copper tubing, and the satellite structure due to the temperature saturation of the fluid. The results indicated that with the greater surface area of contact, the PCB temperature is able to maintain operational temperatures below the critical temperature of 70°C (temperature subjected to electronics during hardware testing). In the next case, the PFLA is examined for the cooling of single critical components onboard the satellite.

5.4.3 MEMS Thermal Management

In this section, the PFLA is demonstrated for its thermal cooling capabilities of critical components on board a satellite. For instance, the power amplifier of the communications subsystem produces high power output and therefore generates heat that could increase the temperature of the component above its maximum operating temperature when subjected to elevated environmental temperatures.

Herein the PFLA is positioned such one of its surfaces is in contact with the satellite body, and the heat generating unit is positioned so as to contact the circumferential surface of the PFLA as illustrated below. The PCB is not in contact with the satellite surface in order to isolate it from conduction through the satellite body and eliminate any environmental effects.

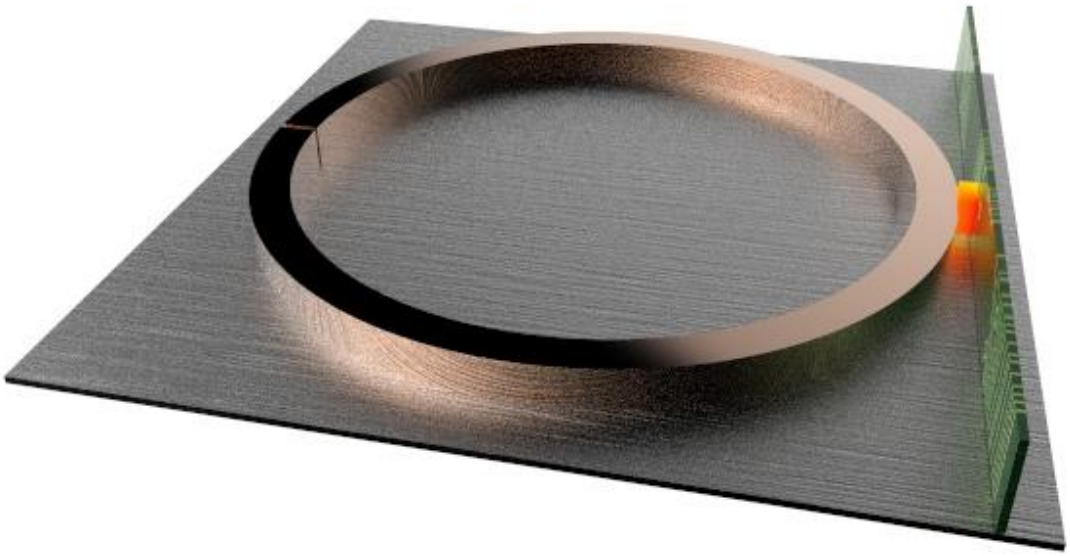

Figure 5.23: Thermal Dissipation from Critical Component

With reference to the design of the PFLA, since the contact between the PFLA and the power amplifier creates a thin edge, the surface of the PFLA tube is cut horizontally to sit on the component and maximize its contact surface area from a single edge to an area of 71.22436 mm^2 as shown in Figure 5.24. Since thermal conduction is dependent of contact surface area, the increase in contact area allows for higher thermal heat conduction to occur at that face and therefore thermally cool the power amplifier more effectively.

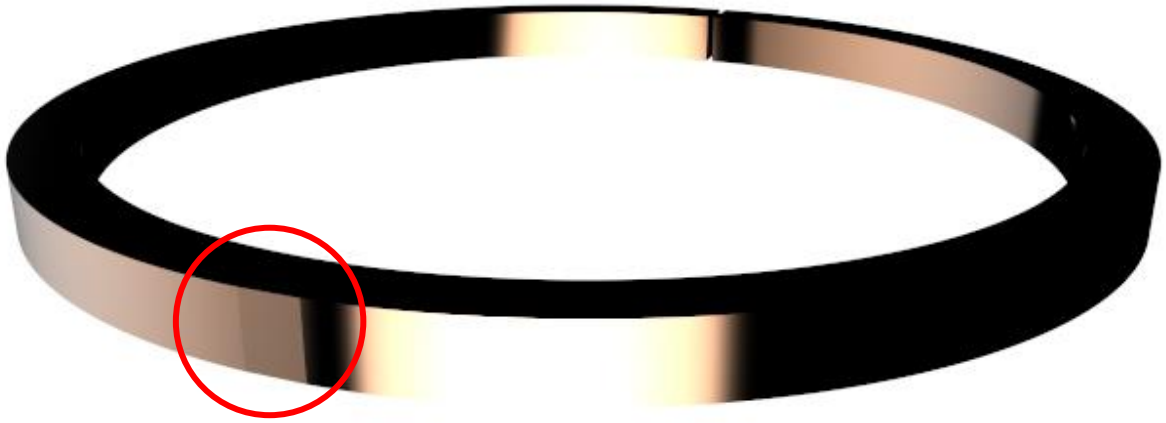

Figure 5.24: Contact Surface with Power Amplifier

The power generation of the amplifier is set to 3W, and the initial satellite body is 60°C. Since the PFLA is in direct contact with the satellite surface, over time, the fluid temperature is saturated by the temperature of the satellite due to thermal conduction and is the case considered herein. While flow rotation, the thermal energy transport of the amplifier is illustrated in Figure 5.25:

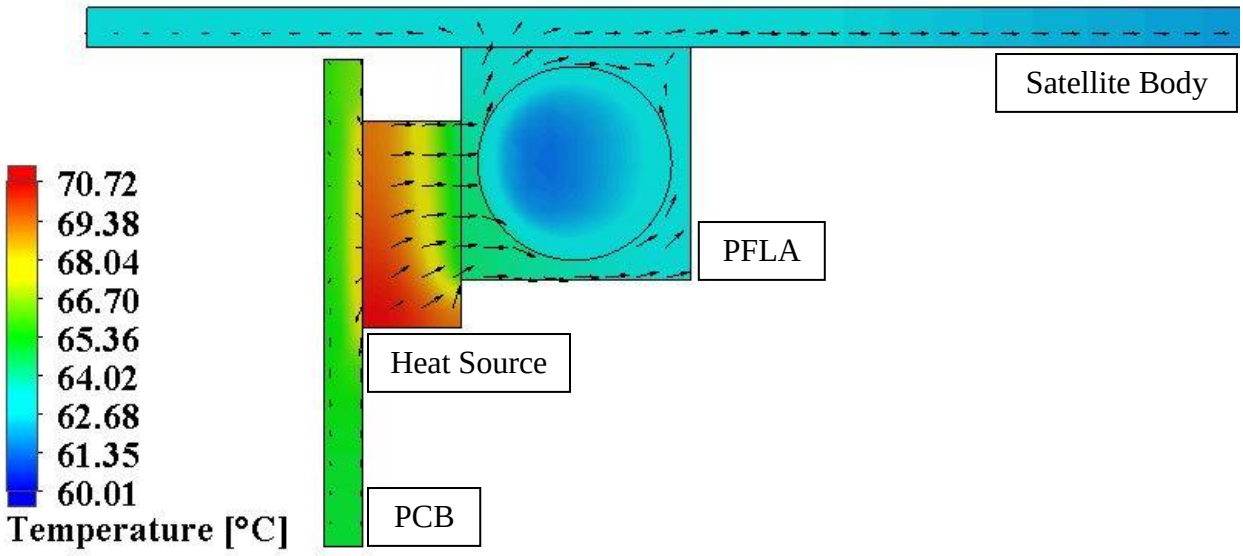

Figure 5.25: Thermal Heat Transfer from Power Amplifier

It can be seen that the thermal energy is transferred from the power amplifier to the copper tubing of the PFLA by conduction and then dissipated into the satellite aluminum body. The thickness of the component has been designed to 4mm; typical MEMS systems can have thicknesses of less than 2mm (therein the effects would be more prominent). By examining the power amplifier, it is clear that the temperature gradient caused by the PFLA is able to penetrate through the entire depth of the amplifier. As the thickness of the component increases, the depth of heat dissipation into the volume of the component decreases. Therefore, for thinner components such as MEMS microcontrollers, the PFLA would be able to reduce the overall temperature of the volume by approximately 5°C with only a small point of contact on the surface of the component. By maximizing the contact area, increased thermal energy can be absorbed from the heat source. It is further examined that a cooler flow exists in the core of the tube as opposed to the outer edges that are in contact with the copper thereby suggesting that the fluid is not saturated by the increase in thermal energy from the amplifier.

By examining the heat dissipated from the copper tube into the moving fluid, Figure 5.26 demonstrates that the fluid is transporting the temperature in the clockwise direction from the heated element as per the direction of the flow. Regions of the fluid that are farther from the heated element are approximately 60°C (as expected by the saturation of the external satellite body), and regions closer to the heated element have increased to ~62°C - 64°C. A similar notion is depicted herein as was seen in the convection case presented in Section 5.4.1.2 where the cooler fluid is able to transport the warmer fluid away from the heat source and is verified by the cooler inner core as aforementioned.

Similar to before, the temperature of the cooler satellite body presents a twist-like thermal gradient due to the rotation of the fluid transporting heat across the circumference of the PFLA. Moreover, it is evident that on the surface of the satellite closest to where the heat has been absorbed by the PFLA, the thermal heat dissipation from the power amplifier has been absorbed and transferred into the satellite body through conduction hence increasing its temperature in that region to ~65.5°C as depicted in Figure 5.27. It can also be seen that the heated temperature absorbed into the satellite solid body in Figure 5.27 is skewed clockwise. This confirms the effects of convection due to the fluid rotation; the effects are presented by the green region that is

shifted up from the center of the plate – results that are in agreement with the flow rotation depicted below by the similar green region. Thus, the thermal energy is indeed transported farther from the heat source due to the effects of convection. Without convection, the thermal gradient would be symmetric about the horizontal axis, and the lack of flowing fluid would not transport the heat away from the source thus resulting in less energy being absorbed from the power amplifier.

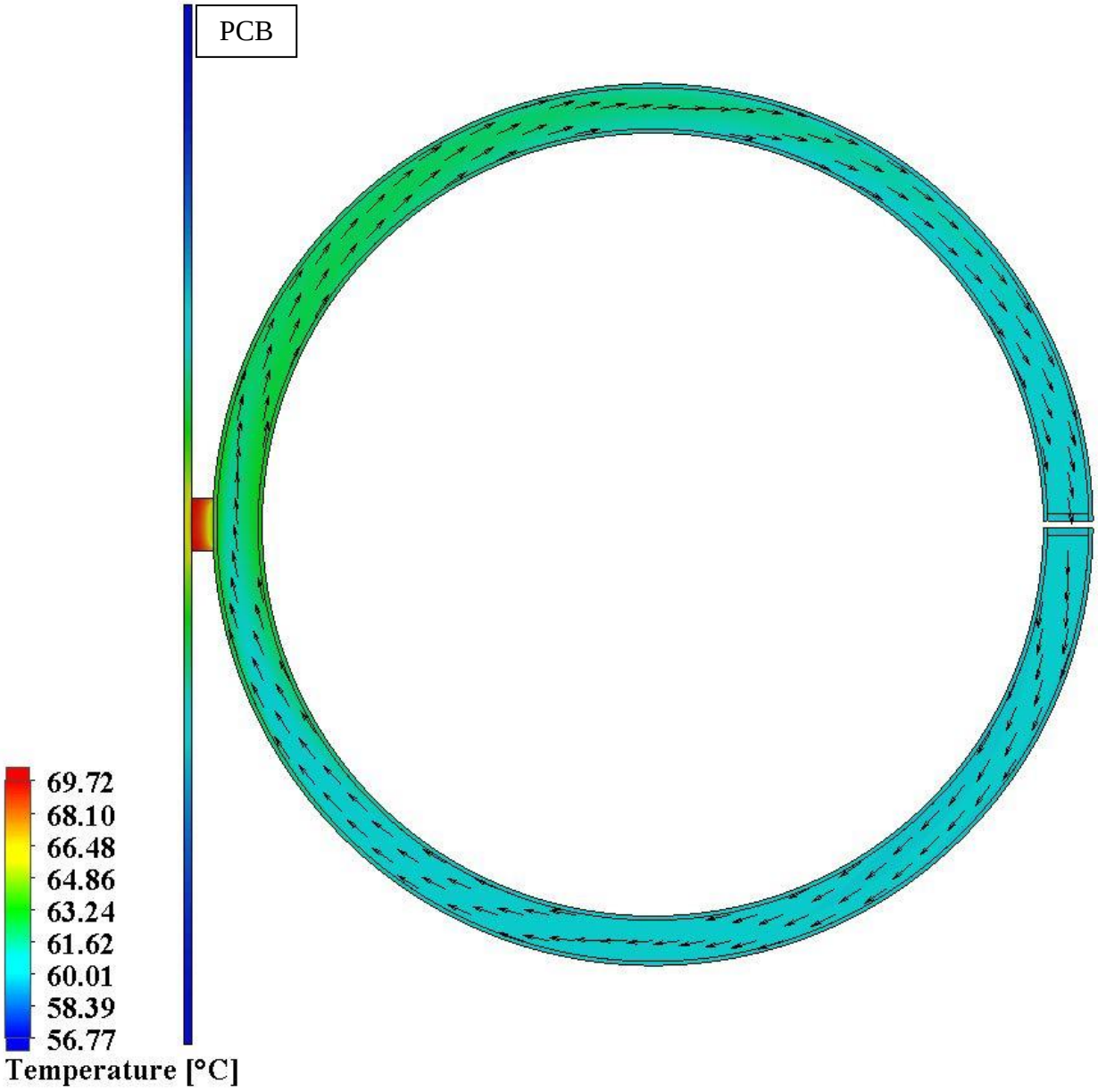

Figure 5.26: Temperature Gradient of Fluid and Solid at Mid-Plane of PFLA

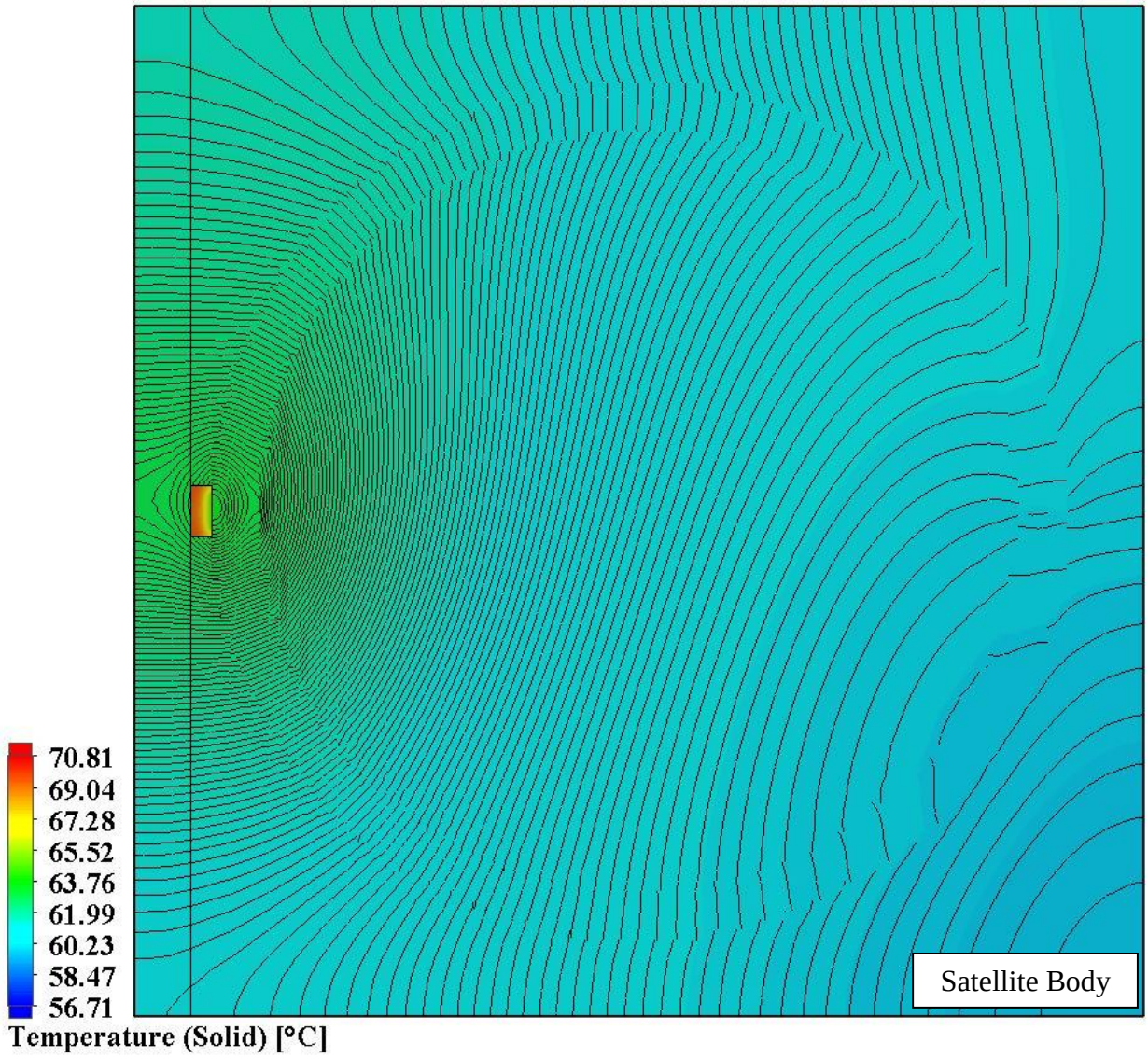

Figure 5.27: Solid Surface Temperature Gradient

In this section, the application of the PFLA was examined for the thermal management of a single critical components onboard the satellite and the results indicated that in the presented configuration, thin (less than 4mm) MEMS components can be thermal cooled using the external environment through flow rotation that induces convection. At lower environmental temperatures, such as when the satellite is on the dark side of the Earth or, when the satellite face equipped with the PFLA is not facing the sun, greater thermal cooling can be achieved using

the PFLA. This is due to the lower saturated temperature of the fluid that can effectively transport greater heat away from the component and bring in cooler fluid to the area.

5.5 Conclusions

In this chapter, the thermal management capabilities of the PFLA are studied to determine the feasibility of thermal conduction and convection for maintaining operational temperatures of electronic components and subsystems onboard a satellite. Three configurations of the PFLA have been studied, and it has been determined that in the presence of fluid rotation, the convective effects that are introduced are able to provide thermal transport capabilities of up to ~ 20°C.

While the temperature of the fluid inside the PFLA is below the temperature of the electronics, the effects of thermal convection will aid to maintain the thermal operating range of the electronics to which the PFLA is attached. Furthermore, the PFLA can be used a device to isolate the PCB board from the surface of the satellite body in order to provide a method of thermal management while using the environment to its advantage. The thermal energy transport of the PFLA has been determined to be inversely proportional to the temperature of the satellite body to which it is attached. Therefore, a satellite requiring high thermal heat dissipation may turn its face with the PFLA attached away from the sun to cool down the fluid through conduction of the cooling satellite body, and simultaneously use the cooler fluid to perform thermal transport of heated elements inside the satellite.

In the absence of fluid rotation, the mode of energy transport by conduction has been recognized as dominantly through the copper tube and not the fluid. The lack of fluid rotation inside the PFLA causes temperature saturation of the fluid and therefore renders the fluid ineffective. Although through conduction the temperature of the heated element such as a PCB board can be reduced by ~7°C in the regions neighboring the PFLA structure, the presence of convection effects is able to further reduce the temperature by approximately three folds before the temperature of the fluid is saturated.

CHAPTER 6
CONCLUSIONS

THE primary and most advantageous aspects of the PFLA have been overlooked in the literature and are presented in this dissertation from a practical perspective while considering the necessity of simulations to take into consideration the dynamics imposed onto satellites during actuator saturation. PFLA have been introduced as combined attitude and thermal management systems, yet very little examination is carried out in the literature to address their thermal management capabilities. This dissertation provides a completed analysis on the PFLA that examines all its performance aspects including, active and passive attitude stabilization, active attitude rest-to-rest maneuvers, real-time active attitude maneuvers, hybridization of the passive and active method for fault-tolerant control, and provides a comprehensive examination of the thermal management capabilities of the PFLA. Furthermore, the performance limitations of traditional passive stabilization methods are overcome with the design and development of a novel spherical fluid dynamic actuator.

6.1 Summary of Contributions

In this section, a review of the major contributions of this dissertation is presented. The contributions are categorized based on the previous chapters.

6.1.1 Nonlinear Voltage-Driven Control Law and High-Fidelity Actuator Torque Model

Ignoring the actuator dynamics in the control of rigid manipulators can in practice result in performance degradation or loss of system stability [2]. Generally, input control torque does not consider the dynamics of the actuator but only torque limitation of the system. The absence of an actuator model does not appropriately reflect the performance of theoretical control algorithm for practical applications.

A gap exists in the model defining the performance of the PFLA due to the lack of a high-fidelity actuator model that also considers the hardware saturation and applied torque capabilities of the

PFLA. A clear assessment cannot be made against the performance of said actuators and their benefits, or lack thereof if the full actuator dynamics is not considered. This dissertation presents a high-fidelity model of the PFLA in order to examine the system from a practical perspective.

In this study, a control technique is proposed that takes into consideration the problem of actuator saturation from a hardware perspective not considered in the literature. The proposed technique can be applied to any control algorithm for practical implementations. The model adjusts the control output torque from the control algorithm to reflect the hardware performance of real systems wherein the applied torque to the satellite is zero during states of constant angular velocity. Herein, a nonlinear voltage-driven control law is developed that drives the physical motor voltage as opposed to control torque. The controller is applied to a high-fidelity PFLA model to examine the performance of the actuator system for satellite attitude control. The method validates the compatibility of the control algorithm with the PFLA system while demonstrating the application of the PFLA.

6.1.2 Attitude Tracking Maneuvers

Analyses carried out in the literature have not examined the application of the PFLA for attitude tracking maneuvers. This study presents, a first account in the literature wherein fluid is used to perform rest-to-rest and attitude tracking maneuver with consideration of the complete motor and fluid dynamic models of the PFLA. The nonlinear control algorithm used in the literature is modified to control the voltage signal of the actuator directly as opposed to control torque. The performance of the PFLA is examined, and its optimal power configuration is obtained. The study entailed presents a complete and practical examination of the PFLA not found in the literature.

6.1.3 Novel Actuator Design

The control and generation of magnetic fields either through magnetic coils or permanent magnets has allowed for the development of sophisticated spherical devices that offer complete 360° control while eliminating hardware singularity constraints. The spherical electromagnetic actuators are unrealistic for satellite attitude control in their current state due to the complexity of their designs.

Furthermore, the passive attitude stabilization of satellite has been addressed in the literature through the use of environmental forces available in space and through limited number of hardware systems such as magnetorquers and the PFLA system. The existing hardware devices are limited in their ability to generate torques about any arbitrary axis; magnetorquers require being in line with the Earth`s magnetic field, and the PFLA can only stabilize torques if they are subjected directly about the torque axis of the loops.

To address the limitations of existing methods, a novel patent pending [88] actuator developed based on the fluid dynamic principles of the PFLA is proposed. The actuator, termed PFSA, takes advantage of an innovative spherical configuration to provide passive control torques about any arbitrary axis. The single PFSA can replace three PFLA while providing comparable active control performance and superior passive control torques due to its unique design. The foundation of the proposed actuator is set in this dissertation in order to extend the innovation in actuator technologies.

6.1.4 Attitude Stabilization with Novel Actuator

The examination of attitude control while considering sensor failure or the absence of sensor information has become of increased interest in the literature. To address this issue, fault-tolerant and robust control algorithms are proposed to perform parametric estimations of the lack of sensor feedback data. In this study, the fault associated with rate gyro failure is examined through the passive technique of a novel actuator system wherein the fluid angular velocity is used in place of the rate gyro sensor data. The proposed method extends the application of the proposed actuator to act as both an actuator and a sensor for performing simultaneous passive attitude control and determination.

6.1.5 Thermal Management

The combining of subsystems into a single multi-purpose unit is examined in the literature for the combined attitude and thermal management systems. Existing works in the literature examine the methods of magnetofluid dynamics that require high voltages for flow regulation and is currently impractical for its attitude performance capabilities. Through the history of the PFLA, the system has been proposed as a thermal management system but has not been examined for its

thermal transport capabilities. In this study, a first account of the thermal management performance of the PFLA is examined for practical applications. Extensive CFD simulations are carried out, and the practicality of the PFLA as a combined attitude and thermal management subsystem is presented as a first in the literature.

6.2 Future Works

In this section, research topics are introduced that will further extend the research entailed in this dissertation. The topics are intended to progress the advantages of using fluid as a combined attitude and thermal management system for small satellite deep space missions.

6.2.1 Active Attitude Control using PFSA

The foundation of the PFSA system has been set in this thesis, and preliminary research conducted through CFD and numerical simulations proposed the practicality of the system for active and passive attitude control of satellite. A comprehensive mathematical model of the fluid motion inside the cavity of the PFSA needs to be developed in order to examine its performance capabilities for active attitude stabilization and tracking maneuvers and to obtain a mathematical relationship between the applied voltage and axis of rotation; identifying the necessary voltage ratios that generate a specified AOR requires a complex reverse algorithm than what is used in this dissertation.

6.2.2 Transient Analysis for Thermal Simulation

The thermal analysis carried out in this dissertation examines the steady-state response of the PFLA system as a basis to examine the behavior and thermal transport energy of the fluid from the perspective of convection and conduction. The analysis of a transient flow simulation would help to understand the time dependency of the thermal management capability of the PFLA.

6.2.3 Hybrid PFLA for Actuator Saturation

In the literature, the PFLA and PFLA-like systems have been studied as either exclusively active or passive actuators. An examination of the hybridization of both passive and active methods has not been made. A hybrid technique would increase the operational capabilities of the PFLA to

ensure stability without the need for peripheral devices such as magnetorquers for momentum dumping under actuator upper limit torque saturation. This hybrid method would provide a fault-tolerant by design actuator that can perform its own momentum dumping.

6.3 Concluding Remarks

The performance of the PFLA system is thoroughly examined in this study from a practical perspective while simulation results illustrate the practicality of the proposed developments. The combined attitude and thermal management capability of the PFLA are also examined. This dissertation provides a completed analysis of the PFLA while examining aspects of the actuator that have to date been overlooked in the literature. The operating principals of the PFLA are extrapolated, and a new actuator based on spherical design is proposed that harnesses the capabilities of the PFLA while providing superior performance enhancements.

BIBLIOGRAPHY

[1]Gilbertson, R. G., and Busch, J. D. "A Survey of Micro-Actuator Technologies for Future Spacecraft Missions," *Journal of the British Interplanetary Society* Vol. 49,No. 4, 1996, pp. 129-138.

[2]Khaligh, Y. S., and Namvar, M. "Adaptive Control of Robot Manipulators Including Actuator Dynamics and without Joint Torque Measurement," *IEEE International Conference on Robotics and Automation (ICRA)*,No. 11042, 2010, pp. 4639-4644.

[3]Technologies, B. C. "Rw1," http://bluecanyontech.com/rw1 [March 2017].

[4]Votel, R., and Sinclair, D. "Comparison of Control Moment Gyros and Reaction Wheels for Small Earth-Observing Satellites," *26th Annual AIAA/USU Conference on Small Satellites*,No. 1, 2012, pp. 1-5.

[5]Limited, B. F. "Control Moment Gyroscope Platform," https://www.gyroscope.com/d.asp?product=CMG [April 2017].

[6]Cui, P., He, J., Cui, J., and Li, H. "Improved Path Planning and Attitude Control Method for Agile Maneuver Satellite with Double-Gimbal Control Moment Gyros," *Mathematical Problems in Engineering* Vol. 2015,No. 878724, 2015, pp. 1-11.

[7]Yoon, H., and Tsiotras, P. "Singularity Analysis of Variable Speed Control Moment Gyros," *Journal of Guidance, Control, and Dynamics* Vol. 27,No. 3, 2004, pp. 374-386.

[8]Aerospace, V. "Magentic Torquer Vmt-35," http://www.vectronic-aerospace.com/space-applications/magnetic-torquer-vmt-35 [April 2017].

[9]Yan, L., Chen, I.-M., Lim, C. K., Yang, G., Lin, W., and Lee, K.-M. "Design and Analysis of a Permanent Magnet Spherical Actuator," *IEEE/ASME Transactions on Mechatronics* Vol. 13,No. 2, 2008, pp. 239-248.

[10]Williams, F., Laithwaite, E., and Eastham, J. "Development and Design of Spherical Induction Motors," *Proceedings of the IEE-Part A: Power Engineering* Vol. 106,No. 30, 1959, pp. 471-484.

[11]Lee, K.-M., and Kwan, C.-K. "Design Concept Development of a Spherical Stepper for Robotic Applications," *IEEE Transactions on Robotics and Automation* Vol. 7,No. 1, 1991, pp. 175-181.

[12]Yano, T., and Suzuki, T. "Basic Characteristics of the Small Spherical Stepping Motor," *IEEE/RSJ International Conference on Intelligent Robots and Systems* Vol. 2 2002, pp. 1980-1985.

[13]Kaneko, K., Yamada, I., and Itao, K. "A Spherical Dc Servo Motor with Three Degrees of Freedom," *Journal of Dynamic Systems, Measurement, and Control* Vol. 111,No. 3, 1989, pp. 398-402.

[14]Bederson, B. B., Wallace, R. S., and Schwartz, E. L. "A Miniature Pan-Tilt Actuator: The Spherical Pointing Motor," *IEEE Transactions on Robotics and Automation* Vol. 10,No. 3, 1994, pp. 298-308.

[15]Wang, W., Wang, J., Jewell, G., and Howe, D. "Design and Control of a Novel Spherical Permanent Magnet Actuator with Three Degrees of Freedom," *IEEE/ASME Transactions on Mechatronics* Vol. 8,No. 4, 2003, pp. 457-468.

[16]Chen, W., Zhang, L., Yan, L., and Liu, J. "Design and Control of a Three Degree-of-Freedom Permanent Magnet Spherical Actuator," *Sensors and Actuators A: Physical* Vol. 180 2012, pp. 75-86.

[17]Kim, H., Kim, H., Ahn, D., and Gweon, D. "Design of a New Type of Spherical Voice Coil Actuator," *Sensors and Actuators A: Physical* Vol. 203 2013, pp. 181-188.

[18]Das, C., Wang, G., and Payne, F. "Some Practical Applications of Magnetohydrodynamic Pumping," *Sensors and Actuators A: Physical* Vol. 201 2013, pp. 43-48.

[19]Bushnell, D. M. "Advanced-to-Revolutionary Space Technology Options-the Responsibly Imaginable." NASA Langley Research Center, Hampton, VA, United States, 2013, pp. 3-15.

[20]Laughlin, D., Sebesta, H., and Eckelkamp-Baker, D. "A Dual Function Magnetohydrodynamic (Mhd) Device for Angular Motion Measurement and Control," *American Astronautical Society*,No. 111, 2002, pp. 335-348.

[21]Jang, J., and Lee, S. S. "Theoretical and Experimental Study of Mhd (Magnetohydrodynamic) Micropump," *Sensors and Actuators A: Physical* Vol. 80,No. 1, 2000, pp. 84-89.

[22]Bau, H. H., Zhong, J., and Yi, M. "A Minute Magneto Hydro Dynamic (Mhd) Mixer," *Sensors and Actuators B: Chemical* Vol. 79,No. 2, 2001, pp. 207-215.

[23]Lemoff, A. V., and Lee, A. P. "An Ac Magnetohydrodynamic Micropump," *Sensors and Actuators B: Chemical* Vol. 63,No. 3, 2000, pp. 178-185.

[24]Karmozdi, M., Salari, A., and Shafii, M. B. "Experimental Study of a Novel Magneto Mercury Reciprocating (Mmr) Micropump, Fabrication and Operation," *Sensors and Actuators A: Physical* Vol. 194 2013, pp. 277-284.

[25]Moghadam, M. E., and Shafii, M. B. "Rotary Magnetohydrodynamic Micropump Based on Slug Trapping Valve," *Microelectromechanical Systems, Journal of* Vol. 20,No. 1, 2011, pp. 260-269.

[26]Rabinovich, B., and Grishin, A. "Attitude Stabilization of a Rotating Spacecraft with Flexible Elements and a Magnetohydrodynamic Control System," *Journal of Structural Control* Vol. 10,No. 1, 2003, pp. 25-39.

[27]Patel, S. "Design and Development of Fluid Based Attitude Control System," *Department of Aerospace Engineering*. MASc Thesis, Ryerson University, Toronto, Canada, 2011.

[28]Gasbarri, P., and Teofilatto, P. "Fluid Ring Damper for Artificial Gravity Rotating System Used for Manned Spacecraft," *Acta Astronautica* Vol. 64,No. 11, 2009, pp. 1286-1292.

[29]Kumar, K. "Satellite Attitude Stabilization Using Fluid Rings," *Acta Mechanica* Vol. 208,No. 1-2, 2009, pp. 117-131.

[30]Nobari, N. A., and Misra, A. "Satellite Attitude Stabilization Using Four Fluid Rings in a Pyramidal Configuration," *AIAA/AAS Astrodynamics Conference* 2010, pp. 7652-1.

[31]Nobari, N. A., and Misra, A. K. "Attitude Dynamics and Control of Satellites with Fluid Ring Actuators," *Journal of Guidance, Control, and Dynamics* Vol. 35,No. 6, 2012, pp. 1855-1864.

[32]Nobari, N. A., and Misra, A. K. "A Hybrid Attitude Controller Consisting of Electromagnetic Torque Rods and an Active Fluid Ring," *Acta Astronautica* Vol. 94,No. 1, 2014, pp. 470-479.

[33]Xiao-wei, S., Xue-qin, C., Yun-hai, G., and Shi-jie, Z. "Small Satellite Attitude Control Based on Mechanically-Pumped Fluid Loops," *6th IEEE Conference on Industrial Electronics and Applications (ICIEA)*. IEEE, 2011, pp. 149-153.

[34]Nobari, N. A., and Misra, A. "Satellite Attitude Stabilization Using Four Fluid Rings in a Pyramidal Configuration," *AIAA/AAS Astrodynamics Conference, Canada* 2010, pp. 1-4.

[35]Salvati, A., and Curti, F. "Mhd Reaction Wheel for Spacecraft Attitude Control: Configuration and Lumped Parameter Model," *2nd IAA Conference on Dynamics and Control of Space Systems*. International Academy of Astronautics, Roma, Italy, 2014.

[36]Ludwig, G. "Relative Advantages of Small and Observatory Type Satellites," *Space Program Issues of the 70's Meeting*. NASA, GODDARD SPACE FLIGHT CENTER, Seattle,WA,U.S.A., 1965, p. 634.

[37]Bialke, B. "High Fidelity Mathematical Modeling of Reaction Wheel Performance," *Guidance and Control* 1998, pp. 483-496.

[38]White, M., Frank. *Fluid Mechanics*, Boston, MA: McGraw-Hill Book Company, 2003.

[39]Cengel, Y. A. *Fluid Mechanics*: Tata McGraw-Hill Education, 2010.

[40]Sidi, M. J. *Spacecraft Dynamics and Control: A Practical Engineering Approach*: Cambridge university press, 1997.

[41]Wertz, J. R. *Spacecraft Attitude Determination and Control*, Dordrecht, Holland: D. Redidel Publishing Company, 2012.

[42]Ismail, Z., and Varatharajoo, R. "A Study of Reaction Wheel Configurations for a 3-Axis Satellite Attitude Control," *Advances in Space Research* Vol. 45,No. 6, 2010, pp. 750-759.

[43]Lee, H., Kim, Y., Y.J., C., and Kim, H. S. "Reconfigurable Satellite Attitude Control Scheme Using Two Reaction Wheels for Limited Mission," *60th International Astronautical Congress*. International Astronautical Federation, 2009.

[44]Li, J., and Kumar, K. D. "Fault Tolerant Attitude Synchronization Control During Formation Flying," *Journal of Aerospace Engineering* Vol. 24,No. 3, 2011, pp. 251-263.

[45]Hablani, H. B. "Momentum Accumulation Due to Solar Radiation Torque, and Reaction Wheel Sizing, with Configuration Optimization." Rockwell International Corp., Seal Beach, CA, United States, 1993, pp. 1-4.

[46]Marshall, T., Gunderman, T., and Mobley, F. "Reaction Wheel Control of the Msx Satellite," *Guidance and Control* 1991, pp. 119-138.

[47]Lappas, V. J. "Design and Testing of a Control Moment Gyroscope Cluster for Small Satellites," *Journal of Spacecraft and Rockets* Vol. 42,No. 4, 2005, pp. 729-739.

[48]Wang, D., Jia, Y., Jin, L., and Xu, S. "Control Analysis of an Underactuated Spacecraft under Disturbance," *Acta Astronautica* Vol. 83 2013, pp. 44-53.

[49]Wie, B., and Barba, P. M. "Quaternion Feedback for Spacecraft Large Angle Maneuvers," *Journal of Guidance, Control, and Dynamics* Vol. 8,No. 3, 1985, pp. 360-365.

[50]Lappas, V., Steyn, W., and Underwood, C. "Attitude Control for Small Satellites Using Control Moment Gyros," *Acta Astronautica* Vol. 51,No. 1, 2002, pp. 101-111.
[51]Godard. "Fault Tolerant Control of Spacecraft," *PhD Thesis*. Ryerson University, Toronto, Canada, 2010, pp. 107-157.
[52]Venkataraman, S., and Gulati, S. "Control of Nonlinear Systems Using Terminal Sliding Modes," *Journal of Dynamic Systems, Measurement, and Control* Vol. 115,No. 3, 1993, pp. 554-560.
[53]Cochin, I. *Analysis and Design of Dynamic Systems*: HarperCollins Publishers, 1980.
[54]Wu B., W. D. "Decentralized Robust Adaptive Control for Attitude Synchronization under Directed Communication Topology," *Journal of Guidance, Control, and Dynamics* Vol. 34,No. 4, 2011, pp. 1276–1282.
[55]Levent, A. "Sliding Order and Sliding Accuracy in Sliding Mode Control," *International Journal of Control* Vol. 58,No. 11, 1993, pp. 1247–1263.
[56]Inc., A. D. "Adxrs646-Ep," *High Stability, Low Noise*
Vibration Rejecting Yaw Rate Gyroscope,No. Rev. A, 2015.
[57]Ha, S. K., Kim, J. H., and Han, Y. H. "Design of a Hybrid Composite Flywheel Multi-Rim Rotor System Using Geometric Scaling Factors," *Journal of composite materials* Vol. 42,No. 8, 2008, pp. 771-785.
[58]Kim, B., Lee, H., and Choi, S. "Three-Axis Reaction Wheel Attitude Control System for Kitsat-3 Microsatellite," *Space Technology-Kedlington* Vol. 16,No. 5, 1996, pp. 291-296.
[59]Zhu, Z., Xia, Y., and Fu, M. "Adaptive Sliding Mode Control for Attitude Stabilization with Actuator Saturation," *IEEE Transactions on Industrial Electronics* Vol. 58,No. 10, 2011, pp. 4898-4907.
[60]Lu, K., Xia, Y., Fu, M., and Yu, C. "Adaptive Finite-Time Attitude Stabilization for Rigid Spacecraft with Actuator Faults and Saturation Constraints," *International Journal of Robust and Nonlinear Control* Vol. 26,No. 1, 2016, pp. 28-46.
[61]Hogan, E. A., and Schaub, H. "Three-Axis Attitude Control Using Redundant Reaction Wheels with Continuous Momentum Dumping," *Journal of Guidance, Control, and Dynamics* Vol. 38,No. 10, 2015, pp. 1865-1871.
[62]Bang, H., Tahk, M.-J., and Choi, H.-D. "Large Angle Attitude Control of Spacecraft with Actuator Saturation," *Control engineering practice* Vol. 11,No. 9, 2003, pp. 989-997.
[63]Lu, K., Xia, Y., and Fu, M. "Controller Design for Rigid Spacecraft Attitude Tracking with Actuator Saturation," *Information Sciences* Vol. 220 2013, pp. 343-366.
[64]Helvajian, H., Janson, W., S. . *Small Satellites: Past, Present, and Future*, El Segundo, California: The Aerospace Press, 2008.
[65]SolidWorks. "Solidworks Flow Simulation 2012 Technical Reference." D2S SolidWorks, 2012, pp. 2.7-2.15.
[66]Birur, G. C., Sur, T. W., Paris, A. D., Shakkottai, P., Green, A. A., and Haapanen, S. I. "Micro/Nano Spacecraft Thermal Control Using a Mems-Based Pumped Liquid Cooling System," *SPIE Micromachining and Microfabrication*. Vol. 4560, 2001, pp. 21-24.
[67]Habib, Y. M., John, B. G., Rickard, L. H., and Steinbeck, J. W. "Heat Pipe with Nanostructured Wick," A10200199, United States, 2010.
[68]Cengel, A. Y. *Heat and Mass Transfer: A Practical Approach*, New York, NY: McGraw-Hill, 2007.
[69]Baturkin, V. "Micro-Satellites Thermal Control—Concepts and Components," *Acta Astronautica* Vol. 56,No. 1, 2005, pp. 161-170.
[70]Telerex. "Heat Pipes," https://www.telerex-europe.com/en-gb/heatpipes [April 2017].
[71]Ku, J., Ottenstein, L., Douglas, D., and Hoang, T. "Validation Design for a Multi-Evaporator Miniature Loop Heat Pipe for Spacecraft Applications," *Journal of Spacecraft and Rockets* Vol. 49,No. 6, 2012, pp. 1008-1018.
[72]Wang, G., Mishkinis, D., and Nikanpour, D. "Capillary Heat Loop Technology: Space Applications and Recent Canadian Activities," *Applied Thermal Engineering* Vol. 28,No. 4, 2008, pp. 284-303.
[73]Tang, Y., Xiang, J., Wan, Z., Zhou, W., and Wu, L. "A Novel Miniaturized Loop Heat Pipe," *Applied Thermal Engineering* Vol. 30,No. 10, 2010, pp. 1152-1158.
[74]Leriche, M., Harmand, S., Lippert, M., and Desmet, B. "An Experimental and Analytical Study of a Variable Conductance Heat Pipe: Application to Vehicle Thermal Management," *Applied Thermal Engineering* Vol. 38 2012, pp. 48-57.
[75]Li, Y.-Z., Wang, Y.-Y., and Lee, K.-M. "Dynamic Modeling and Transient Performance Analysis of a Lhp-Mems Thermal Management System for Spacecraft Electronics," *IEEE Transactions on Components and Packaging Technologies* Vol. 33,No. 3, 2010, pp. 597-606.
[76]Maydanik, Y. F. "Loop Heat Pipes," *Applied Thermal Engineering* Vol. 25,No. 5, 2005, pp. 635-657.

[77]Wang, X.-w., Wan, Z.-p., and Tang, Y. "Heat Transfer Mechanism of Miniature Loop Heat Pipe with Water-Copper Nanofluid: Thermodynamics Model and Experimental Study," *Heat and Mass Transfer* Vol. 49,No. 7, 2013, pp. 1001-1007.

[78]Ellis, M., Anderson, W., and Montgomery, J. "Passive Thermal Management for Avionics in High Temperature Environments." SAE Technical Paper, 2014, pp. 1-10.

[79]Dean, R. N., Harris, D. K., Palkar, A. Y., and Wonacott, G. D. "Liquid Metal-Filled Micro Heat Pipes for Thermal Management of Solid-State Devices," *Industrial Electronics, IEEE Transactions on* Vol. 59,No. 12, 2012, pp. 4888-4894.

[80]Jia, L., Yunze, L., and Jun, W. "Modeling and Analysis of Mems-Based Cooling System for Nano-Satellite Active Thermal Control." 2nd International Symposium on Systems and Control in Aerospace and Astronautics (ISSCAA), 2008, pp. 1-6.

[81]Schick, S., Rusch, B., and Batty, J. C. "Isothermal Structural Panels for Spacecraft Thermal Management," *Small Satellite Conference*. 2011.

[82]Kiomarsipour, N., Shoja Razavi, R., and Ghani, K. "Improvement of Spacecraft White Thermal Control Coatings Using the New Synthesized Zn-Mcm-41 Pigment," *Dyes and Pigments* Vol. 96,No. 2, 2013, pp. 403-406.

[83]Stavely, R. L., Lesieutre, G. A., Frecker, M. I., and Adair, J. H. "Variable Thermal Conductivity, Contact-Aided Cellular Structures for Spacecraft Thermal Control," *54th AIAA/ASME/ASCE/AHS/ASC Structures, Structural Dynamics, and Materials Conference*. Boston, Massachusetts, 2013.

[84]Cognata, T. J., Hartl, D. J., Sheth, R., and Dinsmore, C. "A Morphing Radiator for High-Turndown Thermal Control of Crewed Space Exploration Vehicles," *23rd AIAA/AHS Adaptive Structures Conference* 2014, pp. 1-4.

[85]Mohammadi, N., Mohammadi, M., and Shafii, M. B. "A Review of Nanofluidic Pulsating Heat Pipes: Suitable Choices for Thermal Management of Electronics," *Frontiers in Heat Pipes (FHP)* Vol. 3,No. 3, 2013.

[86]Varatharajoo, R., Kahle, R., and Fasoulas, S. "Approach for Combining Spacecraft Attitude and Thermal Control Systems," *Journal of spacecraft and rockets* Vol. 40,No. 5, 2003, pp. 657-664.

[87]Arnold, S. S., Nuzzaci, R., and Gordon-Ross, A. "Energy Budgeting for Cubesats with an Integrated Fpga," *IEEE Aerospace Conference*. IEEE, Big Sky, MT, USA, 2012.

[88]Etemadi, S., and Krishna D., K. "Spherical Fluid-Momentum Actuator for Attitude Maneuvering and Stabilization of Space Vehicles." CA 2958887, Canada, 2017, pp. 1-6.